

2022-05

# ON THE INFLUENCE OF MAJORANA BOUND STATES IN QUANTUM-RINGS.

MEDINA CUY., FABIÁN GONZALO

---

<http://hdl.handle.net/11673/53600>

*Repositorio Digital USM, UNIVERSIDAD TECNICA FEDERICO SANTA MARIA*

# On the Influence of Majorana Bound States in Quantum-Rings.

FABIÁN GONZALO MEDINA CUY.

**Professor:** PEDRO ORELLANA DINAMARCA

**Profesor:** LUIS ROSALES AHUMADA

Universidad Técnica Federico Santa María



This work is dedicated to my colleague and friend Lina Julieth Castiblanco Tolosa, who has supported my studies and work.

# Contents

<b>1</b>	<b>Introduction</b>	<b>3</b>
<b>2</b>	<b>Majorana Bound States Hybridized in a Quantum-Ring.</b>	<b>6</b>
2.1	Aharonov-Bohm Quantum-Ring. . . . .	6
2.1.1	Charge Persistent Current. . . . .	7
2.2	Topological Superconductors in One Dimension. . . . .	7
2.2.1	s-Wave Superconductivity. . . . .	7
2.2.2	p-Wave superconductors. . . . .	9
2.2.3	Kitaev Model for a p-Wave Superconductor. . . . .	10
<b>3</b>	<b>Rashba Spin-Orbit in a Quantum-Ring With Majorana Bound States.</b>	<b>21</b>
3.1	Quantum-ring with Rashba Spin-Orbit. . . . .	21
3.1.1	Topological Superconductor Coupled to a Quantum-Ring. . . . .	23
3.1.2	Charge and Spin Persistent Currents. . . . .	24
<b>4</b>	<b>Two-terminal Josephson Junctions with Topological Superconductors.</b>	<b>36</b>
4.1	Symmetries. . . . .	36
4.1.1	Time-reversal Symmetry. . . . .	36
4.1.2	Particle-Hole Symmetry. . . . .	37
4.1.3	Chiral Symmetry. . . . .	38
4.1.4	Properties of a System with Chiral Symmetry. . . . .	38

# 1

## Introduction

In the thirties, physicists knew that quantum mechanics was telling us that nature works with complex numbers and not only with real or imaginary numbers. Therefore, every time we look into Schrödinger equation for non-relativistic or Dirac equation for relativistic fermions, quantum mechanics remind us this characteristic of nature. Nevertheless, Ettore Majorana at 1937 found real solutions from Dirac equation, providing an essential interpretation in the quantum world which is that exist fermions that are their own antiparticles [20]. Hence, real solutions from a quantum theory of fermions started to receive the name of Majorana fermions. In this work, we are practically focused on Majoranas predicted theoretically in the topological superconductors.

In condensed matter physics, we deal with strongly correlated systems, where emergent phenomena present in systems of many bodies provide a connection with the quantum world [2]. Superconductivity is an excellent example of these emergent phenomena, where the fermionic ground state of a semiconductor turns out to a bosonic ground state [14, 3]. Such a change in the quantum nature of the material is observed in the macroscopic world by introducing a new state of matter, which is known as superconductivity. Hence, the quantum world holds many more fascinating phenomena which are predicted from the theory, and many of them experimentally demonstrated as Bose-Einstein condensates, spontaneous magnetization, even superfluidity, and superconductivity. The common characteristic among them is the breaking of symmetry, being explicit or spontaneous. Landau's theory of phase transitions provides a path to understand the symmetry breaking in a phenomenological way. The main characteristic of the Landau's theory for phase transitions is the expansion of the free energy in the order parameter around criticality [9]. In condensed matter physics in the past decade, it has been clear that together with the traditional phase transitions, there are the so-called topological phase transitions, which does not have local order parameter. Actually, it is possible to define a nonlocal order parameter in most cases. However, the application of Landau's theory is not straightforward for these nonlocal order parameters. An example of a topological phase is the well-known fractional quantum Hall phase. This phase has a nonlocal order parameter, which corresponds to annihilating an electron at a position and, crucially, unwinding a number of fluxes. The flux unwinding is nonlocal. Hence, states with nonlocal order parameters could be called topologically ordered; in general words, the definition of topological phase is such a phase whose low-energy field theory is a topological field theory. The term topological, used in phases or insulators, implies the existence of a bulk invariant that

differentiates the phases of matter with the same symmetry. For topological insulators, gapless edge modes are associated with topological phases. But in general terms, this is not true. Topological insulators can exist without the presence of gapless edge modes [4].

A periodic table classifying topological insulators and superconductors has been established. The table contains the possible topological states based on three discrete symmetries: Time reversal ( $\mathcal{T}$ ), charge-conjugation ( $\mathcal{PH}$ ) and chiral symmetry ( $\mathcal{C}$ ) [1]. In this document, we are not going through the whole classification of topological states of matter. Rather, we focus on the topological superconducting part, more specifically in the class D where  $\mathcal{T}$ ,  $\mathcal{C}$  are broken, and  $\mathcal{PH}$  (charge conjugation or particle-hole) is the symmetry that protects the edge states. The system with these characteristics is the Kitaev chain, which the edge states are known as Majorana zero modes (MZMs) [15]. Currently, there is active research looking for materials that can host Majoranas either in p-wave superconductors or semiconductors in which is induced superconductivity [26, 22, 13, 25, 12]. Because of the quasiparticles in a superconductor are a linear combination of electrons and holes, the superconductor materials are the natural systems to find Majoranas bound states. The equivalent linear combination of those theoretically predicts as Majoranas bound states. The panorama for Majoranas in one-dimensional systems (nanowires) has been quite promising, even though there are evident difficulties in the detection of a truly MZM [10]. One of such difficulties that we must overcome is the difference between Majoranas and Andreev bound states (ABS) [21, 28, 17]. Clearly, some proposals are made in order to detect such differences [18, 31]. One outstanding idea for the detection of Majoranas was to couple a quantum dot at the extreme of the nanowire such that the Majorana at the edge can tunnel the quantum dot, with the goal to measure the quantum conductance. The conductance in the quantum-dot should be measured half-quantize conductance of a zero-bias peak. And this is because Majoranas in condensed matter physics are a delocalized fermionic state; in one extreme of the nanowire, we have the real part of the fermionic state, while in the other extreme, we have the imaginary part [19]. Even though the experimental detection of Majoranas remains elusive, the exciting aspect is that in the field, it is already known the path to follow for the detection of Majoranas in one-dimensional nanowires. This can be summarized in five signatures. Such a path starts by detecting a robust zero-bias peak (the width of the peak should be smaller than the range in an applied magnetic field), the zero modes should be sensitive to spin anisotropy, meaning that when the applied magnetic field becomes parallel to Rashba the zero-bias peak must disappear, the third signature is that the zero-bias peak must be found in a wide range in the phase space (applied magnetic and electric fields), a next signature is known as Majorana oscillations. When two Majoranas interact, they split from zero energy, showing oscillations. Finally, as Majoranas are formed in pairs, there must be a correlation between the two. Therefore, all that is measured at one edge of the nanowire must be measured the same at another edge of the same nanowire. Once those signatures are confirmed in the same sample, we can certainly say that Majorana-bound states have been found experimentally.

Because Majorana can tunnel quantum systems, we chose to study the influence of MZMs hybridized in a quantum ring crossed by a magnetic flux. This work could be divided into three main parts: A single topological nanowire coupled to a discrete quantum-ring formed by a finite number of sites (quantum-dots). We study the effects of delocaliza-

tion of the two hybridized MZMs presented as Majorana oscillations in the quasiparticle spectrum of the quantum ring. Together with the quasiparticle spectrum, we studied the persistent charge currents as a signal for detecting the Majorana oscillations in the quantum ring. The second part of this work consists of an approach more realistic of the system, which is the consideration of the Rashba spin-orbit in the quantum ring. This new ingredient in the Hamiltonian introduces persistent spin currents, which may be used as a signal for detecting spin anisotropy mentioned above. The last part is the consideration of two Topological superconductors connected to the quantum ring. In other words, four Majoranas hybridize the quantum ring. This system is analyzed in the parameter space determined by the magnetic flux and the phase difference between superconductors. The Majoranas in the quasiparticle spectrum show different patterns that distinguish them in the zero-energy crossings that are topologically protected by  $\mathcal{C}$  symmetry (chiral symmetry). Those patterns have been reported for materials like *ZrZiSe*, *ZrZiTe*, *PbTaSe<sub>2</sub>*, *PtSn<sub>4</sub>* and *ZrSiS* for the nodal line [11, 8, 6, 5]. Nodal points or Weyl cones are reported in materials as *TaAs* [27, 7]. But also, Weyl points in the parameter space have been reported theoretically in multi Josephson junctions [29, 23, 30], and in multi-junctions of topological superconductors (TSCs) [24, 16]. We show that these patterns can be found for a two-junction (TSC).

## 2

# Majorana Bound States Hybridized in a Quantum-Ring.

Quantum-dots are easily tunnelable objects, and a finite collection of them is not an exception. We consider an Aharonov-Bohm ring composed by a finite number of quantum dots attached to a topological superconductor. This setup allows investigating the behavior of Majorana bound states that leak in the ring. This chapter paves the way to understand the influence of Majorana bound states in quantum rings, which is a paper that can be found at the end of the chapter.

### 2.1 Aharonov-Bohm Quantum-Ring.

Aharonov-Bohm effect stands that a charged particle can move in regions of the space where electromagnetic fields are excluded, but the vector potential is present. Hence, the dependence of the vector potential in the wave function appears as a close integral around a circular region and is equal to a magnetic flux. As a result, the magnetic flux in the wave function produces motion of the particles around the close path observed through a persistent current.

Here, we work with a discrete ring crossed by a magnetic flux  $\phi$ . The Hamiltonian in second quantization is written as:

$$H_R = \sum_l \left( v \exp \left( i \frac{2\pi}{N} \Phi \right) c_l^\dagger c_{l+1} + h.c. \right), \quad (2.1)$$

where  $c_l^\dagger$  is the creation of an electron in the position  $l$  site of the ring and  $c_{l+1}$  is the annihilation of the electron in the site  $l + 1$ ,  $N$  is the total number of sites in the ring,  $v$  is the hopping between sites in the ring, and  $\Phi = \phi/\phi_0$  is the magnetic flux in units of the flux quantum  $\phi_0 = h/e$ . The system can be diagonalized by taking it to a momentum space expressing the operators in a Fourier series as:

$$c_l^\dagger = \sum_k \exp(ikl) c_k^\dagger. \quad (2.2)$$

The above Hamiltonian writes directly as:

$$H_R = \sum_{k,k'} \left[ v \exp \left( i \frac{2\pi}{N} \Phi + ik \right) \exp(-il(k - k')) c_k^\dagger c_{k'} + h.c. \right], \quad (2.3)$$

finally, in the diagonal basis:

$$H_R = \sum_k 2v \cos\left(\frac{2\pi}{N}\Phi + k\right) c_k^\dagger c_k. \quad (2.4)$$

Due to the periodic boundary conditions, the momentum  $k$  is quantized as  $k = 2\pi n/N$  being  $n$  the states in the quantum ring. Since we are considering a single state per site in the ring,  $n$  coincides with  $l$ .

### 2.1.1 Charge Persistent Current.

For a one-dimensional quantum-ring, the current for each mode can be expressed as:

$$I_n = \frac{ev_n}{L}, \quad v_k = \frac{1}{\hbar} \frac{\partial E_n}{\partial k}. \quad (2.5)$$

If the spectrum of the quantum ring is given by  $E(k, \Phi) = 2v \cos\left(\frac{2\pi}{N}\Phi + k\right)$ . Here, we can change the variable in order to express the derivative with respect to the magnetic flux.

$$I_n = \frac{e}{L\hbar} \frac{\partial \phi}{\partial k} \frac{\partial E_n}{\partial \phi} = -\frac{eN}{L\hbar} \frac{\partial E_n}{\partial \Phi}, \quad (2.6)$$

where  $\Phi = \phi/\phi_0$ . Measuring the spectrum in units of  $2v$ , we can leave the current dimensionless.

$$\frac{I_n}{I_0} = -\frac{\partial E_n}{\partial \Phi}. \quad (2.7)$$

Here, we have  $I_0 = eN2v/L\hbar$  and  $E_n/2v \rightarrow E_n$ . The above expression for the current is valid only for zero temperature. In this case, we consider finite temperatures, and we should weigh each state with the Dirac distribution function.

$$\frac{I_n}{I_0} = -\frac{\partial}{\partial \Phi} [f(E_n) E_n]. \quad (2.8)$$

## 2.2 Topological Superconductors in One Dimension.

### 2.2.1 s-Wave Superconductivity.

In order to introduce topological superconductivity, it is convenient to start with the formulation of a free electron model (a metal) with spin degeneracy and, in the process, introduce superconducting pairing. The Hamiltonian is given by:

$$H = \sum_{p,\sigma} c_{p,\sigma}^\dagger \left( \frac{p^2}{2m} - \mu \right) c_{p,\sigma} \equiv \sum_{p,\sigma} c_{p,\sigma} \epsilon(p) c_{p,\sigma}, \quad (2.9)$$

where  $\mu$  is the chemical potential and  $\sigma$  denotes the spin. By the use of anticommutation relation  $\{c_{p,\sigma}^\dagger, c_{p',\sigma'}\} = \delta_{p,p'}\delta_{\sigma,\sigma'}$ . We can rewrite the Hamiltonian as:

$$\begin{aligned} H &= \frac{1}{2} \sum_{p,\sigma} [c_{p,\sigma}^\dagger \epsilon(p) c_{p,\sigma} - c_{p,\sigma} \epsilon(p) c_{p,\sigma}^\dagger] + \frac{1}{2} \sum_p \epsilon(p) \\ &= \frac{1}{2} \sum_{p,\sigma} [c_{p,\sigma}^\dagger \epsilon(p) c_{p,\sigma} - c_{-p,\sigma} \epsilon(-p) c_{-p,\sigma}^\dagger] + \frac{1}{2} \sum_p \epsilon(p). \end{aligned} \quad (2.10)$$

Note, the sum index  $p$  in the second term is changed to be  $-p$ . We can introduce the spinor  $\Psi_p = (c_{p,\uparrow}, c_{p,\downarrow}, c_{-p,\uparrow}^\dagger, c_{-p,\downarrow}^\dagger)^T$ . Therefore, the Hamiltonian can be written in matrix form:

$$H = \frac{1}{2} \sum_p \Psi_p^\dagger H_{BdG} \Psi_p + constant, \quad (2.11)$$

where

$$H_{BdG} = \begin{pmatrix} \epsilon(p) & 0 & 0 & 0 \\ 0 & \epsilon(p) & 0 & 0 \\ 0 & 0 & -\epsilon(-p) & 0 \\ 0 & 0 & 0 & -\epsilon(-p) \end{pmatrix}. \quad (2.12)$$

Hence, the subscript BdG (Bogoliubov-de Gennes) stands to label the Hamiltonian written redundantly. We can drop the constant. We can note that the Hamiltonian is invariant under  $\mathcal{PH}$ . In other words,  $H_{BdG} = -CH_{BdG}^T(-p)C^{-1}$  with  $C = \tau_x \otimes I_{2 \times 2}$ . Where  $\tau_x$  is the  $x$  component of the Pauli matrices. This invariance becomes more important in the case of superconductivity and is called particle-hole symmetry, but is evident that is not a real symmetry of the system. Since we have doubled the states of the system instead of having two degrees of freedom, the Hamiltonian now has four degrees. What is important about the redundancy is that only two out of four bands give independent quasiparticle states. The hole point of doing this is that for a mean-field superconducting theory, the solution is easier to solve by writing the Hamiltonian in a BdG form. Hence, for a superconducting pairing, the above Hamiltonian is written as:

$$H + H_\Delta = \frac{1}{2} \sum_p \Psi_p^\dagger H_{BdG} \Psi_p, \quad (2.13)$$

$$H_{BdG} = \frac{1}{2} \begin{pmatrix} \epsilon(p) & 0 & 0 & \Delta \\ 0 & \epsilon(p) & -\Delta & 0 \\ 0 & -\Delta^* & -\epsilon(-p) & 0 \\ \Delta^* & 0 & 0 & -\epsilon(-p) \end{pmatrix} \quad (2.14)$$

We can find the energy spectrum because  $H_{BdG}^2(p) = (\epsilon(p)^2 + |\Delta|^2) I_{2 \times 2}$ . Thus, the energy spectrum is made up of two doubly degenerate bands with energies:

$$E_\pm = \pm \sqrt{\epsilon(p)^2 + |\Delta|^2}. \quad (2.15)$$

The spectrum has an energy gap whenever  $|\Delta| \neq 0$ . In fact, the spectrum has similar features to that of a band insulator with a fine-tuned particle-hole symmetry. However, there is an important difference between the fermionic excitations of the gapped insulator state and the gapped superconductor state, namely, the superconductor quasi-particles are combinations of particle and hole states.

## 2.2.2 p-Wave superconductors.

The most accessible models of TSCs are the mean-field BdG Hamiltonians with spinless fermions in one and two dimensions. Hence, spinless fermion sounds like a theoretical approach and is impossible to obtain in real experiments. Fortunately, this condition can be imposed experimentally by fully polarizing the fermions. Here we only focus on one-dimensional TSCs, and the Hamiltonian is written as:

$$H + H_\Delta = \sum_p c_p^\dagger \left( \frac{p^2}{2m} - \mu \right) c_p + \frac{1}{2} \left( \Delta p c_p^\dagger c_{-p}^\dagger + \Delta^* p c_{-p} c_p \right) \quad (2.16)$$

and the BdG Hamiltonian is

$$H_{BdG} = \sum_p \begin{pmatrix} \frac{p^2}{2m} - \mu & \Delta p \\ \Delta^* p & -\frac{p^2}{2m} + \mu \end{pmatrix}, \quad (2.17)$$

where  $\Psi_p = (c_p \ c_{-p}^\dagger)^T$  is a two component spinor. The presence of a linear  $p$  indicates the p-wave pairing. This model has two energy bands  $E_\pm = \pm \sqrt{\epsilon(p)^2 + |\Delta|^2 p^2}$ , with  $\epsilon(p) = \frac{p^2}{2m} - \mu$ . The energy spectrum is gapped as long as  $\mu \neq 0$ . The critical point  $\mu = 0$  separates two physical regimes: weak pairing ( $\mu > 0$ ) and strong pairing ( $\mu < 0$ ). The system is weak pairing with  $\Delta = 0$  is a metallic system, and in its superconducting phase is BCS-like. In strong pairing phase, the system with  $\Delta = 0$  is a gapped insulator and does not fit the usual weak pairing BSC stability picture because there are no low energy fermions.

One of those two phases is a topological one. In order to know which one is the topological phase, we need to take a finite limit mass. But, first let us take the limit  $m \rightarrow \infty$ , the matrix structure becomes a massive one dimensional Dirac Hamiltonian:  $H_{BdG} = \text{Re}\Delta p \sigma_x - \text{Im}\Delta p \sigma_y - \mu \sigma_z$ . Because we are considering only a single superconductor, we can use a global phase rotation to make  $\Delta$  real. Hence, the Hamiltonian becomes  $H_{BdG} = \text{Re}\Delta p \sigma_x - \mu \sigma_z$ .

We can expect to see bound state zero modes. If the chemical potential depends on the coordinates  $\mu \rightarrow \mu(x)$ , and that  $\mu(x)$  has a soliton kink profile with  $\mu(-\infty) < 0$  and  $\mu(+\infty) > 0$ . Hence, we can look for the single-particle, zero-energy solution  $|\psi\rangle$  such that  $H_{BdG} |\psi\rangle = 0 |\psi\rangle$ .

$$|\psi(x)\rangle = \exp\left(-\frac{1}{|\Delta|} \int_0^x \mu(x') dx'\right) |\phi\rangle \quad (2.18)$$

Acting  $H_{BdG}$  on the ansatz, it is easy to obtain:

$$\begin{pmatrix} -\mu(x) & i\mu(x) \\ i\mu(x) & \mu(x) \end{pmatrix} |\phi\rangle = 0 \quad (2.19)$$

The solution of this equation is:

$$|\phi\rangle = \frac{1}{\sqrt{2}} \begin{pmatrix} 1 \\ -i \end{pmatrix} \quad (2.20)$$

Here, the full state reads

$$|\psi\rangle = \frac{1}{\sqrt{2}} \exp\left(-\frac{1}{|\Delta|} \int_0^x \mu(x') dx'\right) \begin{pmatrix} 1 \\ -i \end{pmatrix} \quad (2.21)$$

We can write this state in second quantization as:

$$\gamma = \frac{1}{\mathcal{N}} \int dx \exp\left(-\frac{1}{|\Delta|} \int_0^x \mu(x') dx'\right) \frac{1}{\sqrt{2}} (c(x) - ic^\dagger(x)) \quad (2.22)$$

Multiplying by a phase factor  $e^{i\frac{\pi}{4}}$ . Note that  $\gamma' = e^{i\frac{\pi}{4}}\gamma$  is  $\gamma'^\dagger = \gamma'$ . Thus,  $\gamma'$  is an MZM. Hence, we can not distinguish the phases exactly in the infinite mass limit because they are identical. From here, we need to take the limit of finite mass. Hence, the band disperses upwards or downwards in energy, with clear dependence of the sign of  $m$ . By choosing  $m > 0$  and sticking in that choice, it is clear the difference between  $\mu > 0$  and  $\mu < 0$ . If we turn on a finite  $\Delta$  when  $\mu < 0$ , the system remains gapped; thus, the trivial insulator phase when  $\Delta = 0$  is adiabatically connected with the quasiparticle spectrum of the gapped superconductor phase when  $\mu < 0$ ,  $\Delta \neq 0$ . This does not happen with  $\mu > 0$ . At  $\Delta = 0$  the system is gapless and becomes gapped only when there is a nonzero  $\Delta$ . We cannot adiabatically connect the  $\mu > 0$ ,  $\Delta \neq 0$  phase to the trivial insulating limit  $\mu < 0$ ,  $\Delta = 0$  without passing through a gapless point or region. Therefore,  $\Delta \neq 0$  we find zero-energy modes when  $\mu > 0$  and no zero-energy modes when  $\mu < 0$ .

### 2.2.3 Kitaev Model for a p-Wave Superconductor.

A model was born as a toy model for one-dimensional TSC and became one of the most used models in the field. Here, we explain the model and the considerations for the two phases (the trivial and topological). Let us start with the Hamiltonian of a one-dimensional spinless lattice with superconducting pairing

$$H = \sum_j \left[ -t (c_j^\dagger c_{j+1} + c_{j+1}^\dagger c_j) - \mu c_j^\dagger c_j + |\Delta| (c_{j+1}^\dagger c_j^\dagger + c_j c_{j+1}) \right]. \quad (2.23)$$

From a different perspective, we can replace the fermionic operators with Majorana operators by the following definition:

$$c_j^\dagger = \frac{1}{\sqrt{2}} (\gamma_{2j-1} - i\gamma_{2j}) \quad (2.24)$$

The Hamiltonian in Majorana representation is written as:

$$H = i \sum_j [-\mu \gamma_{2j-1} \gamma_{2j} + (t + |\Delta|) \gamma_{2j} \gamma_{2j+1} + (-t + |\Delta|) \gamma_{2j-1} \gamma_{2j+2}]. \quad (2.25)$$

We can distinguish two phases, from the above Hamiltonian: The trivial phase with  $\mu < 0$  and  $|\Delta| = t = 0$ . In this case, the Hamiltonian reduces to

$$H = -\mu i \sum_j \gamma_{2j-1} \gamma_{2j}. \quad (2.26)$$

The topological phase with  $|\Delta| = t > 0$  and  $\mu = 0$ . For this case, the Hamiltonian reduces to

$$H = 2ti \sum_j \gamma_{2j} \gamma_{2j+1}. \quad (2.27)$$

Hence, we can perform a transformation to Dirac operators such that group the sites  $j$  and  $j+1$  as follows  $\tilde{c}_j = (\gamma_{2j} + i\gamma_{2j+1})/\sqrt{2}$  and the Hamiltonian rewrites  $H = 2t \sum_i (\tilde{c}_i^\dagger \tilde{c}_i - \frac{1}{2})$ . The states satisfy  $\tilde{c}_j |\psi\rangle = 0$  for all values of  $j$ . What we have is that there are two orthogonal states that satisfy the zero energy mode,  $|\psi_0\rangle$  and  $|\psi_1\rangle$ . Here we have the Majorana operators  $\gamma_1$  and  $\gamma_2$  the edge states that unpaired for an infinite chain. Hence, for a finite chain Majorana modes interact, and we can write an effective Hamiltonian as

$$H = i\xi_M \gamma_1 \gamma_2. \quad (2.28)$$

Where  $\xi_M \sim e^{-L/l_0}$  with  $L$  the length of the chain and  $l_0$  the superconducting characteristic length. The above Hamiltonian together with (2.4) are the main theories for our first article.

# Influence of Majorana Bound States in Quantum Rings

Fabián Medina,\* Juan Pablo Ramos-Andrade, Luis Rosales, and Pedro Orellana

**A quantum ring coupled to a 1D topological superconductor hosting Majorana bound states (MBSs) is investigated. The MBSs effects over the spectrum and persistent current along the quantum ring are studied. The spectra of the system are obtained by an exact numerical diagonalization of the Bogoliubov-de Gennes Hamiltonian in the Majorana representation. In addition, Green's function formalism is implemented for analytical calculations and obtained a switching condition in the MBSs fermionic parity. Three different patterns that could be obtained for the spatial separation of the MBSs, named: bowtie, diamond, and asymmetric, are reported here, which are present only in odd parity in the quantum ring, while only a single pattern (bowtie) is obtained for even parity. Those patterns are subject strictly to the switching condition for the MBSs. Besides, quantum ring with the presence of a Majorana zero mode presents gapped/gapless spectra in odd/even parity showing in the even case a subtle signature in the persistent current.**

## 1. Introduction

Majorana fermions are particles whose principal feature is to be their own antiparticles.<sup>[1]</sup> In condensed matter physics, they appear as zero-energy excitations (quasi-particles). Localized Majorana-like excitations, called Majorana bound states (MBS), satisfy non-Abelian statistics, therefore, they are of interest for quantum computation implementations.<sup>[2]</sup> Theoretically, a MBS is predicted to be found in a  $p$ -wave superconductor half-quantum vortex.<sup>[3]</sup> Several proposals have been carried out to detect MBSs, such as resonant Andreev reflection by a scanning tunneling microscope (STM),<sup>[4]</sup> the  $4\pi$  periodic Majorana-Josephson current,<sup>[5]</sup> the implementation of optically trapped one-dimensional (1D) fermionic atoms<sup>[6]</sup> or an effective model in a cold-atom honeycomb lattice with textured pairings,<sup>[7]</sup> among others. On the other hand, Kitaev developed a proposal based on a spinless chain proximitized by a superconductor. This model represents a topological superconductor (TSCs) at which MBSs appears localized at its ends.<sup>[8]</sup>

Recent experimental advances suggest that the physical realization of Kitaev proposal has been carried out<sup>[9]</sup>. In this scenario, zero-bias anomalies in transport quantities measured through TSCs have been proposed to detect the presence of MBSs.<sup>[10–15]</sup> Since MBSs are exotic states, it is also interesting to explore its

interplay with regular fermionic states, such as quantum dots (QDs). For instance, the linear conductance through a QD with a side-coupled TSC exhibit a zero-bias distinctive characteristic; a half-integer conductance.<sup>[16–18]</sup> Interference phenomena in multiple QD-chains connected with MBSs have also been considered, proposing additional features for detection.<sup>[19,20]</sup> A recent experimental study of the non-locality of emergent zero modes in superconductor-semiconductor hybrid nanowire devices has been accomplished, where more than to observe the zero mode, the authors have focused on measure the patterns formed due to the overlapping of MBSs.<sup>[21]</sup> Another experimental measurement was carried out in a gold surface with Europium islands, where the

Majorana modes were observed as zero bias peak. This platform promises to have advantages in the robustness in energy scales and the possibility of realizing complex designs using lithographic methods.<sup>[22]</sup> At this point, it is relevant to mention that the presence of TSCs hosting MBSs affects the transport phenomena, being a useful way for detection implementations.

Although theoretical results obtained in QD-MBS coupled systems cannot be refused, in physical realizations, resonant tunneling not always ensures the detection of MBSs mostly due to decoherence effects, which may suppress the signature of the MBSs. Therefore, it is attractive to study isolated systems and characterize any possible variations in their physical properties due to the presence of the MBSs and going into a bit further studying the possibility to control MBSs. An fascinating system is an isolate quantum ring crossed by a magnetic flux, also called  $U(1)$  gauge field. Due to the presence of this gauge field the system shows persistent currents, which corresponds to the generation of a spontaneous current as a response to changes in magnetic flux. Persistent currents have been well studied both experimentally and theoretically,<sup>[23–26]</sup> focusing on magnification,<sup>[27]</sup> controlling local currents,<sup>[28]</sup> currents in 1D disordered rings,<sup>[29]</sup> electron correlations,<sup>[30]</sup> and even in alternative ways to generate persistent currents without a magnetic flux.<sup>[31]</sup> Furthermore, persistent currents are sensitive to external perturbations, any change that makes variations in the spectra of a determined system will be observed in the persistent current. In this sense, the use of persistent currents with the purpose of detecting MBSs has been studied theoretically by Gong et al.,<sup>[32]</sup> where a TSC is embedded in the QD-ring. As a result, the relevant signature of the MBSs is the cancellation of persistent current signal when the ring parity is even. Ghazaryan et al.<sup>[33]</sup> show that

Dr. F. Medina, Dr. J. P. Ramos-Andrade, Dr. L. Rosales, Prof. P. Orellana  
Departamento de Física  
Universidad Técnica Federico Santa María  
Casilla 110-V, Valparaíso, Chile  
E-mail: fabian.medinac@sansano.usm.cl

DOI: 10.1002/andp.202000199

for a ring with a few hundred angstroms and a particular range of chemical potential, the system is in a topological phase with the possibility to find MBS. Some different geometries have been considered, such as 1D topological superconductor weakly coupled to a normal metal as a ring-shaped junction and the proposal is to observe the interference patterns in the conductance<sup>[34]</sup> or the behavior in the maximal interference contrast.<sup>[35]</sup>

In this work, we study the spectra and the persistent current signals of a quantum ring side-coupled with a TSC hosting MBSs. By direct diagonalization of the BdG Hamiltonian and an analytical analysis by using a Green's function techniques, we found the changes in the quantum ring spectra due to the connection with MBSs, which leads to establish a persistent current behavior depending on ring-TSC and/or MBSs coupling parameters. We believe our findings could be useful to provide further characterization of persistent currents in the presence of MBSs. The manuscript is organized as follows: In Section 2 we present the model and theoretical background implemented along this work. In Section 3, we present the corresponding analytic results and their related discussions, and finally, we conclude by giving the final remarks in Section 4.

## 2. Model

We follow the experimental setups of nanowires attached to a single QD,<sup>[21,36,37]</sup> where the QD is part of the same nanowire made of InAs. In these setups, a segment of the nanowire is covered with Al to build a TSC, leaving bare a shorter section of a few nm at the edge, which plays the role of QD. Gate voltages control the charge in the QDs. Based on the previous description, we can ruffly imagine a system in which a ring form as an extension of the same nanowire is made. Gate voltages can also control QDs along the ring. For our purpose, this ring-like arrangement of QDs is crossed by a magnetic flux  $\phi$ , being the control parameter in the system.

The system under study consists of a discrete number of QDs arranged to form a quantum ring coupled to a TSC, which is hosting MBSs at its ends, as is illustrated in **Figure 1**. We model the system utilizing an effective low-energy Hamiltonian, which describes the electronic motion through the ring, in the presence of MBSs. The Hamiltonian is written as

$$H = H_R + H_M + H_C \quad (1)$$

where the term  $\hat{H}_R = \sum_l v(\exp[i(2\pi/N)\Phi]c_l^\dagger c_{l+1} + \text{h.c.})$  corresponds to the quantum ring Hamiltonian in the position space, where  $v = v^*$  is the nearest-neighbor coupling parameter in the quantum ring. Since the ring is crossed by a magnetic flux, a phase factor  $\Phi = \phi/\phi_0$  is included, expressed in units of the quantum flux  $\phi_0 = h/e$ . We set the on-site energy at zero, and in order to perform the calculations, we express  $\hat{H}_R$  in the momentum space. Thus, we write

$$H_R = \sum_k \varepsilon_k(\Phi) c_k^\dagger c_k \quad (2)$$

where  $\varepsilon_k(\Phi) = 2v \cos[(2\pi/N)\Phi + ka]$  and  $k = 2\pi n/N$ .

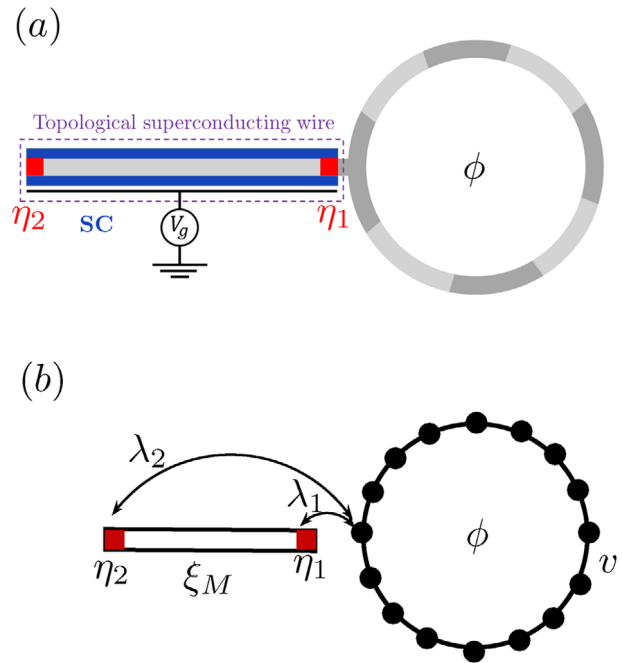


**Figure 1.** a) Schematic view of a possible experimental realization: The quantum-ring is an extension of the InAs hosting MBSs at the edges, where the dark gray zones in the ring are the bare InAs (QDs). The blue bar represents the Al covering the InAs wire, forming the TSC hosting MBSs (red squares) at the edges. b) Schematic view of the tight-binding model: TSC hosting MBSs at its ends (red) side attached to a QD-ring (connected black dots). The ring arrangement of QDs is crossed by a magnetic flux  $\phi$ .

The second term on the right-hand side of Equation (1),  $H_M$ , corresponds to the MBSs, which is described within the effective form described by Kitaev<sup>[8]</sup> as

$$H_M = i\xi_M \eta_1 \eta_2 \quad (3)$$

where  $\eta_\alpha$  is the Majorana operator in the  $\alpha$ -edge ( $\alpha = 1, 2$ ) of the TSC. Majorana operators satisfy both  $\{\eta_\alpha, \eta_\beta^\dagger\} = \delta_{\alpha,\beta}$  and  $\eta_\alpha = \eta_\alpha^\dagger$ , that is, MBSs are characterized by being their own anti-particles. A useful way to treat them analytically is by means of regular fermionic operators superposition, as  $\eta_1 = (f + f^\dagger)/\sqrt{2}$  and  $e^{-\ell/\ell_0} \eta_2 = -i(f - f^\dagger)/\sqrt{2}$ . The inter MBSs coupling  $\xi_M$  describes the connection between both MBSs and it is proportional to  $\xi_M \sim e^{-\ell/\ell_0}$ , being  $\ell$  the nanonowire length and  $\ell_0$  the superconducting coherence length. Note that in the case of  $\xi_M = 0$ , both MBSs are strictly equivalent. The last term in the right hand side of Equation (1) describes the coupling between MBSs and quantum ring. Which is expressed as

$$H_C = \lambda \sum_k (c_k f^\dagger + f c_k^\dagger) \quad (4)$$

In Majorana representation, the same Hamiltonian is written as

$$H_C = i\lambda_1 \sum_k \alpha_k^{(2)} \eta_1 + i\lambda_2 \sum_k \eta_2 \alpha_k^{(1)} \quad (5)$$

where  $\lambda \sim \lambda_1$  and  $\lambda_2 \sim \lambda_1 e^{-l/l_0}$  are the couplings given by the projection of the fermionic states of the Kitaev nanowire on the fermionic states of the ring, as is done for a Kitaev nanowire and a QD in [38]. Note that the operators  $\alpha_k^{(1)} = (c_k + c_k^\dagger)/\sqrt{2}$  and  $\alpha_k^{(2)} = -i(c_k - c_k^\dagger)/\sqrt{2}$ . Without loss of generality, we have chosen the coupling parameter between the ring and the MBS to be real, that is,  $\lambda_{1(2)} = \lambda_{1(2)}^*$ .

We will focus on the spectra and persistent current in the quantum ring. The spectra is fully obtained by direct diagonalization of the Hamiltonian and the implementation of the Green's function method is used for an analytical analysis. Hence, we choose an spinor representation

$$\Psi_{N-1} = \left( \alpha_0^{(1)} \alpha_0^{(2)} \alpha_1^{(1)} \alpha_1^{(2)} \dots \alpha_{N-1}^{(1)} \alpha_{N-1}^{(2)} \eta_1 \eta_2 \right)^T \quad (6)$$

as the basis dimension of size  $D = 2N + 2$ , where the  $2N$  is due to the ring states mapping into the Majorana basis as consequence of the Bogoliubov-de Gennes (BdG) formalism. Therefore, Equation (1) in matrix representation is written as

$$H = \frac{1}{2} \Psi_{N-1}^\dagger H_{\text{BdG}} \Psi_{N-1} \quad (7)$$

The factor  $1/2$  comes from the redundancy of the BdG formalism and for our results, we let it be absorbed into the amplitudes. Finally, the expression for the persistent currents present in the quantum ring is obtained by

$$I_n = -\frac{\partial}{\partial \phi} [f(E_n) E_n] \quad (8)$$

where  $\phi$  is the magnetic flux,  $E_n$  is the quantum ring spectrum and  $f(E_n)$  is the Fermi distribution function. Then, the spectrum slope will determine if the persistent current is diamagnetic or paramagnetic. In the specific case in which we are considering spinless electrons, the persistent current is diamagnetic when the electron number is odd, and it is paramagnetic otherwise. This phenomenon is known as Leggett's conjecture.[39] We obtain the total persistent current in the quantum ring by summing over all  $n$  states:[40]

$$I = -\sum_n I_n \quad (9)$$

For analytical calculations we compute the retarded Green's function for the system in a Majorana representation, the first term of the full Green's function writes

$$A_{(11)}(t) = -i\theta(t) \left\langle \left\{ \alpha_k^{(1)}(t), \alpha_k^{(1)}(0) \right\} \right\rangle \quad (10)$$

where  $\langle \dots \rangle$  is the thermal average and  $\theta(t)$  is the Heaviside function, the anticommutator stands because we are dealing with electrons moving along the ring.

### 3. Results and Discussions

In what follows, the Green's function is expressed in energy domain, and the results are presented in units of  $2\nu$  and for zero

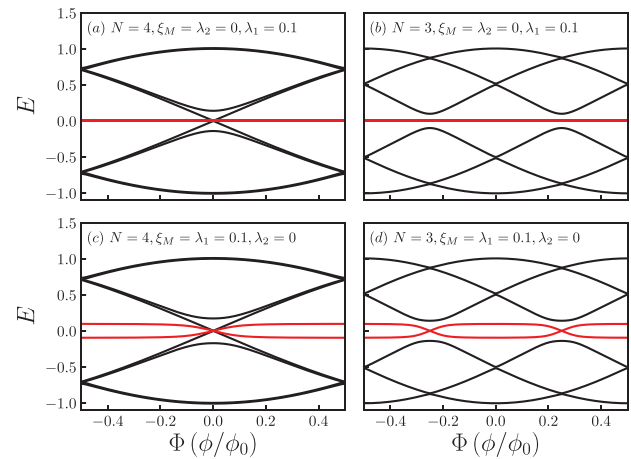


**Figure 2.** Energy spectra  $E$  as function of magnetic flux  $\Phi$ , for fixed  $\xi_M = \lambda_2 = 0$  and  $\lambda_1 = 0.1$  [(a) and (b)], and for  $\xi_M = \lambda_1 = 0.1$  and  $\lambda_2 = 0$  [(c) and (d)].  $N = 4$  and  $N = 3$  are for left and right panels, respectively. Solid red lines represent MBSs in all panels.

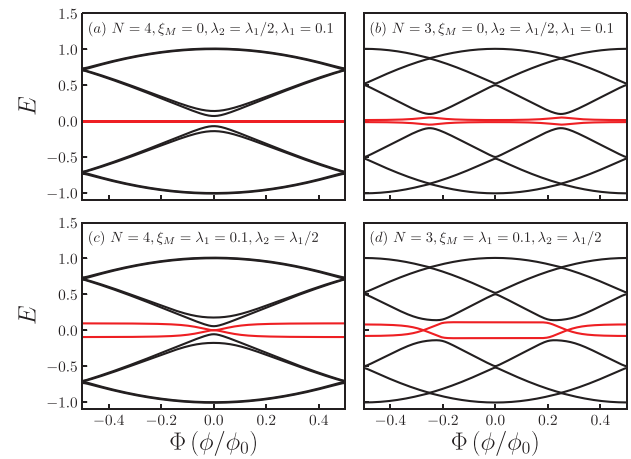


**Figure 3.** Energy spectra  $E$  as function of magnetic flux  $\Phi$ , for fixed  $\xi_M = 0$ ,  $\lambda_2 = \lambda_1/2$  and  $\lambda_1 = 0.1$  [(a) and (b)], and for  $\xi_M = \lambda_1 = 0.1$  and  $\lambda_2 = \lambda_1/2$  [(c) and (d)].  $N = 4$  and  $N = 3$  are for left and right panels, respectively. Solid red lines represent MBSs in all panels.

temperature ( $T = 0$ ). Nevertheless, the MBSs contribution to the persistent current it is also discussed for finite low temperatures.

#### 3.1. Energy Spectra

By using the BdG formalism described in Section 2, we have obtained the energy spectra for the quantum ring connected to the TSC. Depending on the interactions that take place in the system, we observe different electronic behaviors in the spectrum, as it is shown in **Figures 2** and **3**.

Figure 2 displays the spectra for system configuration in the case of  $\lambda_2 = 0$ , that is, with the farther MBS disconnected. Panels (a) and (b) corresponds to even and odd parity, respectively, showing both cases in the long nanowire limit, that is,  $\xi_M = 0$ . For even parity, we obtain a gapless spectrum, while for the odd parity the spectrum is gapped. These two cases represent the

Majorana zero mode (MZM) present in the quantum ring spectrum, regardless  $\Phi$ . The cases with finite distance between MBSs is addressed in panels (c) and (d) using  $\xi_M = 0.1$ . In Figure 2c again it is observed a gapless spectrum for even parity, and in Figure 2d the spectrum is gapped for odd parity. In both, it is presented a bowtie pattern of the MBSs (solid red lines) depending on the magnetic flux.

Figure 3 presents the spectra for system configuration considering interaction with the quantum ring and the farther MBS using  $\lambda_2 \neq 0$ . In this case, the two MBSs hybridize in the quantum ring, and we set  $\lambda_2 = \lambda_1/2$  with  $\lambda_1 = 0.1$ . The upper panels (a) and (b) show the spectra for fixed  $\xi_M = 0$ . We obtain gapped spectra again for both, even and odd parity, with the difference that in panel (b) the two MBSs exhibit a diamond pattern where they do not have any crossing points. It is because the switching in the parity of the MBSs is not allowed in the long-nanowire limit  $\xi_M = 0$ . In the lower panels (c) and (d) it is fixed  $\xi_M = \lambda_1 = 0.1$ , like the previous two panels it is observed a gapped spectra showing a *bowtie* pattern of the MBSs in panel (c), and an *asymmetric* pattern of the MBSs in panel (d). In contrast with Figure 2, we can say that exist two subspaces at which the even parity states of the quantum ring are mapped. One of them interacts with  $\eta_1$ , and the other interacts with  $\eta_2$ ; those subtle details are more evident if we compare them with spectra shown in the Appendix A.1 for a discrete superconducting ring.

The three patterns, *bowtie*, *asymmetric*, and *diamond* have been already reported for the case of a 1D topological superconducting nanowire connected to a single QD.<sup>[37,41]</sup> As we will see in Subsection 3.3, these patterns will have consequences in the persistent currents.

To understand the above results, we found the condition for switching point at zero energy of the MBSs which is determined by

$$\det(H_{\text{BdG}}) = 0 \quad (11)$$

For  $N = 4$ , the condition is

$$\prod_{n=0}^3 \cos\left[\frac{\pi}{2}(n + \Phi)\right] = 0 \quad (12)$$

and for  $N = 3$ , the condition reads as

$$\prod_{n=0}^2 \cos\left[\frac{2\pi}{3}(n + \Phi)\right] = -\frac{3}{4} \frac{\lambda_1 \lambda_2}{\xi_M} \quad (13)$$

From conditions presented in Equations (12) and (13), it is clear that even parity will present always a bowtie pattern, while odd parity displays the three patterns described before. In the bowtie pattern obtained when  $\lambda_2 = 0$  no matter  $\xi_M$  and  $\lambda_1$ , diamond pattern for the limit when  $\xi_M \leq \lambda_1 \lambda_2$ , and asymmetric pattern for  $\xi_M > \lambda_1 \lambda_2$ . These expressions are generalized for any quantum ring parity in the next subsection.

### 3.2. Switching Condition for Majorana Fermion Parity

We have computed the Green's function for the Majorana state  $\alpha_k^{(1)}$ . Hence, for the system shown in Figure 1 the Green's function is obtained from Equation (10) in the energy domain (see Appendix B)

$$A_{(11)}(\epsilon) = \frac{1}{G_0(\epsilon)^{-1} - \Sigma_M} \quad (14)$$

where  $G_0(\epsilon) = [g^{(-)}(\epsilon, n) + g^{(+)}(\epsilon, n)]/2$  is the isolated Green's function for the Majorana operator  $\alpha_k^{(1)}$  and  $g^{(\pm)}(\epsilon, n) = 1/(\epsilon \pm \epsilon_n)$  are the particle and hole Green's functions of the ring, with  $\epsilon_n = \cos[(2\pi/N)\Phi + 2\pi n/N]$ . Additionally, the self-energy  $\Sigma_M(\epsilon, n)$ , which carries the information of the coupling between quantum ring and TSC is written as

$$\Sigma_M = G_0(\epsilon)^{-1} - G_0(\epsilon)^{-1} \Gamma^{-1} \quad (15)$$

where the term  $\Gamma$  is given by

$$\Gamma = \frac{\Gamma_1 + \Gamma_2 + \Gamma_3}{\Gamma_4 - \Gamma_5} \quad (16)$$

and the terms  $\Gamma_i$  are given by:

$$\Gamma_1 = \epsilon^2 - \frac{\epsilon \lambda_1^2}{2} \sum_{n'} [g^{(-)}(\epsilon, n') + g^{(+)}(\epsilon, n')]$$

$$\Gamma_2 = \frac{\xi_M \lambda_1 \lambda_2 \epsilon_n}{2\epsilon} \sum_{n'} [g^{(-)}(\epsilon, n') + g^{(+)}(\epsilon, n')] - \xi_M^2$$

$$\Gamma_3 = \frac{1}{2} (\lambda_1^2 \epsilon_n - \lambda_1 \lambda_2 \xi_M) \sum_{n'} [g^{(-)}(\epsilon, n') - g^{(+)}(\epsilon, n')]$$

$$\Gamma_4 = \Gamma_1 \left\{ 1 - \frac{\lambda_2^2}{2\epsilon} \sum_{n'} [g^{(-)}(\epsilon, n') + g^{(+)}(\epsilon, n')] \right\}$$

$$\Gamma_5 = \left( \frac{\lambda_1 \lambda_2}{2} \sum_{n'} [g^{(-)}(\epsilon, n') - g^{(+)}(\epsilon, n')] + \xi_M \right)^2$$

It is clear how the MBSs are interacting effectively with the quantum ring. The poles of the Green's function provides analytical information which is observed graphically in Figures 2 and 3. Hence, the splitting due to the interaction of the MBSs with the ring states can be found by recognizing the poles of the Green's function. Those are given by

$$G_0(\epsilon)(\Gamma_4 - \Gamma_5) = 0 \quad (17)$$

The above expression represents the poles we can find in the system. The information of the splitting is extracted from the term  $\Gamma_4 - \Gamma_5$  where in the case of  $\lambda_2 = \xi_M = 0$  for  $N = 4$  [Figure 2a] the terms are reduced to  $\Gamma_4 = \Gamma_1$  and  $\Gamma_5 = 0$ . It is observed immediately two zeros, those are:  $\epsilon^2 = 0$  that correspond to the two MZMs solutions. Solving the remaining expression for  $\epsilon$ , evaluating  $\Phi = 0$  and taking the first leading term for  $\lambda_1 \ll 1$  we obtain  $\epsilon_{\pm} \sim \pm \sqrt{2} \lambda_1$  and for odd parity with the same fixed values we get  $\epsilon_{\pm} \sim \pm \lambda_1$ .

The different patterns observed are fully described by the poles  $\Gamma_4 - \Gamma_5 = 0$ , where the condition in Equation (13) can be generalized for any number of states and comes precisely from Equation (17) by looking for the zero eigenvalue  $\varepsilon = 0$ . This expression writes

$$\frac{1}{2} \sum_{n'=0}^{N-1} (g^{(-)}(0, n') - g^{(+)}(0, n')) = -\frac{\xi_M}{\lambda_1 \lambda_2} \quad (18)$$

$$\left[ \sum_{n'=0}^{N-1} \frac{1}{\cos \left[ \frac{2\pi}{N} (n' + \Phi) \right]} \right]^{-1} = \frac{\lambda_1 \lambda_2}{\xi_M} \quad (19)$$

We can see that for  $N = 3$  Equation (13) is recovered. There are some aspects easy to observe from the switching condition by plotting the right and left hand sides of the expression with respect to  $\Phi$ , the values of magnetic flux in which the two curves cross each other are the points where the MBSs parity changes. When the total number of states  $N$  increases, the amplitude in the left hand side of the expression decreases, and for a given value of  $\lambda_1 \lambda_2 / \xi_M$ , there will be an  $N$  where the equality is no longer satisfied regardless  $\Phi$ . This means the asymmetric pattern passes to diamond pattern, for example, for  $\lambda_1 \lambda_2 / \xi_M = 0.05$  the ingap will change from asymmetric to diamond at  $N = 21$ . Additionally, the left hand side has a phase shift of  $\pi$  for each odd number  $N$  meaning positive amplitude for states  $N = 4j + 1$  and negative amplitude for  $N = 4j - 1$ , with  $j = 1, 2, \dots$ . These effects will be shown in the persistent currents in the next subsection.

### 3.3. Persistent Currents

Persistent currents corresponding to the energy spectra showed in Figure 2 are presented in Figure 4 panels (a) and (b) for different values of  $\xi_M$  and additional curves are shown in panels (c) and (d), with  $N = 5$  and  $N = 6$ , respectively. We can observe that the discontinuity in the persistent currents is present in the case of even parity for all values of  $\xi_M$  and  $\lambda_2 = 0$ . Although, an interesting behavior is that the discontinuity remains for  $\xi_M = 0$  (red dotted line) while for odd parity shows a smooth signal similar to the case of the quantum ring with superconductivity [see Figure A1d]. It occurs due to the additional states that appears in even parity. Those remain gapless in the case of  $\lambda_2 = 0$  and are an indirect consequence of the presence of the MZM.

Persistent currents related to the spectra of Figure 3 panels (a) and (b) are shown in the panels (a) and (b) of Figure 5 with an additional two panels (c) and (d) for  $N = 5$  and  $N = 6$ , respectively. We observe discontinuities in all curves except for those that were obtained for  $\xi_M = 0$  (red dotted lines). The difference of these curves and the ones obtained in Figure 4 is the interaction of the two Majoranas with the quantum ring, that is  $\lambda_2 \neq 0$ . This interaction opens a gap in the even parity states, the persistent current becomes smooth and there is not any more distinguishable form with the persistent current of the superconducting quantum ring.

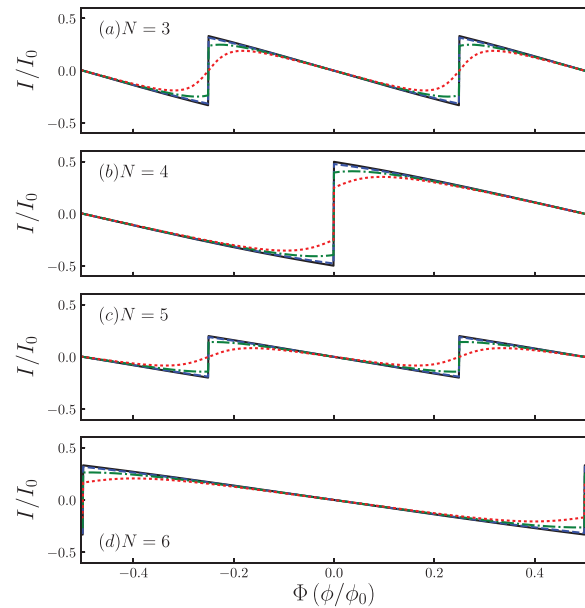


**Figure 4.** Dimensionless persistent current  $I/I_0$ , where  $I_0 = 2ve/\hbar$ , as a function of the dimensionless magnetic flux  $\Phi$ , for fixed  $\lambda_1 = 0.1$  and  $\lambda_2 = 0$ . a)  $N = 3$ , b)  $N = 4$ , c)  $N = 5$ , and d)  $N = 6$ . In all panels,  $\xi_M$  takes values  $\xi_M = 1$  (black solid line),  $\xi_M = 0.3$  (blue dashed line),  $\xi_M = 0.1$  (green dashed-dotted line), and  $\xi_M = 0$  (red dotted line).

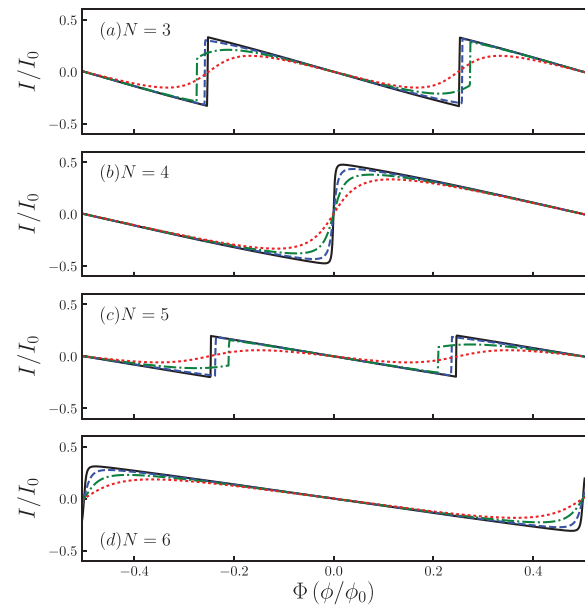


**Figure 5.** Dimensionless persistent current  $I/I_0$  as a function of the dimensionless magnetic flux  $\Phi$  for fixed  $\lambda_1 = 0.1$  and  $\lambda_2 = \lambda_1/2$ . a)  $N = 3$ , b)  $N = 4$ , c)  $N = 5$ , and d)  $N = 6$ . In all panels,  $\xi_M$  takes values  $\xi_M = 1$  (black solid line),  $\xi_M = 0.3$  (blue dashed line),  $\xi_M = 0.1$  (green dashed-dotted line), and  $\xi_M = 0$  (red dotted line).

The asymmetric pattern shows a clear signature in the persistent current with a shift tendency of the discontinuity of the signal when  $\xi_M \rightarrow 0$  as it shows in panels (a) and (c) with blue dashed and green dashed-dotted lines. The sign in Equation (19) determines this shift in the persistent current as was expressed

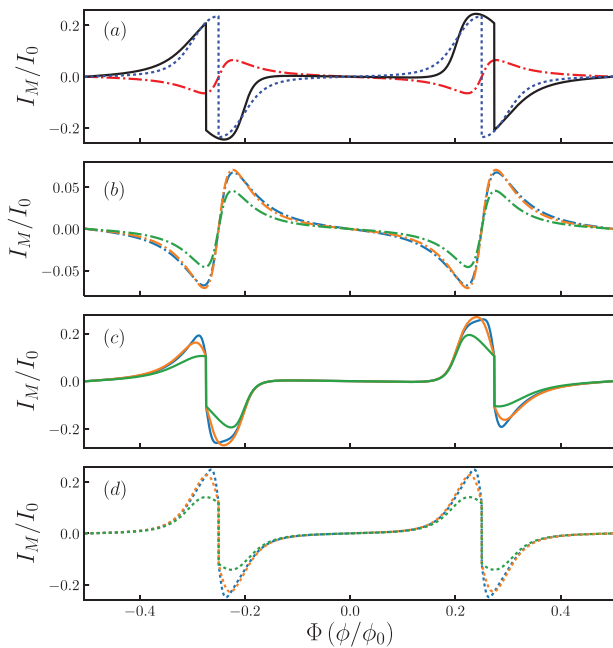


**Figure 6.** *a)* Dimensionless persistent current due to the MBSs  $I_M/I_0$  as a function of the dimensionless magnetic flux  $\Phi$  for  $N = 3$ , for fixed  $\lambda_1 = 0.1$  at temperature  $T = 0$ . Dotted blue, dashed-dotted red and solid black lines represent the signals for the three patterns bowtie, diamond, and asymmetric respectively. Persistent current at finite temperatures for  $\beta = 100$  blue,  $\beta = 50$  orange, and  $\beta = 10$  green lines [(b), (c), and (d)].

before in the text, where if it is negative (case of  $N = 4j - 1$ ) the shift in the persistent current goes outward and if it is positive (case of  $N = 4j + 1$ ) the shift goes inward. Note that the points where there is a change in the parity are reflected as a discontinuity in the persistent current.

**Figure 6** panel (a) displays the contribution of both MBSs ( $I_M$ ) to the persistent current related to *bowtie* ( $\lambda_1 = \xi_M = 0.1$ ,  $\lambda_2 = 0$ ), *diamond* ( $\lambda_1 = 0.1$ ,  $\lambda_2 = 0.05$ ,  $\xi_M = 0$ ) and *asymmetric* ( $\lambda_1 = \xi_M = 0.1$ ,  $\lambda_2 = 0.05$ ) patterns fixing  $N = 3$ . The states are presented in Figures 2 and 3 as solid red lines. In these curves, the persistent currents present a discontinuity only in those cases when the MBSs have a switch in the parity. For the case of the diamond pattern the switching is not allowed, therefore, the corresponding signal in the persistent current is smooth. Panels (b), (c), and (d) show the persistent current signals for finite temperature  $T$  by means of the dimensionless quantity  $\beta = 2\nu/k_B T$ , where  $k_B$  is the Boltzmann constant. We compute  $I_M$  following ref. [40], considering the energy states around the Fermi energy of the system in Equation (8). The values for  $\beta$  considered are  $\beta = 100$ ,  $\beta = 50$ , and  $\beta = 10$  for blue, orange, and green lines, respectively. These values for  $\beta$  are chosen based on the temperature at which has been measured the zero bias peak in InAs wires, being  $T < 1$  K,<sup>[14]</sup> and the coupling between quantum dots is in the order of  $\sim$ meV.<sup>[42]</sup> From these panels, we can observe that persistent currents reduce in amplitude at finite temperatures, but it is important to highlight the discontinuities are preserved.

**Figures 7** and **8** show contour plots of the persistent current, using  $\lambda_2 = 0$  and  $\lambda_2 = 0.05$ , respectively, as function of  $\lambda_1$  and the dimensionless magnetic flux  $\Phi$ . In Figure 7,  $N = 3$  cases are

presented in upper panels (a), (b), and (c) for  $\xi_M = 0, 0.3$ , and 1, respectively. The same configuration is taken for lower panels (d), (e), and (f) with  $N = 4$ . A similar panels distribution is considered in Figure 8, including the case of  $N = 5$  in central panels. These figures are a more general landscape of Figures 4 and 5. It is important to notice the discontinuity of the persistent currents. In the contour plots, it is represented by the sudden change of the color, from red-grey for odd parity to orange-purple for even parity of the ring. The notorious current discontinuity showed in panels (d)–(f) of Figure 7, it is due to the contribution of the already mentioned states which do not respond to the interaction with the state  $\eta_1$  and are present for all even parity cases. On the other hand, the panels (g)–(i) of Figure 8, do not show the sudden change in the persistent current, precisely because the interaction with  $\eta_2$  is turned on, and the spectrum becomes gapped.

In panels (b), (c), (e), and (f) of Figure 8 it is observed the effect of the asymmetric patterns, where the position of the zero energy crossing shifts when  $\lambda_1$  increases. Besides, it is also notorious the inward/outward behavior due to the  $\pi$  phase shift in Equation (19).

A relevant aspect that can modify our results is the presence disorder along the quantum ring. It is expected for a 1D system a localization of the wave function with the increasing of the disorder. In a quantum ring, for weak and moderate disorder strength, the wave function still has to satisfy periodic boundary conditions. Therefore a signal in persistent current is expected (localization length is shorter than the circumference of the ring). However, in the case of the large disorder, strong localization takes place, meaning that the eigenstates of the electrons become standing waves and boundary conditions in the ring are no longer fulfilled. As a consequence, persistent currents vanish as it is shown in ref. [43]. Even though persistent currents vanish with a strong disorder, the patterns we report can survive against a moderate disorder since the crossing points at zero energy are topologically protected. Those crossing points can be detected by a discontinuity in the persistent current, as it is pointed out in the manuscript. A proposal that supports this claim is, ref. [44], where a disorder  $p$ -wave Aharonov–Bohm ring is studied.

## 4. Summary

We have studied the electronic properties of a quantum ring crossed by a magnetic flux, side attached to a 1D TSC, which hosts MBSs at its ends. We focused on the effects and modifications that these MBSs produce on the energy spectra and the persistent currents along the quantum ring. We have obtained the energy spectra by a direct diagonalization of the BdG Hamiltonian, and the analytical details were studied by the implementation of the Green's function techniques. The energy spectra, in the superconductor in-gap region, show characteristic patterns as a function of the quantum flux depending on quantum ring parity and the distance between MBSs, which have influences on the persistent currents of the ring. By taking into account the spatial separation between MBSs, we have obtained three different patterns, depending on the ring parity. Thus, for a quantum ring with odd parity, we can show: i) bowtie pattern obtained when  $\lambda_2 = 0$ ; ii) diamond pattern when  $\xi_M \leq \lambda_1 \lambda_2$  and iii) asymmetric pattern when  $\xi_M > \lambda_1 \lambda_2$ . For the case of a quantum ring with

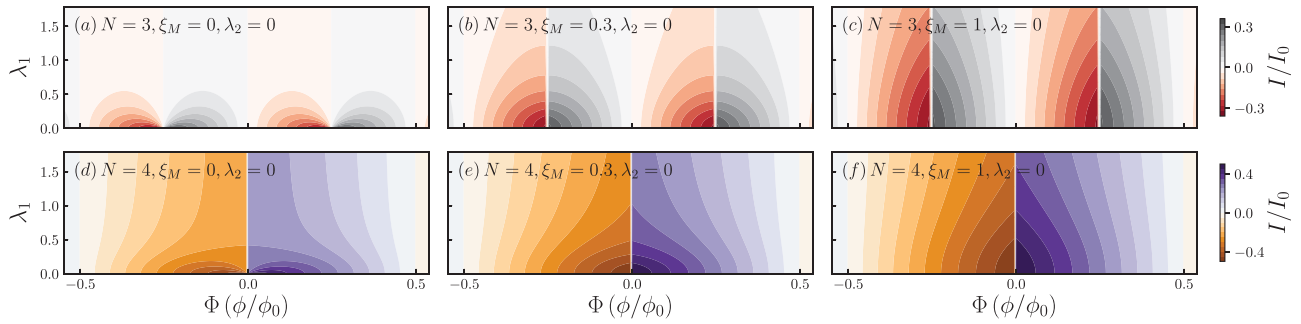


**Figure 7.** Dimensionless persistent current  $I/I_0$ , where  $I_0 = 2ve/\hbar$ , as a function of the dimensionless magnetic flux  $\Phi$  and the coupling with the TSC  $\lambda_1$  for fixed  $\lambda_2 = 0$ . We used  $\xi_M = 0$  [(a) and (d)],  $\xi_M = 0.3$  [(b) and (e)], and  $\xi_M = 1$  [(c) and (f)].  $N = 3$  is used in upper panels and  $N = 4$  in lower panels.

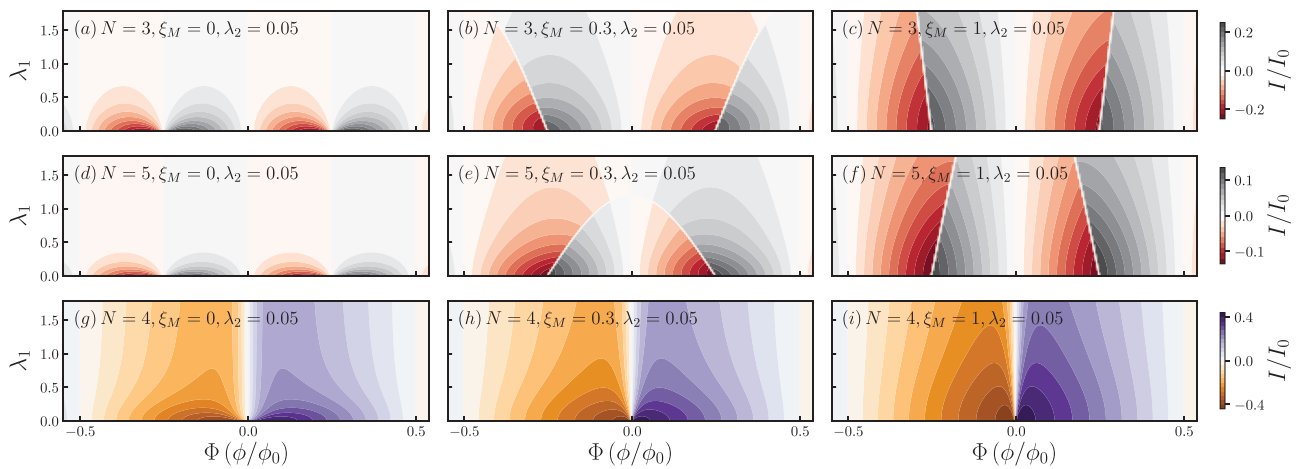


**Figure 8.** Dimensionless persistent current  $I/I_0$ , where  $I_0 = 2ve/\hbar$ , as a function of the dimensionless magnetic flux  $\Phi$  and the coupling with the TSC  $\lambda_1$ . We used  $\xi_M = 0$  [(a), (d) and (g)],  $\xi_M = 0.3$  [(b), (e) and (h)], and  $\xi_M = 1$  [(c), (f) and (i)].  $N = 3$  is used in upper panels,  $N = 5$  in the middle panels and  $N = 4$  in lower panels.

even parity, the ring spectra only presents bowtie pattern. These behaviors can be understood from the MBSs switching condition given by Equation (19) which determines the inward/outward behavior as  $\lambda_1$  is increased in the asymmetric pattern. This condition is better reflected in the contour plots exhibited in Figure 8, panels (b), (c), (e), and (f).

Furthermore, persistent current signals due to the contribution of the three energy patterns were computed, where the discontinuity in this specific curves indicates the change of local parity for the MBSs. Additionally, in the limit of MZM  $\xi_M \rightarrow 0$  and  $\lambda_2 \rightarrow 0$  are distinguished two cases the gapless and gapped spectra for even and odd quantum ring parity respectively. In the gapless case, there is a contribution to the persistent current coming from the states that only hybridize with  $\eta_2$ . This contribution is determined by the discontinuity in the persistent current and remains for any value that could have  $\lambda_1$ , as it is observed in panels (d)–(f) of Figure 7. On the other hand, for gapped spectra the persistent current does not present any discontinuity. Hence only the first case can be of use for the detection of the MZM.

The results presented in this work are complementary to those reported in refs. [34] and [35], where an important aspect to remark about the latter, together with refs. [45,46], is that those studies consider transport properties where, apart from the magnetic flux,

also bias voltage is taking into account. In this sense, our work represents a different approach to the possibility of detection of Majorana bound states in a quantum system. It provides the conditions for which the change in the MBSs fermionic parity is allowed, by using a static perturbation (magnetic flux), the occurrence of persistent currents within the quantum ring, and the observed modifications due to the interactions with the MBS. We believe that the information provided in this article, specifically to the conditions for which the system allows the change in the MBSs parity, could be useful for the implementation of breeding techniques by attaching multiple nanowires to the quantum ring.

## Appendix A: Superconducting Quantum Ring

The Hamiltonian for this model will have the first term of Equation (1) and the BCS superconducting term. The Hamiltonian writes

$$H_S = \sum_{k\sigma} \epsilon_k(\Phi) c_{k\sigma}^\dagger c_{k\sigma} + \sum_k \left( \Delta c_{k\uparrow}^\dagger c_{-k\downarrow}^\dagger + h.c. \right) \quad (\text{A1})$$

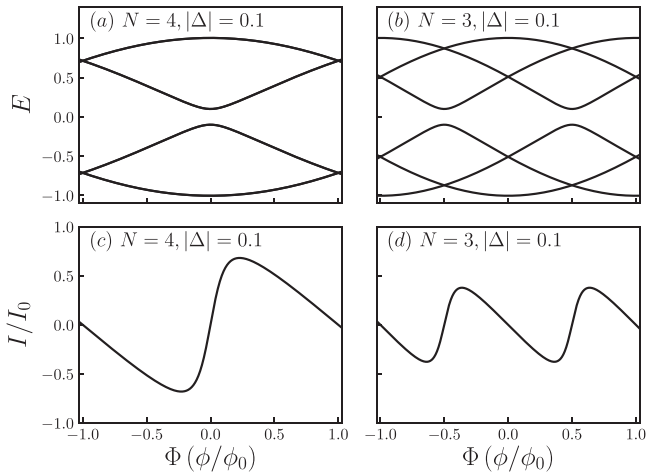


**Figure A1.** Spectra for a quantum ring with superconductivity (a) for  $N = 4$  and (b) for  $N = 3$ , related persistent currents (c) and (d).

where  $\sigma = \uparrow, \downarrow$ ,  $\epsilon_k(\Phi) = \cos[2\pi n/N + (2\pi/N)\Phi]$  and  $\Delta$  is and homogeneous superconducting gap. It is easy to obtain the spectrum by writing the BdG form of the theory given by

$$H_S = \frac{1}{2} \sum_k \Psi_k^\dagger H_{\text{BdG}} \Psi_k \quad (\text{A2})$$

where  $\Psi_k = (c_k \uparrow, c_{-k} \downarrow, c_{-k}^\dagger, c_k^\dagger)^T$ , and we let the factor  $1/2$  to be absorbed by the amplitudes, measuring in units of  $2\nu$ . Hence, we need to diagonalize  $H_{\text{BdG}}$  with energies given by

$$E_\pm = \pm \sqrt{\epsilon_k^2(\Phi) + |\Delta|^2} \quad (\text{A3})$$

where it is the gapped spectrum for superconductivity. We can observe in **Figure A1** the quantum flux  $\phi_0 = h/2e$  now it is defined as twice the charge due to the Cooper pairing, different from the  $\phi_0$  used for the quantum ring in the main calculations of this document. These calculations has been included here in order to compare with the spectra and persistent currents obtained in the main results of this work.

## Appendix B: Green's Functions Calculation

The Green's function of the electrons moving through the localized states in the ring is written as

$$G^\sigma(t) = -i\theta(t) \langle \{c_k(t), c_k^\dagger(0)\} \rangle \quad (\text{B1})$$

We can represent a fermionic state in its real and imaginary part by the transformation  $c_k = (\alpha_k^{(1)} + i\alpha_k^{(2)})/\sqrt{2}$  and  $c_k^\dagger = (\alpha_k^{(1)} - i\alpha_k^{(2)})/\sqrt{2}$ . Therefore, the Green's function can be written as

$$G^\sigma(t) = \frac{1}{2}(A_{(11)}(t) + A_{(22)}(t)) + i\frac{1}{2}(B_{(21)}(t) - B_{(12)}(t)) \quad (\text{B2})$$

where

$$\begin{aligned} A_{(11)}(t) &= -i\theta(t) \langle \{ \alpha_k^{(1)}(t), \alpha_k^{(1)}(0) \} \rangle \\ A_{(22)}(t) &= -i\theta(t) \langle \{ \alpha_k^{(2)}(t), \alpha_k^{(2)}(0) \} \rangle \\ B_{(12)}(t) &= -i\theta(t) \langle \{ \alpha_k^{(1)}(t), \alpha_k^{(2)}(0) \} \rangle \\ B_{(21)}(t) &= -i\theta(t) \langle \{ \alpha_k^{(2)}(t), \alpha_k^{(1)}(0) \} \rangle \end{aligned} \quad (\text{B3})$$

As we are interested only in the poles of the Green's function is enough to work with the first Green's function of Equation (B3). We follow a standard procedure of the equation of motion technique, which implies the use of the Heisenberg's equation. In other words we solve the commutator  $[H, \alpha_k^{(1)}(t)]$ , with the Hamiltonian given by Equation (1). Then, we have got four differential equations. The first one representing the Green's function  $A_{(11)}$ , the second  $B_{(21)}$  that appears as an anomalous Green's function and the other two that correlates  $\eta_1$ ,  $\eta_2$ , and  $\alpha_k^{(1)}$ . By a Fourier's transformation we leave the equations in the energy domain  $\epsilon$  and solve it analytically. This system of equations is

$$\begin{aligned} (\epsilon^2 - \epsilon_n^2)A_{(11)}(\epsilon) + \lambda_1 \epsilon_n C(\epsilon) + i\epsilon \lambda_2 D(\epsilon) &= \epsilon \\ (\epsilon^2 - \epsilon_n^2)B_{(12)}(\epsilon) - i\epsilon \lambda_1 C(\epsilon) + \epsilon_n \lambda_2 D(\epsilon) &= -i\epsilon_n \\ \epsilon^2 \tilde{a} C(\epsilon) - i\epsilon \tilde{b} D(\epsilon) &= -\lambda_1 \epsilon \tilde{c} \\ \epsilon^2 \tilde{f} C(\epsilon) + i\epsilon \tilde{b} D(\epsilon) &= i\lambda_2 \epsilon \tilde{w} \end{aligned} \quad (\text{B4})$$

where  $\tilde{a} = 1 - \frac{\lambda_2^2}{2\epsilon} \sum_{n'} (g^{(-)}(\epsilon, n') + g^{(+)}(\epsilon, n'))$ ,  $\tilde{f}$  is just like  $\tilde{a}$  but instead  $\lambda_1$  we have got  $\lambda_2$ ,  $\tilde{c}$ ,  $\tilde{w}$  both has a difference in a sign as  $\tilde{c} = \frac{1}{2} \sum_{n'} (g^{(-)}(\epsilon, n') - g^{(+)}(\epsilon, n'))$ , and  $\tilde{w} = \frac{1}{2} \sum_{n'} (g^{(-)}(\epsilon, n') + g^{(+)}(\epsilon, n'))$ , finally we can write  $\tilde{b}$  in terms of  $\tilde{c}$  as  $\tilde{b} = \lambda_1 \lambda_2 \tilde{c} + \xi_M$  solving for  $A_{(11)}(\epsilon)$  we can find Equation (14).

## Acknowledgements

F.G.M. is grateful for the funding of scholarship CONICYT-Chile No. 21170550. J.P.R.-A is grateful for the funding of FONDECYT Postdoc. Grant No. 3190301 (2019). L.R. and P.A.O. acknowledge support from FONDECYT Grants 1180914 and 1201876, and Grant USM-DGIIP PI-LI 19-19.

## Conflict of Interest

The authors declare no conflict of interest.

## Keywords

Majorana bound states, persistent currents, quantum rings

Received: April 20, 2020  
Revised: July 7, 2020  
Published online:

- [1] E. Majorana, *Il Nuovo Cimento* **1937**, *14*, 171.
- [2] J. Alicea, *Nat. Phys.* **2016**, *531*, 177.
- [3] J. Alicea, Y. Oreg, G. Refael, F. Von Oppen, M. P. Fisher, *Nat. Phys.* **2011**, *7*, 412.
- [4] K. Law, P. A. Lee, T. Ng, *Phys. Rev. Lett.* **2009**, *103*, 237001.
- [5] L. Fu, C. L. Kane, *Phys. Rev. B* **2009**, *79*, 161408(R).
- [6] L. Jiang, T. Kitagawa, J. Alicea, A. Akhmerov, D. Pekker, G. Refael, J. I. Cirac, E. Demler, M. D. Lukin, P. Zoller, *Phys. Rev. Lett.* **2011**, *106*, 220402.
- [7] R. Pan, C. W. Clark, *Phys. Rev. A* **2018**, *98*, 033604.
- [8] A. Y. Kitaev, *Phys. Usp.* **2001**, *44*, 131.
- [9] R. Lutchyn, E. Bakkers, L. P. Kouwenhoven, P. Krogstrup, C. Marcus, Y. Oreg, *Nat. Rev. Mater.* **2018**, *3*, 52.
- [10] M. T. Deng, C. L. Yu, G. Y. Huang, M. Larsson, P. Caroff, H. Q. Xu, *Nano Lett.* **2012**, *12*, 6414.
- [11] V. Mourik, K. Zuo, S. M. Frolov, S. Plissard, E. P. Bakkers, L. P. Kouwenhoven, *Science* **2012**, *336*, 1003.
- [12] E. J. H. Lee, X. Jiang, R. Aguado, G. Katsaros, C. M. Lieber, S. De Franceschi, *Phys. Rev. Lett.* **2012**, *109*, 186802.
- [13] S. M. Albrecht, A. Higginbotham, M. Madsen, F. Kuemmeth, T. S. Jespersen, J. Nygård, P. Krogstrup, C. Marcus, *Nat. Phys.* **2016**, *531*, 206.
- [14] A. Das, Y. Ronen, Y. Most, Y. Oreg, M. Heiblum, H. Shtrikman, *Nat. Phys.* **2012**, *8*, 887.
- [15] H. O. H. Churchill, V. Fatemi, K. Grove-Rasmussen, M. T. Deng, P. Caroff, H. Q. Xu, C. M. Marcus, *Phys. Rev. B* **2013**, *87*, 241401(R).
- [16] D. E. Liu, H. U. Baranger, *Phys. Rev. B* **2011**, *84*, 201308(R).
- [17] S. Smirnov, *Phys. Rev. B* **2015**, *92*, 195312.
- [18] E. Vernek, P. H. Penteado, A. C. Seridonio, J. C. Egues, *Phys. Rev. B* **2014**, *89*, 165314.
- [19] W. J. Gong, S. F. Zhang, Z. C. Li, G. Yi, Y. S. Zheng, *Phys. Rev. B* **2014**, *89*, 245413.
- [20] D. Zambrano, J. P. Ramos-Andrade, P. A. Orellana, *J. Phys. Condens. Matter* **2018**, *30*, 375301.
- [21] M. T. Deng, S. Vaitiekėnas, E. Prada, P. San-Jose, J. Nygård, P. Krogstrup, R. Aguado, C. Marcus, *Phys. Rev. B* **2018**, *98*, 085125.
- [22] S. Manna, P. Wei, Y. Xie, K. T. Law, P. A. Lee, J. S. Moodera, *Proc. Natl. Acad. Sci. USA* **2020**, *117*, 8775.
- [23] M. Büttiker, Y. Imry, R. Landauer, *Phys. Lett. A* **1983**, *96*, 365.
- [24] A. Fuhrer, S. Lüscher, T. Ihn, T. Heinzel, K. Ensslin, W. Wegscheider, M. Bichler, *Nat. Phys.* **2001**, *413*, 822.
- [25] S. Oh, C. M. Ryu, *Phys. Rev. B* **1995**, *51*, 13441.
- [26] H. F. Cheung, Y. Gefen, E. K. Riedel, W. H. Shih, *Phys. Rev. B* **1988**, *37*, 6050.
- [27] P. Orellana, M. Pacheco, *Phys. Rev. B* **2005**, *71*, 235330.
- [28] H. K. Yadalam, U. Harbola, *Phys. Rev. B* **2016**, *94*, 115424.
- [29] X. Chen, Z. Y. Deng, W. Lu, S. Shen, *Phys. Rev. B* **2000**, *61*, 2008.
- [30] T. Chakraborty, P. Pietiläinen, *Phys. Rev. B* **1994**, *50*, 8460.
- [31] M. Keck, D. Rossini, R. Fazio, *Phys. Rev. A* **2018**, *98*, 053812.
- [32] W. J. Gong, Y. Zhao, Z. Gao, G. Yi, X. Zhang, *J. Phys. Soc. Jpn.* **2015**, *84*, 024707.
- [33] A. Ghazaryan, A. Manaselyan, T. Chakraborty, *Phys. Rev. B* **2016**, *93*, 245108.
- [34] C. K. Chiu, J. D. Sau, S. D. Sarma, *Phys. Rev. B* **2018**, *97*, 035310.
- [35] M. Hell, K. Flensberg, M. Leijnse, *Phys. Rev. B* **2018**, *97*, 161401.
- [36] M. Deng, S. Vaitiekėnas, E. B. Hansen, J. Danon, M. Leijnse, K. Flensberg, J. Nygård, P. Krogstrup, C. M. Marcus, *Science* **2016**, *354*, 1557.
- [37] E. Prada, R. Aguado, P. San-Jose, *Phys. Rev. B* **2017**, *96*, 085418.
- [38] C. Malciu, L. Mazza, C. Mora, *Phys. Rev. B* **2018**, *98*, 165426.
- [39] A. Leggett, D. K. Ferry, J. R. Barker, C. Jacoboni, *Nato ASI Series B* **1991**, 297.
- [40] P. Monisha, I. Sankar, S. Sil, A. Chatterjee, *Sci. Rep.* **2016**, *6*, 1.
- [41] D. J. Clarke, *Phys. Rev. B* **2017**, *96*, 201109.
- [42] T. Takakura, A. Noiri, T. Obata, T. Otsuka, J. Yoneda, K. Yoshida, S. Tarucha, *Appl. Phys. Lett.* **2014**, *104*, 113109.
- [43] G. Bergmann, *Eur. Phys. J. B* **2019**, *92*, 79.
- [44] A. Nava, R. Giuliano, G. Campagnano, D. Giuliano, *PRB* **2017**, *95*, 155449.
- [45] C. X. Liu, W. S. Cole, J. D. Sau, *Phys. Rev. Lett.* **2019**, *122*, 117001.
- [46] K. M. Tripathi, S. Das, S. Rao, *Phys. Rev. Lett.* **2016**, *116*, 166401.

# 3

## Rashba Spin-Orbit in a Quantum-Ring With Majorana Bound States.

The more recurrent question and criticisms to the previous work were whether the model is suitable for actual experimental setups. The questions were based on the difficulty of producing a quantum ring with discretized segments and the case of considering the quantum-ring spinless. Indeed, we can consider a fully polarized quantum ring, and the coupling with the TSC is obtained by constructing a hole structure nanowire and quantum-ring made of the same material, usually InAs or GaAs. The characteristic of those materials is that are chosen due to their high Rashba spin-orbit. Therefore, considering the Rashba strength in the quantum ring provides a more realistic approach to the model. Additionally, the tuning of Rashba strength generates a shifting in the Majorana zero crossings, allowing us to control where the zero energy crossings of the Majoranas modes are produced. Finally, the presence of the two spin states and anisotropy from both states allow us to study spin currents.

### 3.1 Quantum-ring with Rashba Spin-Orbit.

Hence, every site in the quantum ring now has two states, one for a spin up and one for a spin down, as can be seen in Figure 3.1. Here, the version of equation (2.4) for this model is given by:

$$H_R = 2t \sum_{k,\sigma} \cos\left(k + \frac{2\pi}{N}\Phi\right) c_{k,\sigma}^\dagger c_{k,\sigma}. \quad (3.1)$$

Where,  $\sigma$  represents the spin and  $t$  the coupling between sites. For taking into account spin-orbit, we have to couple spin and momentum given a Hamiltonian as:

$$H_{SO} = \alpha \hat{z} \cdot (\vec{\sigma} \times \vec{p}). \quad (3.2)$$

The above Hamiltonian can be written in terms of only two Pauli matrices by operating the cross product:

$$H_{SO} = -i \frac{\alpha}{R} [\sigma_x \cos(\varphi) + \sigma_y \sin(\varphi)] \frac{\partial}{\partial \varphi} \quad (3.3)$$

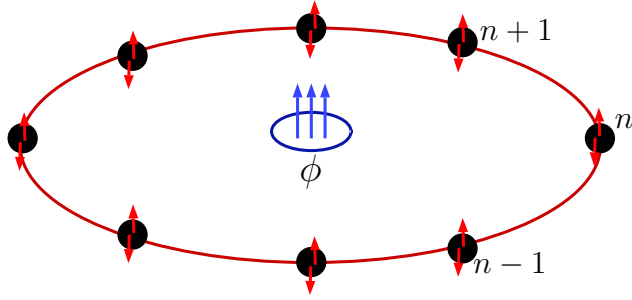


Figure 3.1: Aharonov-Bohm quantum-ring with a two-fold degeneracy of spin.

Here,  $R$  is the radius of the ring and  $\varphi$  is the angular coordinate. We need to represent the Hamiltonian in second quantization and consequently implement finite differences in order to get a discretization of the Hamiltonian. Here we proceed inserting  $1 = \sum_n |\varphi_n\rangle \langle \varphi_n|$  and  $\langle \varphi_{n'} | \varphi_n \rangle = \delta_{n,n'}$ . The action over the fermionic ground state in every ring site is defined as  $c_n^\dagger |0\rangle = |\varphi_n\rangle$ .

$$\begin{aligned} H_{SO} &= - \sum_{n,n'} |\varphi_n\rangle \langle \varphi_n| \mathbf{h}_{so}(\varphi) e^{i\frac{2\pi}{N}\Phi} |\varphi_{n'}\rangle \langle \varphi_{n'}| + h.c. \\ &= - \sum_{n,n'} c_n^\dagger \langle \varphi_n| \mathbf{h}_{so}(\varphi) e^{i\frac{2\pi}{N}\Phi} |\varphi_{n'}\rangle c_{n'} + h.c., \end{aligned} \quad (3.4)$$

with  $\mathbf{h}_{so}(\varphi) = i\frac{\alpha}{R}(\sigma_x \cos(\varphi) + \sigma_y \sin(\varphi)) \frac{\partial}{\partial \varphi}$ . Now we can write the Hamiltonian as follows:

$$H_{SO} = - \sum_n [c_n^\dagger \mathbf{t}_{so}(n) e^{i\frac{2\pi}{N}\Phi} c_{n+1} + h.c.], \quad (3.5)$$

with  $c_n^\dagger = (c_{n,\uparrow}^\dagger, c_{n,\downarrow}^\dagger)$ . The Hamiltonian from the quantum-ring with

$$H_r = H_R + H_{SO} = - \sum_n [c_n^\dagger (\mathbf{t} + \mathbf{t}_{so}(n)) e^{i\frac{2\pi}{N}\Phi} c_{n+1} + h.c.]. \quad (3.6)$$

$\mathbf{t}_{so} = i\tilde{\alpha}(\sigma_x \cos(\varphi_n) + \sigma_y \sin(\varphi_n))$  with  $\tilde{\alpha} = \alpha N/2\pi R$ , here, the discretized angular coordinate is  $\varphi_n = \frac{2\pi}{N}(n - \frac{1}{2})$ . The steps to follow in order to find the spectra for this system consist in the implementation of three unitary transformations, the first one has the objective to remove the position dependence of  $\mathbf{t}_{so}(n)$  paying a cost, which is the mixing of the spins states, the second is a traditional Fourier transformation, but due to the mixing of states the Hamiltonian is not diagonalized and finally a unitary transformation that diagonalize the Hamiltonian. The first unitary transformation is given by:

$$\mathcal{U}_n = \frac{1}{\sqrt{2}} \begin{pmatrix} 1 & -1 \\ e^{i\varphi_n} & e^{i\varphi_n} \end{pmatrix}. \quad (3.7)$$

Here, the operators transform as  $c_n = \mathcal{U}_n \tilde{c}_n$ . This transformation turns out  $H_r$  as a Hamiltonian with couplings independent of the position. After this transformation and a Fourier transformation, we obtain a Hamiltonian given by

$$H_r = \sum_k \tilde{c}_k^\dagger \tilde{\mathbf{h}}_k \tilde{c}_k. \quad (3.8)$$

With,

$$\tilde{\mathbf{h}}_k = -\cos\left(\frac{\pi}{N}\right)\cos\left(k + \theta + \frac{\pi}{N}\right)\sigma_0 + \sin\left(k + \theta + \frac{\pi}{N}\right) \times \left[\sin\left(\frac{\pi}{N}\right)\sigma_x - 2\tilde{\alpha}\sin\left(\frac{\pi}{N}\right)\sigma_y + 2\tilde{\alpha}\cos\left(\frac{\pi}{N}\right)\sigma_z\right] \quad (3.9)$$

We can diagonalize the above Hamiltonian. If we write the Hamiltonian on the diagonal basis, we obtain:

$$H_r = \sum_{n,\mu=\pm} \varepsilon_{n,\mu} d_{n,\mu}^\dagger d_{n,\mu}. \quad (3.10)$$

To obtain the above Hamiltonian, we should implement the following unitary transformation:

$$\mathcal{U} = \begin{pmatrix} \psi_-^u & \psi_+^u \\ \psi_-^d & \psi_+^d \end{pmatrix}. \quad (3.11)$$

Where the sub-index  $\pm$  represent the pseudospin (since we have now mixed spins states) and the upper index  $u, d$  are the labels for the two-component spinor given by:

$$\psi_\pm = \begin{pmatrix} \psi_\pm^u \\ \psi_\pm^d \end{pmatrix}, \quad (3.12)$$

the fermionic operators transform as  $d_k = \mathcal{U}\tilde{c}_k$ . The spinor components are given by

$$\psi_\pm^u = \frac{u_\pm}{\sqrt{1 + |u_\pm|^2}}, \quad \psi_\pm^d = \frac{1}{\sqrt{1 + |u_\pm|^2}}, \quad (3.13)$$

the  $u_\pm$  terms are:

$$u_\pm = \frac{2\tilde{\alpha}\cos\left(\frac{\pi}{N}\right) \pm \sqrt{\sin^2\left(\frac{\pi}{N}\right) + 4\tilde{\alpha}^2}}{(1 - 2i\tilde{\alpha})\sin\left(\frac{\pi}{N}\right)}. \quad (3.14)$$

The spectrum for the quantum ring writes as

$$\varepsilon_\pm = -\cos\left(\frac{\pi}{N}\right)\cos\left(\frac{2\pi}{N}\left(n + \frac{1}{2} + \Phi\right)\right) \pm \sin\left(\frac{2\pi}{N}\left(n + \frac{1}{2} + \Phi\right)\right)\sqrt{\sin^2\left(\frac{\pi}{N}\right) + 4\tilde{\alpha}^2}. \quad (3.15)$$

Hence, if  $\alpha = 0$  the expression is reduced to the spectrum of the single ring, but in this case twofold degenerate.

### 3.1.1 Topological Superconductor Coupled to a Quantum-Ring.

Given that the TSC is a p-wave superconductor and, in consequence, the nanowire is fully polarized, the coupling with the quantum ring is given only to one spin state. Here, we describe the coupling and how this Hamiltonian results after the transformations as mentioned above. Hence, the Hamiltonian in position space is written as:

$$H_c = \lambda_1 (c_{1,\uparrow}^\dagger - c_{1,\uparrow}) \gamma_1 + i\lambda_2 (c_{1,\uparrow}^\dagger + c_{1,\uparrow}) \gamma_2. \quad (3.16)$$

By expressing the Majorana operator in terms of the Dirac representation and changing the base for the  $c$  operators

$$\begin{aligned} \gamma_1 &= \frac{1}{\sqrt{2}} (f^\dagger + f); & \gamma_2 &= \frac{i}{\sqrt{2}} (f^\dagger - f) \\ c_{1,\uparrow} &= \frac{1}{\sqrt{2}} (\tilde{c}_{1,a} - \tilde{c}_{1,b}); & c_{1,\downarrow} &= \frac{1}{\sqrt{2}} e^{i\frac{2\pi}{N}(1-\frac{1}{2})} (\tilde{c}_{1,a} + \tilde{c}_{1,b}). \end{aligned} \quad (3.17)$$

The Majoranas coupled only to one of the two spin states, and here we choose the coupling to spin up. Therefore, the Hamiltonian can be written as:

$$H_c = (\tilde{c}_{1,a}^\dagger - \tilde{c}_{1,b}^\dagger) (\lambda_- f^\dagger + \lambda_+ f) + (\lambda_- f + \lambda_+ f^\dagger) (\tilde{c}_{1,a} - \tilde{c}_{1,b}). \quad (3.18)$$

where  $\lambda_\pm = \frac{1}{2}(\lambda_1 \pm \lambda_2)$ . The next transformation is a straightforward Fourier transformation. and the Hamiltonian writes as:

$$H_c = \sum_n e^{-i\frac{2\pi n}{N}} [(\tilde{c}_{n,a}^\dagger - \tilde{c}_{n,b}^\dagger) (\lambda_- f^\dagger + \lambda_+ f)] + h.c. \quad (3.19)$$

The final unitary transformation is given by Eq. (3.11). The above Hamiltonian transform as:

$$H_c = \sum_n e^{i\frac{2\pi n}{N}} \left\{ [(\psi_-^u - \psi_+^u) d_{n,-}^\dagger + (\psi_-^d - \psi_+^d) d_{n,+}^\dagger] (\lambda_- f^\dagger + \lambda_+ f) \right\} + h.c. \quad (3.20)$$

Finally, by defining  $\beta_{n,-} = e^{-i2\pi n/N} (\psi_-^u - \psi_+^u)$  and  $\beta_{n,+} = e^{-i2\pi n/N} (\psi_-^d - \psi_+^d)$  the Hamiltonian take the form:

$$H_c = \sum_{n,\mu=\pm} [\beta_{n,\mu} d_{n,\mu}^\dagger (\lambda_- f^\dagger + \lambda_+ f) - \beta_{n,\mu}^* d_{n,\mu} (\lambda_- f + \lambda_+ f^\dagger)]. \quad (3.21)$$

### 3.1.2 Charge and Spin Persistent Currents.

Persistent current, as was presented in the previous chapter, originates from time-reversal symmetry breaking and is very simple to find by taking the variation of the spectra with respect to the magnetic flux. Hence, when inversion symmetry is broken, spin persistent currents are obtained. In order to compute persistent spin currents, it is necessarily a different approach since the spectrum modes appear mixed, and we can not distinguish between spin down and spin up modes. Hence, Green's function calculations are implemented to obtain an expression for the currents. Therefore, we should start with the derivative in time of the total number and the difference in of a number of particles spin up and spin down.

$$I_p = \langle \dot{N}_\uparrow + \dot{N}_\downarrow \rangle, \quad I_s = \langle \dot{N}_\uparrow - \dot{N}_\downarrow \rangle. \quad (3.22)$$

What is important is that the calculation must be done first in the position space to find a correct expression for the currents. Therefore, let us start with a Hamiltonian under the first unitary transformation. Thus, the Hamiltonian for the ring is given by:

$$\begin{aligned}
H_r = & - \sum_n e^{i(\frac{\pi}{N} + \theta)} \left[ \left( \frac{1}{2} + i\tilde{\alpha} \right) \cos \left( \frac{\pi}{N} \right) \tilde{c}_{n,a}^\dagger \tilde{c}_{n+1,a} + \left( \frac{i}{2} + \tilde{\alpha} \right) \sin \left( \frac{\pi}{N} \right) \tilde{c}_{n,b}^\dagger \tilde{c}_{n+1,a} \right. \\
& \left. + \left( \frac{i}{2} - \tilde{\alpha} \right) \sin \left( \frac{\pi}{N} \right) \tilde{c}_{n,a}^\dagger \tilde{c}_{n+1,b} + \left( \frac{1}{2} - i\tilde{\alpha} \right) \cos \left( \frac{\pi}{N} \right) \tilde{c}_{n,b}^\dagger \tilde{c}_{n+1,b} + h.c. \right]. \quad (3.23)
\end{aligned}$$

For the coupling Hamiltonian, we use Eq. (3.18), and for the Majoranas, we use Eq. (2.28) in Dirac representation. So now, from the Heisenberg equation, we can write the commutators for the persistent charge current and the persistent spin current.

$$[N_\uparrow + N_\downarrow, H] = [\tilde{c}_{n,a}^\dagger \tilde{c}_{n,a} + \tilde{c}_{n,b}^\dagger \tilde{c}_{n,b}, H] \quad (3.24)$$

and for computing spin currents, we have:

$$[N_\uparrow - N_\downarrow, H] = - [\tilde{c}_{n,a}^\dagger \tilde{c}_{n,b} + \tilde{c}_{n,b} \tilde{c}_{n,a}, H]. \quad (3.25)$$

The commutator Eq. (3.24) provides the result:

$$\begin{aligned}
& [\tilde{c}_{n,a}^\dagger \tilde{c}_{n,a} + \tilde{c}_{n,b} \tilde{c}_{n,b}, H] = -e^{i(\frac{\pi}{N} + \theta)} \left\{ \left( \frac{i}{2} - \tilde{\alpha} \right) \sin \left( \frac{\pi}{N} \right) \tilde{c}_{n,a}^\dagger \tilde{c}_{n+1,b} \right. \\
& + \left( \frac{i}{2} + \tilde{\alpha} \right) \sin \left( \frac{\pi}{N} \right) \tilde{c}_{n,b}^\dagger \tilde{c}_{n+1,a} + \left( \frac{1}{2} + i\tilde{\alpha} \right) \cos \left( \frac{\pi}{N} \right) \tilde{c}_{n,a}^\dagger \tilde{c}_{n+1,a} \\
& + \left. \left( \frac{1}{2} - i\tilde{\alpha} \right) \cos \left( \frac{\pi}{N} \right) \tilde{c}_{n,b}^\dagger \tilde{c}_{n+1,b} \right\} + e^{-i(\frac{\pi}{N} + \theta)} \left\{ \left( \frac{1}{2} - i\tilde{\alpha} \right) \cos \left( \frac{\pi}{N} \right) \tilde{c}_{n+1,a}^\dagger \tilde{c}_{n,a} \right. \\
& + \left( -\frac{i}{2} - \tilde{\alpha} \right) \sin \left( \frac{\pi}{N} \right) \tilde{c}_{n+1,b}^\dagger \tilde{c}_{n,a} + \left( -\frac{i}{2} + \tilde{\alpha} \right) \sin \left( \frac{\pi}{N} \right) \tilde{c}_{n+1,a}^\dagger \tilde{c}_{n,b} \\
& + \left. \left( \frac{1}{2} + i\tilde{\alpha} \right) \cos \left( \frac{\pi}{N} \right) \tilde{c}_{n+1,b}^\dagger \tilde{c}_{n,b} \right\} + [N_\uparrow + N_\downarrow, H_c], \quad (3.26)
\end{aligned}$$

since we are interested only in the persistent currents, the terms from the current coming from the coupling Hamiltonian are not taken into account here. Hence, the commutator after momentum transformation is written as:

$$\begin{aligned}
[N_\uparrow + N_\downarrow, H_r] = & \sum_k \left\{ (-i + 2\tilde{\alpha}) \sin \left( \frac{\pi}{N} \right) \cos \left( \frac{\pi}{N} + \theta + k \right) \tilde{c}_{k,a}^\dagger \tilde{c}_{k,b} \right. \\
& + (-i - 2\tilde{\alpha}) \sin \left( \frac{\pi}{N} \right) \cos \left( \frac{\pi}{N} + \theta + k \right) \tilde{c}_{k,b}^\dagger \tilde{c}_{k,a} \\
& + i \left( \sin \left( \frac{\pi}{N} + \theta + k \right) - 2\tilde{\alpha} \cos \left( \frac{\pi}{N} + \theta + k \right) \right) \cos \left( \frac{\pi}{N} \right) \tilde{c}_{k,a}^\dagger \tilde{c}_{k,a} \\
& + i \left( -\sin \left( \frac{\pi}{N} + \theta + k \right) + 2\tilde{\alpha} \cos \left( \frac{\pi}{N} + \theta + k \right) \right) \cos \left( \frac{\pi}{N} \right) \tilde{c}_{k,b}^\dagger \tilde{c}_{k,b} \left. \right\}. \quad (3.27)
\end{aligned}$$

The persistent current is given by the following expression:

$$\begin{aligned}
I_p &= -i \langle [N_\uparrow + N_\downarrow, H_r] \rangle = - \sum_k \left\{ (1 + 2i\tilde{\alpha}) \sin\left(\frac{\pi}{N}\right) \cos\left(\frac{\pi}{N} + \theta + k\right) \langle \tilde{c}_{k,a}^\dagger \tilde{c}_{k,b} \rangle \right. \\
&\quad (1 - 2i\tilde{\alpha}) \sin\left(\frac{\pi}{N}\right) \cos\left(\frac{\pi}{N} + \theta + k\right) \langle \tilde{c}_{k,b}^\dagger \tilde{c}_{k,a} \rangle \\
&\quad \left. \left( \sin\left(\frac{\pi}{N} + \theta + k\right) + 2\tilde{\alpha} \cos\left(\frac{\pi}{N} + \theta + k\right) \right) \cos\left(\frac{\pi}{N}\right) \langle \tilde{c}_{k,a}^\dagger \tilde{c}_{k,a} \rangle \right. \\
&\quad \left. \left( \sin\left(\frac{\pi}{N} + \theta + k\right) - 2\tilde{\alpha} \cos\left(\frac{\pi}{N} + \theta + k\right) \right) \cos\left(\frac{\pi}{N}\right) \langle \tilde{c}_{k,b}^\dagger \tilde{c}_{k,b} \rangle \right\}. \tag{3.28}
\end{aligned}$$

Under a final transformation. We pass from the  $\tilde{c}_{k,a/b}$  operators to the  $d_{k,\pm}$  operators. Hence, we obtain:

$$I_p = - \sum_k \left[ \chi_k \langle d_{k,-}^\dagger d_{k,-} \rangle + \gamma_k \langle d_{k,+}^\dagger d_{k,+} \rangle + 2\text{Re} \left\{ \beta_k \langle d_{k,-}^\dagger d_{k,+} \rangle \right\} \right] \tag{3.29}$$

where the coefficients are given by:

$$\begin{aligned}
\chi_k &= A_k^+ |\psi_-^u|^2 + A_k^- |\psi_+^u|^2 + 2\text{Re} \left\{ B_k \psi_-^u (\psi_+^u)^* \right\} \\
\gamma_k &= A_k^+ |\psi_-^d|^2 + A_k^- |\psi_+^d|^2 + 2\text{Re} \left\{ B_k \psi_-^d (\psi_+^d)^* \right\} \\
\beta_n &= A_k^+ \psi_-^u (\psi_-^d)^* + A_k^- \psi_+^u (\psi_+^d)^* + B_k \psi_-^u (\psi_+^d)^* + B_k^* \psi_+^u (\psi_-^d)^* \tag{3.30}
\end{aligned}$$

The fluctuation-dissipation theorem connects the average values  $\langle \rangle$  with Green's function. If it is known the Green's functions, we can calculate the currents. Hence, the fluctuation-dissipation theorem writes:

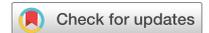
$$\langle AB \rangle = \int_{-\infty}^{\infty} d\omega \left( -\frac{1}{\pi} \right) f(\omega) \text{Im} \langle \langle A; B \rangle \rangle_\omega \tag{3.31}$$

Therefore, a final expression for the persistent current, is given by:

$$\begin{aligned}
I_p &= - \sum_k \frac{1}{\pi} \int_{-\infty}^{\infty} d\omega f(\omega) \left[ \chi_k \text{Im} \langle \langle d_{k,-}; d_{k,-}^\dagger \rangle \rangle_\omega + \gamma_k \text{Im} \langle \langle d_{k,+}; d_{k,+}^\dagger \rangle \rangle_\omega \right. \\
&\quad \left. + 2\text{Re} \left\{ \beta_n \langle \langle d_{k,-}; d_{k,+}^\dagger \rangle \rangle_\omega \right\} \right]. \tag{3.32}
\end{aligned}$$

The expression for the persistent spin current is similar to the charge persistent currents, actually is identical with some changes in the coefficients. Those are  $\sin \rightarrow \cos$  in  $A_k$  and  $B_k$  also  $\tilde{\alpha} \rightarrow -\tilde{\alpha}$  in  $B_K$  or equivalently taking the complex in  $B_k$  for all coefficients. Therefore, we can write:

$$\begin{aligned}
I_{p(s)} &= - \sum_k \frac{1}{\pi} \int_{-\infty}^{\infty} d\omega f(\omega) \left[ \chi_k^{p(s)} \text{Im} \langle \langle d_{k,-}; d_{k,-}^\dagger \rangle \rangle_\omega + \gamma_k^{p(s)} \text{Im} \langle \langle d_{k,+}; d_{k,+}^\dagger \rangle \rangle_\omega \right. \\
&\quad \left. + 2\text{Re} \left\{ \beta_n^{p(s)} \langle \langle d_{k,-}; d_{k,+}^\dagger \rangle \rangle_\omega \right\} \right]. \tag{3.33}
\end{aligned}$$



OPEN

# Manipulation of Majorana bound states in proximity to a quantum ring with Rashba coupling

Fabián Gonzalo Medina<sup>1,4</sup>, Dunkan Martínez<sup>2,4</sup>, Álvaro Díaz-Fernández<sup>3</sup>, Francisco Domínguez-Adame<sup>2</sup>, Luis Rosales<sup>1</sup> & Pedro A. Orellana<sup>1</sup>

The quest for Majorana zero modes in the laboratory is an active field of research in condensed matter physics. In this regard, there have been many theoretical proposals; however, their experimental detection remains elusive. In this article, we present a realistic setting by considering a quantum ring with Rashba spin-orbit coupling and threaded by a magnetic flux, in contact with a topological superconducting nanowire. We focus on spin-polarized persistent currents to assess the existence of Majorana zero modes. We find that the Rashba spin-orbit coupling allows for tuning the position of the zero energy crossings in the flux parameter space and has sizable effects on spin-polarized persistent currents. We believe that our results will contribute towards probing the existence of Majorana zero modes.

Majorana fermions remain a theoretical construct in the realm of particle physics. These particles, whose main feature is to be their own antiparticles, have been sought after in neutrinos, although without success thus far<sup>1,2</sup>. In condensed matter physics, Majorana quasiparticles emerge in *p*-wave topological superconductors<sup>3,4</sup>. Of particular relevance are the so-called Majorana zero modes (MZM)<sup>2</sup>, which are zero-energy Majorana quasiparticles protected by particle-hole symmetry. These quasiparticles, in contrast to their particle counterparts, exhibit yet another crucial feature. Such property is their being non-Abelian under braiding, which renders these quasiparticles as ideal candidates to perform topological quantum computing<sup>5,6</sup>. The reason for this stems in the large degeneracy found in the ground state of a system comprising a large number of Majorana quasiparticles. This degeneracy occurs due to these zero modes being pinned to zero energy<sup>4</sup>.

The archetypal model for studying Majorana modes in superconductors is that of Kitaev<sup>7–9</sup>, where a one-dimensional spinless *p*-wave superconductor is considered. Under suitable tuning of parameters, the model predicts that an ordinary superconductor undergoes a topological quantum phase transition into a topological superconductor. When considering open boundary conditions, the model predicts an odd number of MZMs at both ends of the chain with exponential decay into the bulk. Kitaev's model, although simple, poses significant challenges for its experimental realization. However, a great deal of experimental advances have taken place during the last few years, and a convenient setting has been put forward<sup>4,10–12</sup>. Such a setting has three key ingredients: a semiconductor nanowire with large spin-orbit coupling, such as InAs and InSb, a uniform magnetic field parallel to the wire to induce Zeeman splitting, and an *s*-wave superconductor such as Al. When placed in contact with the semiconductor and applying the magnetic field, the superconductor becomes topological when a given magnetic field is reached.

In this paper, we consider a superconducting nanowire in the topological regime placed in contact to a quantum ring. We assume the ring to be a continuation of the nanowire, as was done with a quantum dot in Ref.<sup>13</sup>, and therefore it displays strong spin-orbit coupling. The ring is in fact a collection of quantum dots assembled in a ring-like fashion, which can be achieved by means of gate voltages. The main results of this paper relate to the impact of the nanowire on the persistent spin currents of the ring, which are sharply different from those of the ring. As we shall show, when the MZMs interact via the quantum ring, they split from zero energy and oscillate, forming zero energy crossings. These crossings reshape the spin currents that would be present in the absence of Majoranas. Therefore, we believe our proposal could potentially be used as an additional tool to uncover the nature of MZMs.

<sup>1</sup>Departamento de Física, Universidad Técnica Federico Santa María, Casilla 110 V, Valparaíso, Chile. <sup>2</sup>GISC, Departamento de Física de Materiales, Universidad Complutense, 28040 Madrid, Spain. <sup>3</sup>GISC, GSC, Departamento de Estructuras y Física de Edificación, Universidad Politécnica de Madrid, 28031 Madrid, Spain. <sup>4</sup>These authors contributed equally: Fabián Gonzalo Medina and Dunkan Martínez. ✉email: fmmedinacfabian@gmail.com

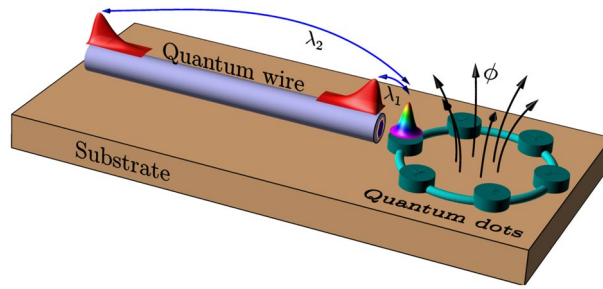


**Figure 1.** (a) Schematic representation of the system under study. A nanowire driven into a superconducting regime supports a MZM at each edge and influences the persistent currents of a quantum ring, threaded by a magnetic flux. (b) The quantum ring consists of an array of quantum dots uniformly distributed on a circumference. The MZMs are assumed to be coupled to the same quantum dot of the ring, with coupling constants  $\lambda_1$  and  $\lambda_2$ .

### System and model Hamiltonian

The system under consideration consists of a topological superconducting nanowire hosting MZMs at its edges, as depicted in Fig. 1a. The nanowire is placed in close proximity to a quantum ring, which is threaded by a magnetic flux. We introduce a minimal model that captures the influence of the MZMs on the persistent currents of the ring. The quantum ring consists of an array of quantum dots uniformly distributed on a circumference, as shown in Fig. 1b. Due to the similarities of our system with the one considered in Refs.<sup>12,13</sup>, we believe that our model might be amenable to be performed experimentally.

The model Hamiltonian is then given by

$$H = H_r + H_M + H_c, \tag{1}$$

where  $H_r$  is the Hamiltonian of the ring,  $H_M$  describes the interaction between the two MZMs at the edges of a nanowire in the topological superconducting regime, and  $H_c$  contains the coupling between the MZMs and the quantum ring. Considering spin-orbit coupling and the fact that the quantum ring is threaded by a flux  $\Phi$ ,  $H_r$  can be written as<sup>14-16</sup>

$$H_r = - \sum_n [c_n^\dagger (t + t_{so}(n)) e^{i\theta} c_{n+1} + \text{h.c.}], \tag{2}$$

where  $c_n^\dagger = (c_{n,\uparrow}^\dagger, c_{n,\downarrow}^\dagger)$  are the creation operators of the quantum ring and  $n$  runs from 1 to  $N$ , with  $N$  the number of sites of the ring, that is, the number of quantum dots that compose it. We shall measure energies in units of  $2t$  with  $t$  the hopping energy, which implies that  $t = \sigma_0/2$ , with  $\sigma_0$  the  $2 \times 2$  identity matrix. The flux is accounted for in the phase factor  $\theta = 2\pi \Phi/N$ , where  $\Phi = \phi/\phi_0$  is the flux  $\phi$  measured in units of the flux quantum  $\phi_0 = h/e$ . The spin-orbit coupling is given by

$$t_{so}(n) = i\tilde{\alpha} (\sigma_x \cos \varphi_n + \sigma_y \sin \varphi_n), \tag{3}$$

where we only consider Rashba spin-orbit interaction, disregarding a possible Dresselhaus interaction<sup>15</sup>. Here,  $\sigma_x$  and  $\sigma_y$  are the Pauli matrices,  $\tilde{\alpha} = \alpha N/2\pi R$  being  $R$  the radius of the ring,  $\alpha$  the strength of the Rashba interaction and

$$\varphi_n = \frac{2\pi}{N} \left( n - \frac{1}{2} \right). \tag{4}$$

Regarding the mutual coupling between MZMs and the coupling between MZMs and the ring, we will consider a low energy theory as in Ref.<sup>17</sup>. Thus, the interaction term between the two MZMs is given by the minimal Kitaev Hamiltonian for the topological phase<sup>7</sup>

$$H_M = i \xi_M \gamma_1 \gamma_2, \tag{5}$$

where  $\gamma_1$  and  $\gamma_2$  are Majorana operators which satisfy  $\gamma_i = \gamma_i^\dagger$  and  $\{\gamma_i, \gamma_j\} = \delta_{ij}$ . Here  $\xi_M \propto e^{-L/\ell_0}$  where  $L$  is the length of the nanowire and  $\ell_0$  is the superconducting coherence length<sup>7</sup>. The Majorana operators can also be written in terms of ordinary fermion operators,  $f$  and  $f^\dagger$ , as

$$\gamma_1 = \frac{1}{\sqrt{2}}(f + f^\dagger), \quad \gamma_2 = \frac{i}{\sqrt{2}}(f - f^\dagger). \tag{6}$$

In terms of these operators, Eq. (5) takes the form

$$H_M = \xi_M \left( f^\dagger f - \frac{1}{2} \right). \tag{7}$$

Finally, the coupling between the MZMs and the quantum ring is given by<sup>17-19</sup>

$$H_c = \lambda_1 \left( c_{1,\uparrow}^\dagger - c_{1,\uparrow} \right) \gamma_1 + i \lambda_2 \left( c_{1,\uparrow}^\dagger + c_{1,\uparrow} \right) \gamma_2, \tag{8}$$

where  $\lambda_1$  and  $\lambda_2$  are real parameters [see also Fig. 1]. We have chosen to couple the MZMs to a single spin. This can be achieved by fixing the spin canting angles of the MZMs accordingly, which can be done by means of sufficiently large magnetic fields<sup>17</sup>. Finally, we will not consider electron-electron interactions in the ring, which could be included within a mean field approximation<sup>16,17</sup>.

It is now convenient to turn to a representation where  $H_r$  is diagonal. For that matter, we can use the following unitary transformation<sup>15</sup>

$$\mathcal{U}_n = \frac{1}{\sqrt{2}} \begin{pmatrix} 1 & -1 \\ e^{i\varphi_n} & e^{i\varphi_n} \end{pmatrix}, \tag{9}$$

so that  $c_n = \mathcal{U}_n \tilde{c}_n$ . This transformation turns  $H_r$  into

$$H_r = - \sum_n \left( \tilde{c}_n^\dagger \mathcal{M} e^{i\theta} \tilde{c}_{n+1} + \text{h.c.} \right). \tag{10}$$

where

$$\mathcal{M} = e^{i\pi/N} \begin{pmatrix} \left( \frac{1}{2} + i\tilde{\alpha} \right) \cos\left(\frac{\pi}{N}\right) & \left( \frac{i}{2} - \tilde{\alpha} \right) \sin\left(\frac{\pi}{N}\right) \\ \left( \frac{i}{2} + \tilde{\alpha} \right) \sin\left(\frac{\pi}{N}\right) & \left( \frac{1}{2} - i\tilde{\alpha} \right) \cos\left(\frac{\pi}{N}\right) \end{pmatrix}. \tag{11}$$

Notice that the unitary transformation has eliminated the site dependence in the hopping matrix in Eq. (10). Thus, by Fourier transforming  $H_r$  we can block-diagonalize it

$$H_r = \sum_k \tilde{c}_k^\dagger \tilde{h}_k \tilde{c}_k, \tag{12}$$

with

$$\tilde{h}_k = - \cos\left(\frac{\pi}{N}\right) \cos\left(k + \theta + \frac{\pi}{N}\right) \sigma_0 + \sin\left(k + \theta + \frac{\pi}{N}\right) \left[ \sin\left(\frac{\pi}{N}\right) \sigma_x - 2\tilde{\alpha} \sin\left(\frac{\pi}{N}\right) \sigma_y + 2\tilde{\alpha} \cos\left(\frac{\pi}{N}\right) \sigma_z \right]. \tag{13}$$

In the basis that diagonalizes  $\tilde{h}_k$  we can write  $H_r$  as

$$H_r = \sum_{n,\mu=\pm} \varepsilon_{n\mu} d_{n\mu}^\dagger d_{n\mu}, \tag{14}$$

where the eigenvalues are

$$\varepsilon_{n,\pm} = - \cos\left(\frac{\pi}{N}\right) \cos\left[\frac{2\pi}{N}\left(n + \frac{1}{2} + \Phi\right)\right] \pm \sin\left[\frac{2\pi}{N}\left(n + \frac{1}{2} + \Phi\right)\right] \sqrt{\sin^2\left(\frac{\pi}{N}\right) + 4\tilde{\alpha}^2}. \tag{15}$$

In this basis,  $H_c$  is written as follows

$$H_c = \sum_{n,\mu=\pm} \left[ \beta_{n,\mu} d_{n,\mu}^\dagger (\lambda_- f^\dagger + \lambda_+ f) - \beta_{n,\mu}^* d_{n,\mu} (\lambda_- f + \lambda_+ f^\dagger) \right], \tag{16}$$

where  $\lambda_\pm = (\lambda_1 \pm \lambda_2)/2$ ,  $\beta_{n,-} = e^{-i2\pi n/N} (\psi_-^u - \psi_+^u)$ ,  $\beta_{n,+} = e^{-i2\pi n/N} (\psi_-^d - \psi_+^d)$  with

$$\begin{aligned} \psi_\pm^u &= u_\pm / \sqrt{1 + |u_\pm|^2}, \\ \psi_\pm^d &= 1 / \sqrt{1 + |u_\pm|^2}, \\ u_\pm &= \frac{2\tilde{\alpha} \cos\left(\frac{\pi}{N}\right) \pm \sqrt{\sin^2\left(\frac{\pi}{N}\right) + 4\tilde{\alpha}^2}}{(1 - 2i\tilde{\alpha}) \sin\left(\frac{\pi}{N}\right)}. \end{aligned} \tag{17}$$

We can now find the spectrum of  $H$  by using the Bogoliubov-de Gennes (BdG) Hamiltonian. Indeed, if we introduce

$$\Psi = (\{d_{n,\mu}\}, f, \{d_{n,\mu}^\dagger\}, f^\dagger)^T, \tag{18}$$

with  $\{d_{n,\mu}\} = d_{1,-}, d_{1,+}, \dots, d_{N,-}, d_{N,+}$  and likewise for  $\{d_{n,\mu}^\dagger\}$ , we can write  $H$  as

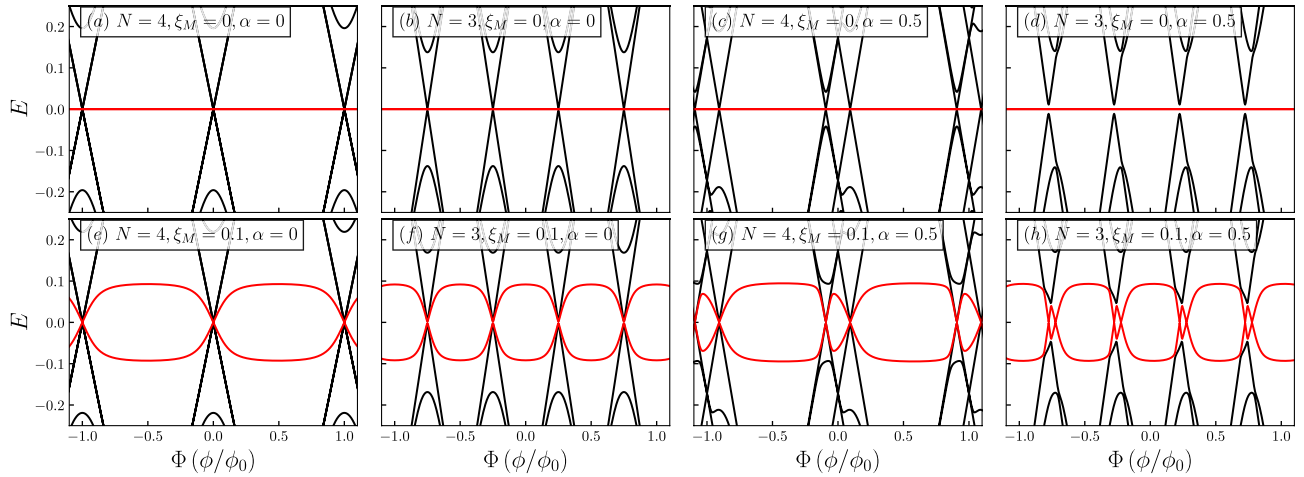


**Figure 2.** Quasiparticle spectra for  $\lambda_1 = 0.1$  and  $\lambda_2 = 0$ . The number of sites,  $N$ , the coupling between MZMs,  $\xi_M$ , and the Rashba spin-orbit coupling,  $\alpha$ , are indicated in the figure. Black curves represent the states in the quantum ring and the red curves correspond to the Majorana modes.

$$H = \frac{1}{2} \Psi^\dagger \mathcal{H}_{\text{BdG}} \Psi, \tag{19}$$

where

$$\mathcal{H}_{\text{BdG}} = \begin{pmatrix} \mathcal{H} & \Lambda \\ -\Lambda^* & -\mathcal{H}^* \end{pmatrix}, \tag{20}$$

is the BdG Hamiltonian. Here,  $\mathcal{H} = \mathcal{H}_0 + \mathcal{V}$  and  $\Lambda$  are the following  $(2N + 1) \times (2N + 1)$  matrices

$$\mathcal{H}_0 = \text{diag}[\varepsilon_{1,-}, \varepsilon_{1,+}, \dots, \varepsilon_{N,-}, \varepsilon_{N,+}, \xi_M] \tag{21}$$

$$\mathcal{V} = \lambda_+ \begin{pmatrix} & & & & \beta_{1,-} \\ & & & & \beta_{1,+} \\ & & \mathbf{0}_{2N} & & \vdots \\ & & & & \beta_{N,-} \\ & & & & \beta_{N,+} \\ \beta_{1,-}^* & \beta_{1,+}^* & \dots & \beta_{N,-}^* & \beta_{N,+}^* \\ & & & & 0 \end{pmatrix} \tag{22}$$

$$\Lambda = \lambda_- \begin{pmatrix} & & & & \beta_{1,-} \\ & & & & \beta_{1,+} \\ & & \mathbf{0}_{2N} & & \vdots \\ & & & & \beta_{N,-} \\ & & & & \beta_{N,+} \\ -\beta_{1,-} & -\beta_{1,+} & \dots & -\beta_{N,-} & -\beta_{N,+} \\ & & & & 0 \end{pmatrix} \tag{23}$$

where  $\mathbf{0}_{2N}$  is the  $2N \times 2N$  zero matrix. The BdG Hamiltonian leads to a particle-hole redundancy and, as a result, the spectrum will be symmetrical around  $E = 0$ . Diagonalization of  $\mathcal{H}_{\text{BdG}}$  provides us with the quasiparticle spectrum,  $E(\Phi)$ .

### Quasiparticle energy spectra

In Figs. 2 and 3, we show the quasiparticle spectrum for rings with  $N = 3$  and  $N = 4$ . The spectra for larger values of  $N$  is provided in the Supplemental Material S1, and restrict to  $N = 3$  and 4 in the remaining of the text. This is mainly for practical reasons, since the larger the number of dots, the harder an experimental implementation would prove to be. In the following, we consider two scenarios, namely  $\lambda_1 = 0.1, \lambda_2 = 0$  and  $\lambda_1 = 0.1, \lambda_2 = 0.15$ , respectively. As explained in Ref.<sup>13</sup>, the quantity  $\eta = \sqrt{\lambda_2/\lambda_1}$  provides a measure of locality and, as reported in that reference, a value of  $\eta \ll 1$  corresponds to highly nonlocal Majoranas, whereas the Majorana components of an Andreev bound state have  $\eta \simeq 1$ . Since in our case  $\lambda_1$  and  $\lambda_2$  are interchangeable, we can see that the values chosen are in the nonlocal regime, that is,  $\eta < 1$ . In Figs. 2a,b,e,f, we consider the case of  $\alpha = 0$  and coupling to a single Majorana mode, namely to  $\gamma_1$ . In this case, we can observe that the spectrum is symmetric as  $E(\Phi) = E(-\Phi)$  and the Majorana modes remain at zero energy [see panels (a) and (b)] as long as there is no

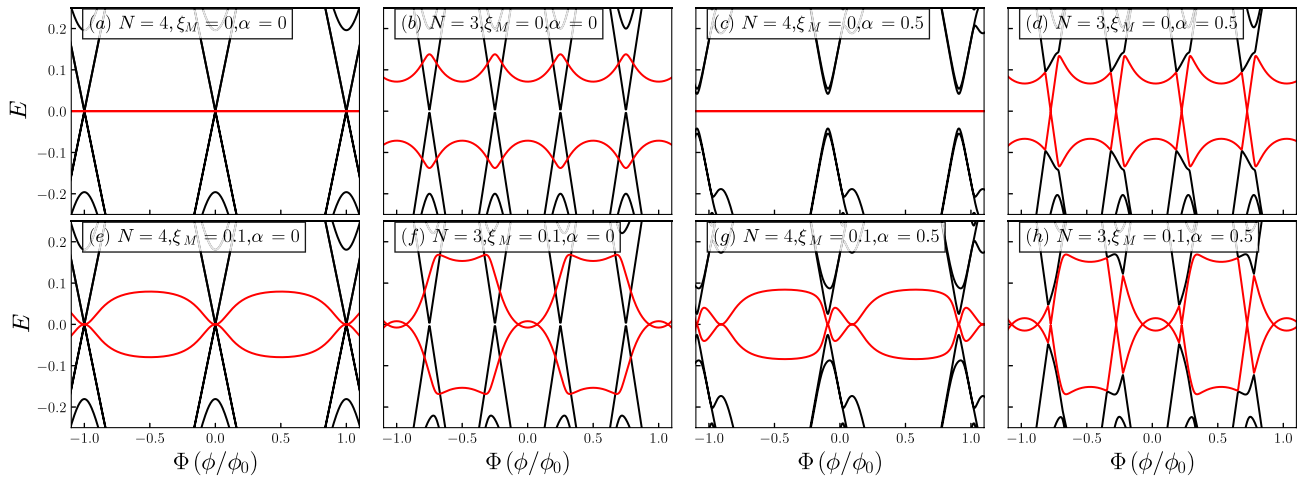


**Figure 3.** Quasiparticle spectra for  $\lambda_1 = 0.1$  and  $\lambda_2 = 0.15$ . The number of sites,  $N$ , the coupling between MZMs,  $\xi_M$ , and the Rashba spin-orbit coupling,  $\alpha$ , are indicated in the figure. Black curves represent the states in the quantum ring and the red curves correspond to the Majorana modes.

coupling between them, that is, as long as  $\xi_M = 0$ . However, the coupling to  $\gamma_1$  breaks the double degeneracy that would otherwise be present in the Dirac cone-like features of the spectra, as can be observed at zero flux. Notice that the degeneracy is lifted only for the spin-up bands, as can be understood from the coupling of the MZMs to the quantum ring in Eq. (8). Nevertheless, this coupling does not lift extra degeneracies, as we shall show when adding Rashba spin-orbit coupling. Once the coupling between MZMs is introduced [see panels (e) and (f)], we see the Majorana oscillations that naturally arise in finite-sized nanowires<sup>2</sup>. There are high symmetry points of the spectrum, namely at the Dirac points, where the hybridization between MZMs effectively vanishes. In panels (c), (d), (g) and (h), while the ring is still coupled to a single MZM, we introduce Rashba spin-orbit coupling. It can be observed that the effect corresponds to a lateral shift of the bands, as expected when Rashba spin-orbit interaction is present. It can be noticed, as we anticipated above, that only certain degeneracies are lifted by the coupling to the Majorana mode. Indeed, for  $N = 4$  we can see that the band that shifts to the left-hand side displays both gapless and gaped Dirac-like spectra close to zero energy, while the band that moves rightwards only shows a Dirac cone-like feature. However, for  $N = 3$  we can see that the two shifted sides present a gaped Dirac-like spectra; this is because the Rashba spin-orbit coupling makes possible the interaction between MZMs and spin down. This shift is also observed in the oscillatory behavior of the MZMs as they are coupled together. However, these shifts follow the Dirac points corresponding to the spin-up states to which  $\gamma_1$  is coupled, as we can observe in panels (g) and (h).

In Fig. 3a,b,e,f, we consider the effect of coupling between the two MZMs while keeping the Rashba spin-orbit coupling turned off,  $\alpha = 0$ . As we can observe, the degeneracy is further lifted by coupling the ring to the two MZMs, as can be observed at zero flux. However, as we expressed above, it is not entirely lifted since there are still gapless Dirac-like features at low energy. It is interesting to notice that there is a clear distinction between even- and odd-numbered rings. Indeed, even when the MZMs are explicitly uncoupled in the Hamiltonian, when  $\xi_M = 0$ , there is hybridization due to their coupling through the ring. Although we do not show it here, this behavior can be seen to occur in rings with a larger number of sites. This effect may be due to the fact that even-numbered rings with  $\alpha = 0$  and at zero flux present particle-hole symmetry  $c_{n,\sigma} \rightarrow (-1)^n c_{n,-\sigma}^\dagger$  and  $c_{n,\sigma}^\dagger \rightarrow (-1)^n c_{n,-\sigma}$ , whereas odd-numbered rings do not, making these two systems inherently different. Notice that this particle-hole symmetry is a true symmetry, whereas the particle-hole symmetry of the BdG Hamiltonian is a redundancy. Finally, in panels (c), (d), (g) and (h), we show the effect of including Rashba spin-orbit coupling, which breaks the symmetry  $E(\Phi) = E(-\Phi)$  by shifting sideways the bands, as occurred in panels (c), (d), (g) and (h) of Fig. 2. However, in contrast to the latter, the coupling to  $\gamma_2$  leads to a further reduction of the degeneracies in the problem. In fact, for  $N = 4$ , the spectrum is wholly gaped out, even for  $\xi_M = 0$ . There is then a clear distinction with the corresponding spectrum without Rashba spin-orbit coupling, which will affect the persistent currents, as we shall show below.

### Charge and spin persistent currents

Persistent currents have been studied extensively, both theoretically<sup>16,20–25</sup> and experimentally<sup>26–29</sup>. They constitute a peculiar quantum phenomenon resulting from the time-reversal symmetry breaking that occurs from coupling electrons to a gauge field, as in the Aharonov-Bohm effect.

In this section, we will study the appearance of persistent charge,  $I_q$ , and spin currents,  $I_s$ , in all the scenarios discussed above. We will calculate  $I_q$  as

$$I_q = -i \langle [N_\uparrow + N_\downarrow, H_r] \rangle, \tag{24}$$

and  $I_s$  as

$$I_s = -i \langle [N_\uparrow - N_\downarrow, H_r] \rangle, \tag{25}$$

where  $N_\sigma = \sum_n c_{n,\sigma}^\dagger c_{n,\sigma}$ . Notice that the charge persistent current can also be obtained from the eigenenergies  $E_\nu$  by summing over all states  $I_q = \sum_\nu I_{q,\nu}$  where<sup>16</sup>

$$I_{q,\nu} = -\frac{\partial}{\partial \Phi} [f(E_\nu) E_\nu], \tag{26}$$

and  $f(E_\nu)$  the Fermi distribution function. The total persistent current is obtained by summing over all states<sup>16</sup>. After lengthy but straightforward calculations, we find that

$$I_{q(s)} = - \sum_n \left[ \chi_n^{q(s)} + \gamma_n^{q(s)} - \chi_n^{q(s)} \langle d_{n,-} d_{n,-}^\dagger \rangle - \gamma_n^{q(s)} \langle d_{n,+} d_{n,+}^\dagger \rangle - 2\text{Re} \left\{ \beta_n^{q(s)} \langle d_{n,+} d_{n,-}^\dagger \rangle \right\} \right]. \tag{27}$$

As we can see, the expressions for the persistent currents are identical, except for the coefficients. For the charge persistent current, we find

$$\begin{aligned} \chi_n^q &= A_n^+ |\psi_-^u|^2 + A_n^- |\psi_+^u|^2 + 2\text{Re} \{ B_n \psi_-^u (\psi_+^u)^* \}, \\ \gamma_n^q &= A_n^+ |\psi_-^d|^2 + A_n^- |\psi_+^d|^2 + 2\text{Re} \{ B_n \psi_-^d (\psi_+^d)^* \}, \\ \beta_n^q &= A_n^+ \psi_-^u (\psi_+^d)^* + A_n^- \psi_+^u (\psi_-^d)^* + B_n \psi_-^u (\psi_+^d)^* + B_n^* \psi_+^u (\psi_-^d)^*, \end{aligned} \tag{28}$$

where

$$\begin{aligned} A_n^\pm &= \left[ \sin \left( \frac{\pi}{N} + \frac{2\pi}{N} \Phi + \frac{2\pi n}{N} \right) \pm 2\tilde{\alpha} \cos \left( \frac{\pi}{N} + \frac{2\pi}{N} \Phi + \frac{2\pi n}{N} \right) \right] \cos \left( \frac{\pi}{N} \right), \\ B_n &= (1 + i2\tilde{\alpha}) \cos \left( \frac{\pi}{N} + \frac{2\pi}{N} \Phi + \frac{2\pi n}{N} \right) \sin \left( \frac{\pi}{N} \right). \end{aligned} \tag{29}$$

The expressions for the spin persistent current coefficients are identical by replacing  $\sin \leftrightarrow \cos$  in  $A_n^\pm$  and  $B_n$  and by taking  $\tilde{\alpha} \rightarrow -\tilde{\alpha}$  in  $B_n$ . Considering the fluctuation-dissipation theorem, we can write

$$I_{q(s)} = - \sum_n \frac{1}{\pi} \int_{-\infty}^{\infty} d\omega f(\omega) \left[ \chi_n^{q(s)} \text{Im} \langle \langle d_{n,-}; d_{n,-}^\dagger \rangle \rangle_\omega + 2\text{Re} \left\{ \beta_n^{q(s)} \text{Im} \langle \langle d_{n,-}; d_{n,+}^\dagger \rangle \rangle_\omega \right\} + \gamma_n^{q(s)} \text{Im} \langle \langle d_{n,+}; d_{n,+}^\dagger \rangle \rangle_\omega \right]. \tag{30}$$

Here  $\langle \langle \cdot; \cdot \rangle \rangle$  stands for the Green's functions of the ring. Notice that we have dropped the first two terms in Eq. (27),  $\chi_n^{q(s)}$  and  $\gamma_n^{q(s)}$ , since they end up cancelling out. The Green's functions can be obtained by applying the equation of motion technique<sup>30</sup>, which are found to be

$$\begin{aligned} \langle \langle d_{n,-}; d_{n,-}^\dagger \rangle \rangle &= g_{p,-} + \frac{g_{p,-}^2 |\beta_{n,-}|^2}{\tilde{M}_p \tilde{M}_h - \tilde{S}^2} [\lambda_-^2 \tilde{M}_p + \lambda_+^2 \tilde{M}_h + 2\lambda_+ \lambda_- \tilde{S}] \\ \langle \langle d_{n,+}; d_{n,+}^\dagger \rangle \rangle &= g_{p,+} + \frac{g_{p,+}^2 |\beta_{n,+}|^2}{\tilde{M}_p \tilde{M}_h - \tilde{S}^2} [\lambda_-^2 \tilde{M}_p + \lambda_+^2 \tilde{M}_h + 2\lambda_+ \lambda_- \tilde{S}], \\ \langle \langle d_{n,-}; d_{n,+}^\dagger \rangle \rangle &= \frac{g_{p,-} \beta_{n,-} g_{p,+} \beta_{n,+}^*}{\tilde{M}_p \tilde{M}_h - \tilde{S}^2} [\lambda_-^2 \tilde{M}_p + \lambda_+^2 \tilde{M}_h + 2\lambda_+ \lambda_- \tilde{S}], \end{aligned} \tag{31}$$

where  $g_{p,\pm} = (z - \varepsilon_{n,\pm})^{-1}$  are the Green's functions of the quantum ring in the absence of interaction with the MZMs and

$$\begin{aligned} \tilde{M}_p &= z - \xi_M - \sum_n (\lambda_-^2 S_h + \lambda_+^2 S_p), \\ \tilde{M}_h &= z + \xi_M - \sum_n (\lambda_+^2 S_h + \lambda_-^2 S_p), \\ \tilde{S} &= \lambda_+ \lambda_- \sum_n \left( |\beta_{n,-}|^2 g_{h,-} + |\beta_{n,+}|^2 g_{h,+} + |\beta_{n,-}|^2 g_{p,-} + |\beta_{n,+}|^2 g_{p,+} \right). \end{aligned} \tag{32}$$

Here  $g_{h,\pm} = (z + \varepsilon_{n,\pm})^{-1}$  are the Green's functions for holes of the ring uncoupled to the MZMs. In order to assess the effect of having MZMs, we first show in Fig. 4 the charge and spin persistent currents for the system without MZMs. Additionally, we include the quasiparticle spectra where it can be seen that, as expected, the only effect is a lateral shift, as indicated by solid and dashed lines. Here, panels (b) and (c) correspond to the charge persistent currents for the  $N = 3$  and  $N = 4$  cases respectively and panels (d) and (e) correspond to the spin persistent currents for the  $N = 3$  and  $N = 4$  cases respectively. The different colours indicate the value of the Rashba spin-orbit interaction. As it can be noticed, the Rashba interaction leads to a secondary peak in the charge persistent current and to nonzero spin persistent currents.

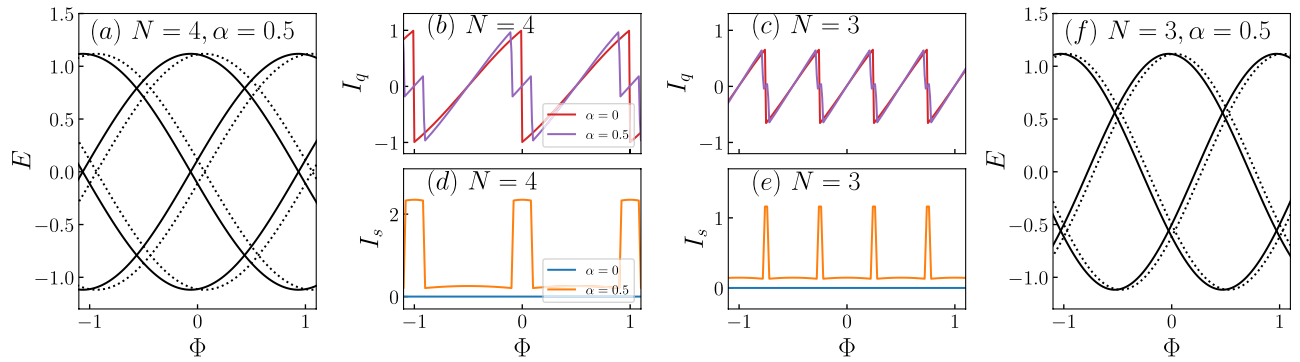


**Figure 4.** Quasiparticle spectra and corresponding charge and spin persistent currents,  $I_q$  and  $I_s$  respectively, for  $\lambda_1 = \lambda_2 = \xi_M = 0$ . The number of sites,  $N$ , and the Rashba spin-orbit coupling,  $\alpha$ , are indicated in the figures.

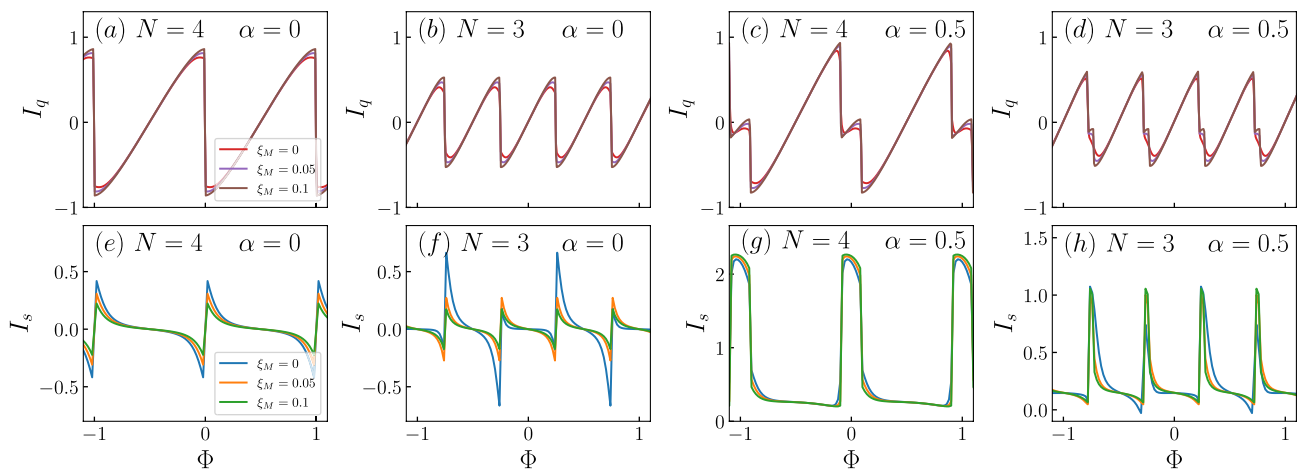


**Figure 5.** Charge and spin persistent currents,  $I_q$  and  $I_s$  respectively, for  $\lambda_1 = 0.1, \lambda_2 = 0$ . The number of sites,  $N$ , and the Rashba spin-orbit coupling,  $\alpha$ , are indicated in the figures. The coupling between MZMs,  $\xi_M$ , is indicated by coloured lines, shown in the leftmost panels.

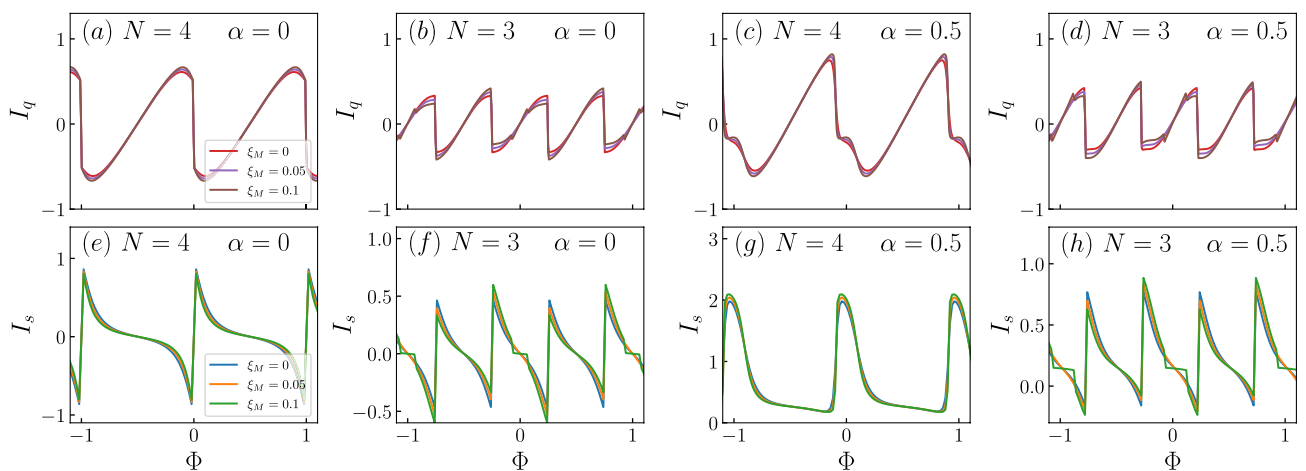


**Figure 6.** Charge and spin persistent currents,  $I_q$  and  $I_s$  respectively, for  $\lambda_1 = 0.1, \lambda_2 = 0.15$ . The number of sites,  $N$ , and the Rashba spin-orbit coupling,  $\alpha$ , are indicated in the figures. The coupling between MZMs,  $\xi_M$ , is indicated by coloured lines, shown in the leftmost panels.

We now study the persistent currents for the cases discussed in Figs. 2, 3 and obtain Figs. 5, 6. Here we use the same labeling as in the last figure, but the colours indicate three different values of  $\xi_M$ , one being  $\xi_M = 0$  [panels (a)–(d) in the BdG spectra], another being  $\xi_M = 0.1$  [panels (e)–(h) in the BdG spectra] and another one in between,  $\xi_M = 0.05$ , whose spectrum is not shown.

Figure 5a,b,e,f corresponds to the settings of Fig. 2a,b,e,f. The first thing we observe is that the persistent currents display the periodicity observed in the spectra, as it should. In the case of the charge currents, we can see that upon decreasing the interaction between the two MZMs, the peaks in the current become smoother. On the other hand, the spin currents are nonzero due to the coupling of one of the two MZMs to the up-spin electrons in the ring. However, as the coupling between MZMs increases, reducing their topological robustness, the spin current tends towards zero. This is consistent with the results shown in the Fig. 4 as a greater interaction hybridizes the Majoranas.

Figure 5c,d,g,h refers to the scenario considered in Fig. 2c,d,g,h, which is identical to the previous one except for a nonzero Rashba spin-orbit coupling. As we can see, in this case, the charge current is affected, as signaled by the appearance of additional peaks. Since the position of these peaks depends on the value of  $\alpha$ , we can fine-tune the persistent current by manipulating this parameter. However, the sharpest distinction occurs when considering the spin currents. As we can observe, Rashba renders the spin currents asymmetric around zero current and, additionally, it leads to a pulse-like pattern, similar to the one we can see in Fig. 4.

In Fig. 6a,b,e,f we show the persistent currents for the parameters of Fig. 3a,b,e,f. In this case, the Rashba spin-orbit coupling is turned off, but the two MZMs are coupled to the ring. As we can observe, the results for the charge current are not dramatically altered, except for the curves being smoother in the  $N = 4$  case and for a secondary peak at  $N = 3$  as  $\xi_M$  is increased to  $\xi_M = 0.1$ . These peaks feature in a clearer fashion in the spin currents, where a small plateau for  $\xi_M = 0.1$  is observed at certain values of flux. This can be understood from Fig. 3. Take for instance the spectrum around  $\Phi = 0$  in panel (f) of that figure. Although it is very subtle, there is a switching of the Majorana states at zero energy and it is in the region between the two crossings where this plateau takes place. Additionally, we can observe that there is no suppression of the spin current upon increasing  $\xi_M$ , as there was when  $\lambda_2 = 0$ . Therefore, we can see that, by coupling the ring to the two MZMs we are able to suppress spin current for a range of fluxes. This could be a smoking gun in the detection of MZMs as this situation is completely different from the result in the absence of MZMs (cf. Fig. 4).

Finally, Fig. 6c,d,g,h corresponds to the case shown in Fig. 3c,d,g,h. In this scenario, the currents are similar to those of panels (a), (b), (e) and (f), but with the additional peak that was observed for  $N = 4$  in Fig. 5c, although clearly smoothed out. In fact, the additional peak for the  $N = 3$  case is completely suppressed. This has an effect on the spin current, where the  $N = 4$  case still shows a pulse-like behaviour, but the  $N = 3$  case shows plateaus for a larger range of fluxes than in panels (a), (b), (e) and (f).

## Conclusions

MZMs stand out for their remarkable properties in the realm of topological quantum matter, such as their non-Abelian statistics. However, although significant progress has been made in the direction of their experimental detection in recent years, they cannot be confirmed as yet. More importantly, recent discoveries show that it is necessary to carefully examine different effects to determine their existence<sup>31</sup> unambiguously. In this regard, we propose to consider a topological superconducting nanowire in proximity to a quantum ring threaded by a magnetic flux. It is the natural extension of the system presented in Ref.<sup>17</sup> where a nanowire is coupled to a single quantum dot. In addition, we propose the ring to display Rashba spin-orbit coupling. As we have shown in this paper, the BdG spectra are entirely altered by coupling the quantum ring to one or two MZMs and having a nonzero Rashba spin-orbit coupling. The consequences are clearly observed in the persistent currents. Interestingly, spin-orbit coupling leads to an asymmetric spin current with a square pulse-like behavior. Moreover, the coupling to the two MZMs leads to plateaus for odd-numbered rings due to the switching of MZMs at zero energy. We believe that our work could serve as an additional signature towards probing the existence of Majorana zero modes.

Received: 21 July 2021; Accepted: 3 January 2022

Published online: 20 January 2022

## References

1. Beenakker, C. Search for Majorana fermions in superconductors. *Annu. Rev. Cond. Matter Phys.* **4**, 113–136 (2013).
2. Aguado, R. Majorana quasiparticles in condensed matter. *La Riv. Nuovo Cimento* **40**, 523–593 (2017).
3. Stanescu, T. D. & Tewari, S. Majorana fermions in semiconductor nanowires: Fundamentals, modeling, and experiment. *J. Phys. Cond. Matter* **25**, 233201 (2013).
4. Lutchyn, R. M. *et al.* Majorana zero modes in superconductor-semiconductor heterostructures. *Nat. Rev. Mater.* **3**, 52 (2018).
5. Sarma, S. D., Freedman, M. & Nayak, C. Majorana zero modes and topological quantum computation. *NPJ Quant. Inf.* **1**, 15001 (2015).
6. Sato, M. & Fujimoto, S. Majorana fermions and topology in superconductors. *J. Phys. Soc. Jpn.* **85**, 072001 (2016).
7. Kitaev, A. Y. Unpaired Majorana fermions in quantum wires. *Phys. Uspekhi* **44**, 131 (2001).
8. Alicea, J. New directions in the pursuit of Majorana fermions in solid state systems. *Rep. Prog. Phys.* **75**, 076501 (2012).
9. Elliott, S. R. & Franz, M. Colloquium: Majorana fermions in nuclear, particle, and solid-state physics. *Rev. Mod. Phys.* **87**, 137 (2015).
10. Lutchyn, R. M., Sau, J. D. & Das Sarma, S. Majorana fermions and a topological phase transition in semiconductor-superconductor heterostructures. *Phys. Rev. Lett.* **105**, 077001 (2010).
11. Oreg, Y., Refael, G. & von Oppen, F. Helical liquids and Majorana bound states in quantum wires. *Phys. Rev. Lett.* **105**, 177002 (2010).
12. Deng, M. T. *et al.* Majorana bound state in a coupled quantum-dot hybrid-nanowire system. *Science* **354**, 1557 (2016).

13. Deng, M.-T. *et al.* Nonlocality of Majorana modes in hybrid nanowires. *Phys. Rev. B* **98**, 085125 (2018).
14. Liu, X., Borunda, M. F., Liu, X.-J. & Sinova, J. Control of Josephson current by Aharonov-Casher phase in a Rashba ring. *Phys. Rev. B* **80**, 174524 (2009).
15. Maiti, S. K., Dey, M., Sil, S., Chakrabarti, A. & Karmakar, S. N. Magneto-transport in a mesoscopic ring with Rashba and Dresselhaus spin-orbit interactions. *EPL Europhys. Lett.* **95**, 57008 (2011).
16. Monisha, P. J., Sankar, I. V., Sil, S. & Chatterjee, A. Persistent current in a correlated quantum ring with electron-phonon interaction in the presence of Rashba interaction and Aharonov–Bohm flux. *Sci. Rep.* **6**, 20056 (2016).
17. Prada, E., Aguado, R. & San-Jose, P. Measuring Majorana nonlocality and spin structure with a quantum dot. *Phys. Rev. B* **96**, 085418 (2017).
18. Zeng, Q.-B., Chen, S., You, L. & Lü, R. Transport through a quantum dot coupled to two Majorana bound states. *Front. Phys.* **12**, 127302 (2017).
19. Ramos-Andrade, J. P., Orellana, P. A. & Ulloa, S. E. Detecting coupling of Majorana bound states with an Aharonov–Bohm interferometer. *J. Phys. Cond. Matter* **30**, 045301 (2018).
20. Byers, N. & Yang, C. N. Theoretical considerations concerning quantized magnetic flux in superconducting cylinders. *Phys. Rev. Lett.* **7**, 46 (1961).
21. Büttiker, M., Imry, Y. & Landauer, R. Josephson behavior in small normal one-dimensional rings. *Phys. Lett. A* **96**, 365 (1983).
22. Ambegaokar, V. & Eckern, U. Coherence and persistent currents in mesoscopic rings. *Phys. Rev. Lett.* **65**, 381 (1990).
23. Riedel, E. K. & von Oppen, F. Mesoscopic persistent current in small rings. *Phys. Rev. B* **47**, 15449 (1993).
24. Orellana, P. A. & Pacheco, M. Persistent current magnification in a double quantum-ring system. *Phys. Rev. B* **71**, 235330 (2005).
25. Maiti, S. K. & Chakrabarti, A. Magnetic response of interacting electrons in a fractal network: A mean-field approach. *Phys. Rev. B* **82**, 184201 (2010).
26. Mailly, D., Chapelier, C. & Benoit, A. Experimental observation of persistent currents in GaAs-AlGaAs single loop. *Phys. Rev. Lett.* **70**, 2020 (1993).
27. Jariwala, E. M. Q., Mohanty, P., Ketchen, M. B. & Webb, R. A. Diamagnetic persistent current in diffusive normal-metal rings. *Phys. Rev. Lett.* **86**, 1594 (2001).
28. Bluhm, H., Koshnick, N. C., Bert, J. A., Huber, M. E. & Moler, K. A. Persistent currents in normal metal rings. *Phys. Rev. Lett.* **102**, 136802 (2009).
29. Bleszynski-Jayich, A. C. *et al.* Persistent currents in normal metal rings. *Science* **326**, 272 (2009).
30. Jishi, R. A. *Feynman Diagram Techniques in Condensed Matter Physics* (Cambridge University Press, 2013).
31. Frolov, S. Quantum computing's reproducibility crisis: Majorana fermions. *Nature* **592**, 350 (2021).

## Acknowledgements

F.G.M. is grateful for the funding of scholarship CONICYT-Chile No. 21170550. L.R. and P.A.O. acknowledges support from FONDECYT, Grants 1180914 and 1201876. Work at Madrid has been supported by Agencia Estatal de Investigación, Grant PID2019-106820RB-C21.

## Author contributions

P.A.O., F.D.A. and L.R. conceived the research. F.G.M. and D.M. performed the calculations. A.D.F. carried out calculations and wrote the manuscript. All authors discussed the results and reviewed the manuscript.

## Competing interests

The authors declare no competing interests.

## Additional information

**Supplementary Information** The online version contains supplementary material available at <https://doi.org/10.1038/s41598-022-05043-y>.

**Correspondence** and requests for materials should be addressed to F.G.M.

**Reprints and permissions information** is available at [www.nature.com/reprints](http://www.nature.com/reprints).

**Publisher's note** Springer Nature remains neutral with regard to jurisdictional claims in published maps and institutional affiliations.



**Open Access** This article is licensed under a Creative Commons Attribution 4.0 International License, which permits use, sharing, adaptation, distribution and reproduction in any medium or format, as long as you give appropriate credit to the original author(s) and the source, provide a link to the Creative Commons licence, and indicate if changes were made. The images or other third party material in this article are included in the article's Creative Commons licence, unless indicated otherwise in a credit line to the material. If material is not included in the article's Creative Commons licence and your intended use is not permitted by statutory regulation or exceeds the permitted use, you will need to obtain permission directly from the copyright holder. To view a copy of this licence, visit <http://creativecommons.org/licenses/by/4.0/>.

© The Author(s) 2022

# 4

## Two-terminal Josephson Junctions with Topological Superconductors.

Two topological superconductors attached to a quantum ring composed of a finite number of sites is a system that may be simple at first look but with rich physics. The two superconductors relatively close with each other suffer an effect common in all superconductors, known as the Josephson effect (cooper pairs tunnel from one superconductor to another). Not only Josephson effect is present in this kind of junction also we can find topological states of matter that go beyond the ten-fold topological classification. Across this chapter, the fundamentals are shown to understand the work found at the end of the chapter.

### 4.1 Symmetries.

From the Wigner theorem, any symmetry transformation in quantum mechanics can be represented on the Hilbert space by an operator that is either linear and unitary, or antilinear and antiunitary. Hence, a system is invariant under a unitary transformation if the canonical anticommutator and  $H$  are preserved,  $\{\psi_a, \psi_b^\dagger\} = U \{\psi_a, \psi_b^\dagger\} U^{-1}$  and  $UHU^{-1} = H$ . Where  $\psi_a$  is a fermionic operator in the respective lattice site and spin states  $a$ .

The unitary symmetry operation is called spatial and nonspatial when it acts or does not act on the spatial part. In particular, when  $U$  can be factorized as  $U = \prod_i U_i$ . Namely, when it acts on each lattice site separately, it is nonspatial and is called on-site. For antiunitary symmetry operations, the definition holds. The time-reversal operator is an example of a nonspatial operator. What follows summarizes the three symmetries that form the building blocks for the ten-fold way classification.

#### 4.1.1 Time-reversal Symmetry.

The time-reversal operator  $T$  is antiunitary (antilinear and unitary) and acts on fermion creation and annihilation operators as:

$$T\psi_a T^{-1} = (U_T)_a^b \psi_b, \quad TiT^{-1} = -i. \quad (4.1)$$

A system is time-reversal invariant if  $T$  preserves the canonical anticommutator and if the Hamiltonian satisfies  $THT_{-1} = H$ . In non-interacting systems, the above condition leads to

$$T : U_T^\dagger H^* U_T = +H \quad (4.2)$$

The symmetry class is an entire family of Hamiltonians that share generic symmetries. Therefore, we can let  $H$  run over all possible single-particle Hamiltonians of such symmetry class with time-reversal symmetry. Applying the time-reversal operator twice, we get  $(U_T^* U_T)^\dagger H (U_T^* U_T) = H$ . Since  $H$  runs overall reducible representations space,  $U_T^* U_T$  should be a multiple of identity matrix  $\mathbb{1}$ . Then,  $U_T^* U_T = e^{i\alpha} \mathbb{1}$  and in consequence  $U_T^* = e^{i\alpha} U_T^\dagger$ . Therefore,  $e^{i2\alpha} = 1$ , which leads to the two possibilities  $U_T^* U_T = \pm \mathbb{1}$ . Hence, when applying time-reversal over a fermion operator, the same operator is obtained up to a sign. For a many-body fermionic operator,  $TOT^{-2} = (\pm)^n O$ . The action of  $\hat{T}$  operator can be summarized as:

$$T^2 = (\pm)^N, \quad (4.3)$$

where,  $\hat{N} = \sum_a \psi_a \psi_a$  in particular when  $U_T^* U_T = -\mathbb{1}$ ,  $\hat{T}$  squares to the fermion number parity. For a system with  $\hat{T}^2 = -1$  (odd number of fermions), Time-reversal invariance leads to the Kramers degeneracy of the eigenvalues.

### 4.1.2 Particle-Hole Symmetry.

Particle-hole is a unitary transformation that mixes fermion creation and annihilation operators. It is also called charge-conjugation, since particle number conserving systems flip the sign of the  $U(1)$  charge. In other words, if we apply the charge conjugation operator over a fermionic state, this reads:

$$C\psi_a C^{-1} = (U_C^*)_a^b \psi_b^\dagger \quad (4.4)$$

Therefore, some systems possess a natural charge conjugation symmetry like a phonon, but certainly, a free fermion does not have such symmetry. Even though, We can apply the constraint or the condition to a fermionic state or a set of fermionic states, as was done for a free electron model in Eq. (2.11) in that case, the  $H_{BdG}$  is symmetric under particle-hole transformation. By representing the same arguments that in the case of time-reversal, we notice that there are two kinds of particle-hole symmetry:

$$C^2 = (\pm 1)^N \quad U_C^* U_C = \pm \mathbb{1} \quad (4.5)$$

when,  $CHC^{-1} = H$ , the particle-hole reserved partner  $C|a\rangle$  of every eigenstate  $|a\rangle$  of  $H$  is also an eigenstate, since  $CHC^{-1}C|a\rangle = E_a C|a\rangle$ . Similarly, for single particle Hamiltonians, it follows that for every eigenfunction  $u^A$  of  $H$  with eigenenergy  $\varepsilon^A$ ,  $H^{ab}u_b^A = \varepsilon^A u_a^A$ , its particle-hole reversed partner  $U_C^\dagger (u^A)^*$  is also an eigenfunction, but with energy  $-\varepsilon^A$ .

### 4.1.3 Chiral Symmetry.

Chiral symmetry is given by the combination of the above two symmetries. One can have a situation where time-reversal and particle-hole are broken, but chiral symmetry is satisfied. Hence, we have:

$$\Gamma = T \cdot C. \quad (4.6)$$

Chiral symmetry acts on fermion operators as

$$\Gamma \psi_a \Gamma^{-1} = (U_C U_T)_a^b \psi_b^\dagger. \quad (4.7)$$

The invariance of a quadratic Hamiltonian under chiral symmetry is described by:

$$\hat{T} : U_\Gamma^\dagger H U_\Gamma = -H, \quad U_\Gamma = U_C^* U_T^*. \quad (4.8)$$

Since,  $T^2 = C^2 = (\pm)^N$ , it is easy to see that  $\Gamma^2 = 1$ . The chiral symmetry gives rise to a symmetric spectrum of single-particle Hamiltonians: if  $|u\rangle$  is an eigenstate of  $H$  with eigenvalue  $\varepsilon$ , then  $U_\Gamma |u\rangle$  is also an eigenstate, but with eigenvalue  $-\varepsilon$ . In the basis in which  $U_\Gamma$  is diagonal, the single-particle Hamiltonian  $H$  is block-off-diagonal,

$$H = \begin{pmatrix} 0 & h \\ h^\dagger & 0 \end{pmatrix} \quad (4.9)$$

where  $h$  is a rectangular matrix. As an example of such a Hamiltonian, we can find the spinless fermions on a bipartite lattice. Also, the Hamiltonian that we considered in this work is a spinless quantum ring side coupled to a spinless chain. It is observed when the Hamiltonian is written in Majorana representation and expressed in BdG form.

### 4.1.4 Properties of a System with Chiral Symmetry.

A Hamiltonian with chiral symmetry obeys the follow:

$$\{H, \Gamma\} = 0, \quad \Gamma^2 = 1. \quad (4.10)$$

The Hamiltonian  $H$  is in a BdG form and obeys the eigenvalues' equation:

$$H |u_E\rangle = E |u_E\rangle. \quad (4.11)$$

Now, we would like to show that there is a one to one correspondence between (4.11) and the following equation:

$$H^2 |v_{E^2}\rangle = E^2 |v_{E^2}\rangle \quad (4.12)$$

For  $E^2 \neq 0$ , if  $(H + E) |v_{E^2}\rangle$ , the solution  $|u_E\rangle$  is:

$$|u_E\rangle = c (H + E) |v_{E^2}\rangle, \quad (4.13)$$

with  $c$  a normalization constant. Now, if  $(H + E) |v_{E^2}\rangle = 0$  the solution is:

$$|u_E\rangle = \Gamma |v_{E^2}\rangle, \quad (4.14)$$

For (4.12) and  $E^2 = 0$  we obtain

$$H^2 |v_0\rangle = 0. \quad (4.15)$$

The above equation implies that:

$$\langle v_0 | H^2 | v_0 \rangle = \| H | v_0 \rangle \|^2 = 0, \quad (4.16)$$

and in consequence we get

$$H | v_0 \rangle = 0. \quad (4.17)$$

The zero energy solution  $|u_0\rangle$  is obtained by  $|u_0\rangle = |v_0\rangle$ . Since, there exist a one to one correspondence between the solution (4.11) and (4.12). Since,  $H^2$  and  $\Gamma$  commute with each other, the eigenvalues of (4.12) are simultaneously eigenvalues of  $\Gamma$ . Then, for  $E^2 \neq 0$ , the solution  $|v_{E^2}^+\rangle$  satisfying  $\Gamma |v_{E^2}^+\rangle = |v_{E^2}^+\rangle$  is constructed from the solution  $|v_{E^2}^-\rangle$  satisfying  $\Gamma |v_{E^2}^-\rangle = -|v_{E^2}^-\rangle$  by multiplying  $H$  from the left

$$|v_{E^2}^+\rangle = c' H |v_{E^2}^-\rangle, \quad (4.18)$$

where  $c'$  is a normalization constant. Therefore, for  $E^2 \neq 0$ , the solution of (4.12) with chirality  $\Gamma = 1$  is always paired with the solution of chirality  $\Gamma = -1$ . Also, for  $E^2 = 0$ , the solutions are not paired. We can conclude two aspects for systems with chiral symmetry: *i*) States that are at zero energy are simultaneously eigenstates of the  $\Gamma$  operator, and *ii*) nonzero energy states can be described as a linear combination of two states associated with the eigenvalues of  $\Gamma$ .

# Josephson and Persistent Currents in a Quantum Ring between Topological Superconductors

Fabián Medina,\* Juan Pablo Ramos-Andrade, Luis Rosales, and Pedro Orellana

In this work, the spectra in an Aharonov–Bohm quantum-ring interferometer forming a Josephson junction between two topological superconductor (TSC) nanowires are investigated. The TSCs host Majorana bound states at their edges, and both the magnetic flux and the superconducting phase difference between the TSCs are used as control parameters. A tight-binding approach is used to model the quantum ring coupled to both TSCs, described by the Kitaev effective Hamiltonian. The problem is solved by means of exact numerical diagonalization of the Bogoliubov-de Gennes Hamiltonian and obtain the spectra for two sizes of the quantum ring as a function of the magnetic flux and the phase difference between the TSCs. Depending on the size of the quantum ring and the coupling, the spectra display several patterns. Those are denoted as line, point, and undulated nodes, together with flat bands, which are topologically protected. The first three patterns can be possibly detected by means of persistent and Josephson currents. Hence, the results could be useful to understand the spectra and their relation with the behavior of the current signals.

## 1. Introduction

Topological properties in matter have been intensively investigated in the past decade in different contexts, starting with gapped topological phases in insulators, superconductors (SCs)<sup>[1–3]</sup> and in gapless topological phases, such as Weyl semimetals.<sup>[4–6]</sup> The classification of these phases is summarized in the tenfold way, with time reversal ( $\mathcal{T}$ ), particle–hole ( $PH$ ), and chiral ( $C$ ) symmetries being the cornerstone of topological matter.<sup>[7–9]</sup> One widely studied system is the Kitaev chain that belongs to class D, since it is a system with broken  $\mathcal{T}$  and  $C$  symmetries, leaving the  $PH$  symmetry as the one that protects the edge modes in the Kitaev chain in its topological phase. These modes, also known as Majorana bound states (MBSs),<sup>[10–12]</sup> receive important attention in their detection, manipulation, and control with the objective of being implemented in quantum computing.<sup>[13–16]</sup> Originally, the idea of the Kitaev chain had

a complication, which relies on the fact that to possess the topological phase, the fermionic states must be spinless fermions. This complication has been overcome since spinless fermions can now be understood experimentally as fully polarized fermions, and under the effect of superconductivity and high Rashba spin-orbit interaction, spin-triplet superconductors are produced.<sup>[17,18]</sup>

Intrinsic spin-triplet SCs have been found in different materials, such as  $Li_2Pt_3B$  due to its broken inversion symmetry<sup>[19]</sup> and in quasi 1D chromium pnictide  $K_2Cr_3As_3$ .<sup>[20]</sup> But they have also been produced by artificially implementing spin-singlet SCs: in interfaces of SC-ferromagnet,<sup>[21]</sup> or by employing the most common setup for observing MBSs, which consists of taking Al-InAs or InSb nanowires and inducing superconductivity by the proximity effect.<sup>[22–24]</sup>

In this context, Josephson junction devices with spin-singlet pairing SCs overcome topological characteristics that go beyond the tenfold classification, displaying Weyl points in the parameter space.<sup>[25–28]</sup> The classification of these hybrid systems could be clarified following the work of Zhang et al.<sup>[29]</sup> In recent works, multiterminal Josephson junctions with spin-triplet pairing SCs hosting MBSs at the edges provide a twist in these reputed Weyl points. Since Weyl points in crystals require the breaking of  $\mathcal{T}$  or inversion symmetry, in four-terminal junctions, the Weyl and nodal points may also occur under  $\mathcal{T}$  symmetry.<sup>[30–32]</sup> The importance of the Josephson junctions lies in the engineering of Andreev bound states (ABSs) and their control by building topological quantum-computing architectures based on MBSs,<sup>[33–37]</sup> where superconducting phase difference, bias voltage, and magnetic flux play the role of control parameters.<sup>[38,39]</sup> To observe MBSs in 1D topological superconductors (TSCs), one of the most suggested models is based on quantum dots (QDs) because they are easily tunnelable objects. Certainly, there are proposals based on observing the half-integer conductance at zero bias,<sup>[40,41]</sup> or the nonlocality of MBSs in 1D hybrid nanowires,<sup>[42]</sup> which is an experimental observation. Some theoretical proposals are based on the structure of an Aharonov–Bohm quantum-ring, where it is suggested to observe the discontinuities in persistent currents to detect zero energy crossing or nodal behaviors<sup>[43,44]</sup> or in the persistence conductance, which also displays nodal behavior.<sup>[45]</sup>

F. Medina, J. P. Ramos-Andrade, L. Rosales, P. Orellana  
Departamento de Física  
Universidad Técnica Federico Santa María  
Casilla 110-V, Valparaíso, Chile  
E-mail: fabian.medinac@sansano.usm.cl

 The ORCID identification number(s) for the author(s) of this article can be found under <https://doi.org/10.1002/andp.202100305>

DOI: 10.1002/andp.202100305

**Table 1.** List of topological patterns for  $N = 3$  quantum-ring in a two-junction with 1D TSCs. The first column indicates the type of junction. The next columns represent the non-zero couplings marked with an  $\times$ . The latter column shows the topological pattern observed in the spectra or the presence of flat bands.

Junction	$\lambda_1$	$\lambda_2$	$\lambda'_1$	$\lambda'_2$	$\xi_1$	$\xi_2$	Nodes
A	$\times$		$\times$		0	0	Line
					$\times$	0	Flat band
					$\times$	$\times$	Line
					$\times$	$\times$	Line
B	$\times$	$\times$	$\times$		$\times$	0	Flat band
C	$\times$		$\times$	$\times$	$\times$	0	Line
D	$\times$	$\times$	$\times$	$\times$	0	$\times$	Flat band
					$\times$	$\times$	Undulate
					$\times$	0	Undulate
					0	$\times$	Line
					$\times$	$\times$	Undulate

In this work, we investigate a low-energy model that describes a bi-junction consisting of an Aharonov–Bohm quantum-ring between two 1D TSCs. The analysis of the system is made in 2D parameter space, composed of the phase difference between the TSCs and the magnetic flux. The ABS spectra are obtained from the exact numerical diagonalization of the BdG Hamiltonian, observing zero energy crossing or nodes, flat bands, and the coexistence of both. These three features are the topological characteristics of the spectra in a bijunction that involves four MBSs. Interestingly, some band structures obtained for semimetals<sup>[46,47]</sup> could be studied using the interplay in magnetic flux and phase differences of TSCs. In addition, we found that the persistent and DC Josephson currents can be used to detect those topological patterns. Both current signals are mixed in our system, and our results shows that they can be controlled by tuning the magnetic flux and/or the phase difference.

This work is organized as follows. In Section 2, we describe the model and the theoretical considerations that we take before diagonalization. In Section 3, we explain the coupling configurations from the MBSs with the quantum ring and present the spectra. In Section 4, we present persistent and DC Josephson currents and the interplay between them through the parameter space  $(\Phi, \theta/\pi)$ . Finally, in Section 5 we summarize the results which are stored in Tables 1 and 2.

## 2. Model and Procedure

### 2.1. Model

The theoretical setup is based on a bijunction consisting of a tight-binding model for a 1D spinless Aharonov–Bohm quantum ring with two D-class TSCs attached to the side, as it is schematically represented in Figure 1. The Hamiltonian for the two TSCs is chosen effectively such that it only captures the edge states. Hence, the Hamiltonian in the Majorana representation is written as

$$H_{\text{TSC}} = i\xi_1\eta_1\eta_2 + i\xi_2\eta_3\eta_4 \quad (1)$$

**Table 2.** Topological patterns for  $N = 4$  quantum-ring in a two-junction with 1D TSCs. The columns represent the same as Table 1 with a distinction in the second column from this table which represents the position of one TSC at sites  $j = 1, 2$  while the other remains fixed at  $j = 0$ .

Junction	$j$	$\lambda_1$	$\lambda_2$	$\lambda'_1$	$\lambda'_2$	$\xi_1$	$\xi_2$	Nodes
A	1	$\times$		$\times$		0	0	Rectangular
						0	$\times$	Line and flat band
						$\times$	0	Line and flat band
						$\times$	$\times$	Fourfold line
B	2					0	$\times$	Line
						$\times$	0	Line
						$\times$	$\times$	Fourfold line
						$\times$	$\times$	Fourfold line
B	1	$\times$	$\times$	$\times$	$\times$	0	0	Flat band
						$\times$	$\times$	Line
						$\times$	0	Line
						$\times$	$\times$	Line
C	1	$\times$		$\times$	$\times$	0	0	Point and flat band
						0	$\times$	Point and flat band
						$\times$	0	Point and flat band
						$\times$	$\times$	Point and line
D	2					$\times$	0	Point
						0	$\times$	Line
						$\times$	$\times$	Point and line
						$\times$	$\times$	Point and line
D	1	$\times$	$\times$	$\times$	$\times$	$\times$	0	Line
						0	$\times$	Line
						$\times$	$\times$	Line
						$\times$	0	Point
						$\times$	$\times$	Point and line

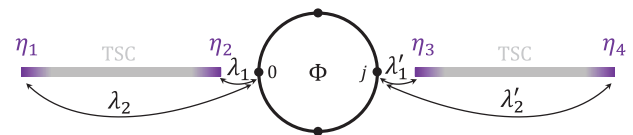


**Figure 1.** Schematic view of the system under study: Two TSCs (gray) hosting MBSs in their edges (purple) connected with a quantum-ring, crossed by a magnetic flux. The left TSC is coupled with the 0-site, while the other TSC is at site  $j$ . The couplings setup presented corresponds to Equation (6). Note that when  $\lambda_2 = \lambda'_2 = 0$  and  $\lambda_1(\lambda'_1) \rightarrow \lambda(\lambda')$  correspond to Equation (5).

with  $\xi_{1(2)} \approx e^{-L_{1(2)}}$  the coupling amplitude proportional to the correlation length between MBSs and  $L_{1(2)}$  the ratio between nanowire length and the superconducting coherence length. Note that we do not consider Majorana oscillations in each TSC. These oscillations appear when Majorana modes, belonging to the same TSC, interact with each other and have a dependence on either the Zeeman field or chemical potential.<sup>[48–51]</sup> The Hamiltonian for the quantum-ring in the position space is given by

$$H_R = \sum_{l=0}^{N-1} e^{i\frac{2\pi}{N}\Phi} t c_l^\dagger c_{l+1} + \text{h.c.} \quad (2)$$

with  $N$  the total number of states in the quantum-ring,  $\Phi$  the magnetic flux in units of  $\phi_0 = h/e$ , and  $t$  the hopping amplitudes

between QDs. A useful way to approach this Hamiltonian is to write it in the momentum space by choosing the transformation  $c_l = \sum_k e^{ikl} c_k$ . Then,  $H_R$  is expressed as

$$H_R = \sum_k 2t \cos \left( k + \frac{2\pi}{N} \Phi \right) c_k^\dagger c_k \quad (3)$$

where  $c_k^\dagger$  and  $c_k$  are the creation and annihilation operators for the states in the quantum-ring,  $k = 2\pi m/N$  with  $m = 0, 1, 2, \dots, N-1$ . In Majorana representation, the Hamiltonian is written as

$$H_R = i2t \sum_k \cos \left( k + \frac{2\pi}{N} \Phi \right) \alpha_k^{(1)} \alpha_k^{(2)} \quad (4)$$

with  $c_k = (\alpha_k^{(1)} + i\alpha_k^{(2)})/\sqrt{2}$  and  $c_k^\dagger = (\alpha_k^{(1)} - i\alpha_k^{(2)})/\sqrt{2}$ . The last Hamiltonian corresponds to the coupling between the fermionic states of the TSCs and the fermionic states in the quantum-ring with position  $l = 0$  and  $l = j$  being  $j = 1, 2, \dots, N-1$ . This Hamiltonian in real space reads

$$H_C = \lambda f^\dagger c_0 + \lambda' e^{i\frac{\theta}{2}} a^\dagger c_j + \text{h.c.} \quad (5)$$

Here,  $f^{(\dagger)}$  are the fermionic states of one TSC coupled to the site  $l = 0$  in the quantum-ring and  $a^{(\dagger)}$  represents the fermionic states of the TSC coupled to the site  $l = j$  with amplitudes  $\lambda$  and  $\lambda'$ , respectively, and with  $\theta$  as the superconducting phase difference. Therefore, a low energy coupling Hamiltonian can be obtained by introducing the transformation  $f^\dagger = (\mu\eta_1 - i\nu\eta_2)/\sqrt{2}$  and  $a^\dagger = (\delta\eta_3 - i\kappa\eta_4)/\sqrt{2}$ , with  $|\mu|^2 + |\nu|^2 = |\delta|^2 + |\kappa|^2 = 1$ . The parameters  $\mu$ ,  $\nu$ ,  $\delta$ , and  $\kappa$  are the weights of the quasiparticle excitations. As we are working in the momentum space, the transformation  $c_0 = \sum_k c_k$  and  $c_j = \sum_k e^{ikj} c_k$  must be taken into account

$$\begin{aligned} H_C = & i \sum_k \left[ \lambda_1 \eta_1 \alpha_k^{(2)} + \lambda_2 \alpha_k^{(1)} \eta_2 \right] \\ & + i\lambda'_1 \sum_k \left[ S_j(k, \theta) \alpha_k^{(1)} \eta_3 + C_j(k, \theta) \eta_3 \alpha_k^{(2)} \right] \\ & + i\lambda'_2 \sum_k \left[ C_j(k, \theta) \alpha_k^{(1)} \eta_4 + S_j(k, \theta) \eta_4 \alpha_k^{(2)} \right] \end{aligned} \quad (6)$$

where  $\lambda_1 = \mu\lambda$ ,  $\lambda_2 = \nu\lambda$ , and  $\lambda'_1 = \delta\lambda'$ ,  $\lambda'_2 = \kappa\lambda'$ . Note if  $\nu \rightarrow 0$  and  $\kappa \rightarrow 0$ , the Hamiltonian reduces to the case in which the two nanowires are infinite and a truly Majorana zero mode hybridizes with the quantum-ring. In the equation above  $S_j(k, \theta) = \sin(kj + \theta/2)$  and  $C_j(k, \theta) = \cos(kj + \theta/2)$ . Hence, the full Hamiltonian of the model is written as

$$H = H_R + H_{\text{TSC}} + H_C \quad (7)$$

Figure 1 displays a schematic representation of the system for  $H_C$  given by Equation (5) (Figure 1a) and Equation (6) (Figure 1b).

## 2.2. Bogoliubov-de Gennes

To obtain the energy spectra, we write the Hamiltonian in a BdG form, which implies writing it in a redundant manner. This pro-

cedure, apart from returning a skew-symmetric matrix in Majorana representation, imposes a constraint which is usually called particle-hole symmetry. Therefore, all the spectra obtained will be symmetric around zero energy. The basis chosen for the skew-symmetric matrix is

$$\Psi = \left( \alpha_0^{(1)} \alpha_1^{(1)} \dots \alpha_{N-1}^{(1)} \alpha_0^{(2)} \alpha_1^{(2)} \dots \alpha_{N-1}^{(2)} \eta_1 \eta_2 \eta_3 \eta_4 \right)^T \quad (8)$$

Hence, the Hamiltonian is written as

$$H = \Psi^\dagger H_{\text{BdG}} \Psi \quad (9)$$

The size of  $H_{\text{BdG}}$  depends on the number of states in the quantum ring. Here, we can identify the symmetry of the Hamiltonian by observing on which basis the Hamiltonian can be written as a linear combination of the generators of the symmetry group. For example, if we consider a single mode in the quantum-ring,  $H_{\text{BdG}}$  has a dimension of  $6 \times 6$  only if  $\xi_{1(2)} \neq 0$  and can be written as a linear combination of the imaginary elements of the  $SU(6)$  in the  $\lambda$ -representation. Thus, if we consider  $N$  the number of states in the quantum-ring, the symmetry of the Hamiltonian is  $SU(2N+4)$  in Majorana representation.<sup>[9]</sup> Therefore, the Hamiltonian can be written in compact form as

$$H_{\text{BdG}} = \frac{1}{2} \mathbf{h} \cdot \Lambda \quad (10)$$

with  $\mathbf{h}$  a vector with the dimension  $(2N+4)^2 - 1$ , which is nothing but the dimension of the  $SU(2N+4)$  Lie group and  $\Lambda$  are the elements of the Lie group.

## 2.3. Chiral Symmetry

We have imposed over the Hamiltonian a  $\mathcal{PH}$  constraint. Therefore, the eigenvalues of the  $H_{\text{BdG}}$  come in pairs. What remains is to determine at which points in the parameter space the system possesses  $C$  symmetry. Hence, if the Hamiltonian preserves  $C$  symmetry it must satisfy the following property

$$\Gamma H_{\text{BdG}} \Gamma^{-1} = -H_{\text{BdG}} \quad (11)$$

with  $\Gamma$  being a chiral operator written in a general form as

$$\Gamma = e^{-i\gamma \mathbf{n} \cdot \Lambda} \quad (12)$$

where,  $\gamma \mathbf{n}$  are  $(2N+4)^2 - 1$  arbitrary parameters. Hence, the rotation is made around the unit vector  $\mathbf{n}$ . Choosing  $\gamma = \pi$  and  $\mathbf{n} \cdot \mathbf{h} = 0$ , the operator satisfies Equation (11) and the anticommutation relation  $\{\Gamma, H_{\text{BdG}}\} = 0$ . As  $\Gamma^2 = 1$ , the eigenvalues of the operator are  $\Gamma = \pm 1$ . Following ref. [52], we know two things: i) The zero energy crossing states in a given BdG Hamiltonian are simultaneously eigenstates of the  $\Gamma$  operator; and ii) nonzero energy states are described by a linear combination of two states  $\psi_\pm$  precisely associated with the eigenvalues of  $\Gamma$ . Therefore, for an eigenstate outside zero energy  $\psi = c_+ \psi_+ + c_- \psi_-$  with  $|c_+| = |c_-|$ .

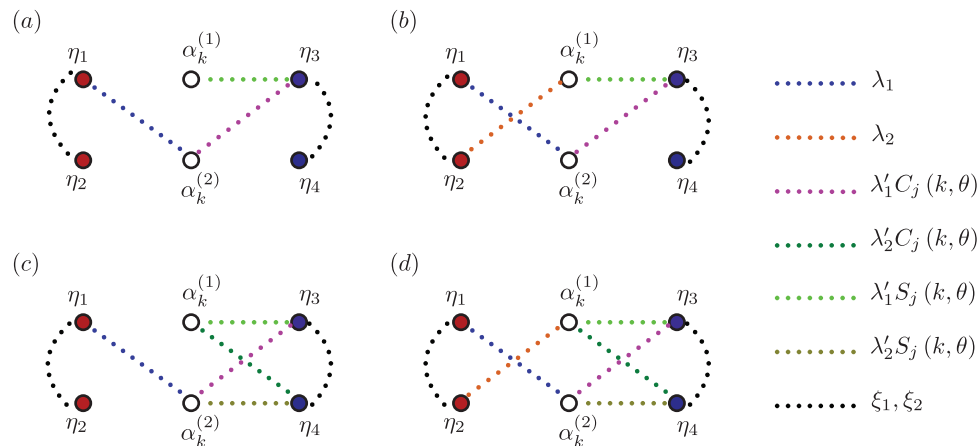


**Figure 2.** Schematic configurations of the four coupling configurations. a) A-junction: two MBSs are hybridized directly with the quantum-ring. b) B-junction: three MBSs hybridized directly. c) C-junction: three MBSs hybridized directly, where two of the MBSs belong to the TSC with phase  $\theta$ . d) D-junction: four MBSs hybridized directly with the quantum-ring. In all the junctions we have the possibility of indirect coupling between  $\eta_2$  and  $\eta_4$ , through  $\xi_{1(2)}$ . The asymmetry in the couplings is due to the presence of the phase difference  $\theta$ .

### 3. Junction Configurations and Spectra

#### 3.1. Junctions

Before proceeding with the spectra, we consider four types of junction configurations for which the minimum number of MBSs hybridizing the ring is two, and the maximum number is four. For the latter case, when  $\xi_{1(2)} = 0$ , we have a pretty similar configuration as that of ref. [31] emphasizing that we have a single phase difference. **Figure 2** shows the graphical representation for the four types of junctions considered. This is a graphical representation of the coupling Hamiltonian. Note that there is a coupling between MBSs with the same chirality, like  $\eta_3$  and  $\alpha_k^{(1)}$ . This is purely due to the effect of superconducting phase difference, and it can be checked by taking  $\theta = 0$  in Equation (6), returning to the symmetric coupling. In these four junctions, we consider two possibilities: a direct and an indirect hybridization of the MBSs. Such considerations give rise to effects in the delocalization of the MBSs.<sup>[42,43]</sup>

In addition to the phase difference, we have taken into account the position of the TSCs, since that starts to be important for  $N \geq 4$ . For  $N = 3$ , no matter what the TSCs positions are, the system is noncentrosymmetric, while in the case of  $N = 4$ , the system could be either: noncentrosymmetric or centrosymmetric, for  $j = 1$  and  $j = 2$ , respectively.

#### 3.2. Spectra

In this section, we are going to analyze the spectra for each of the junctions mentioned before. In what follows, the energy spectra are presented in units of twice the hopping between states in the quantum-ring, that is, in units of  $2t$ . We focus only on a system with  $N = 3$  and  $N = 4$  number of sites in the ring. With this restriction, we lost some generality, but not the utility of the results, since some Aharonov–Bohm quantum-rings architecture is based on InAs, for example, which could be used to prove the results.<sup>[53,54]</sup>

##### 3.2.1. Quantum-Ring with Three Quantum Dots

As mentioned before, we considered four types of junctions named: A-junction, B-junction, C-junction, and D-junction. In the A-junction, only two MBSs hybridize the system and their spectra can be observed in **Figure 3**. The spectra are displayed in the parameter space formed by the magnetic flux,  $\Phi$ , and the phase difference between both TSCs,  $\theta$ , in a noncentrosymmetric configuration with coupling parameters  $\lambda_2 = \lambda'_2 = \xi_1 = \xi_2 = 0$ . Note that for this case ( $N = 3$ ) only the noncentrosymmetric configuration is allowed. The panel (a) shows the inner gap bands formed by the hybridized MBSs, and from this we can see that bands have zero energy crossings. Panel (b) shows the projection of the lower band utilizing a color map. It is clear from the plots that linear node patterns are formed, having a periodicity of  $4\pi$  concerning the phase difference  $\theta$ . In addition, panel (c) shows the 2D full spectra for  $\Phi = 0$  and  $\theta = 0$ . As observed in **Figure 2**, all junctions may have interactions between MBSs from the same TSC. Therefore, in A-junction we have three additional parameter configurations obtained: when  $\xi_1 = 0$  and  $\xi_2 = 0.2$ , the reverse one  $\xi_1 = 0.2$  and  $\xi_2 = 0$ , and finally when  $\xi_1 = \xi_2 = 0.2$ . The former two cases can be understood by considering the length of one TSC to be finite, while the other two nanowires are finite TSCs. One finite TSC generates the overlapping of the MBSs from the same TSC, removing the MBSs from zero energy and two bands that form a subgap in the spectra. The remaining Majorana has no other path that forms a flat band at zero energy. When two finite TSCs are considered, the spectra display four bands inside the gap, with two lower energy bands forming line nodes. Therefore, under those couplings with A-junction configuration, we obtain line and flat band. In this paper, we focus on the case with zero energy crossings and on the formation of topologically protected patterns (**Figure 2**), therefore the latter cases using  $\xi_{2(1)} \neq \xi_{1(2)} = 0$  and  $\xi_1 = \xi_2 \neq 0$  are not presented in figures.

In the B-junction configuration, the system presents only a flat band for any of the couplings as long as  $\xi_2 = \lambda'_2 = 0$ . In contrast with the B-junction, the C-junction allows tuning of  $\xi_1$  and  $\xi_2$ . Therefore, when this junction is considered, it is possible

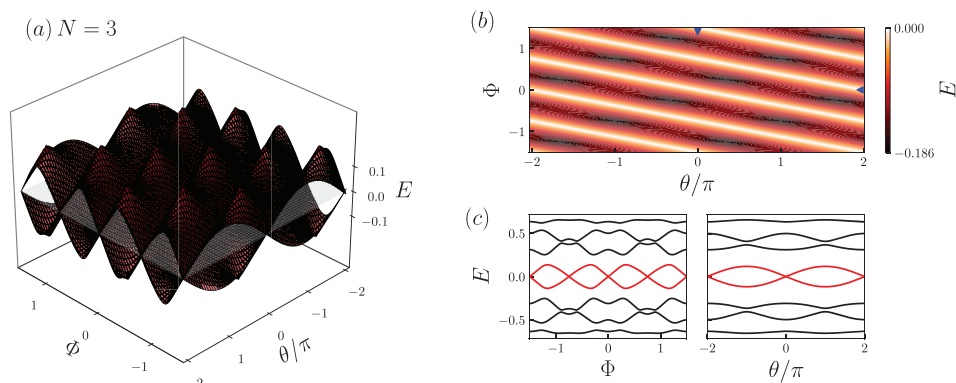


**Figure 3.** Quantum-ring spectra in the A-junction configuration using  $N = 3$ , for coupling amplitudes  $\lambda_1 = \lambda'_1 = 0.5$  and  $\lambda_2 = \lambda'_2 = \xi_1 = \xi_2 = 0$ . a) MBS subgap bands in the parameter space. b) Color map of the negative energy subgap band projection, showing the topological pattern of line nodes. c) 2D representation of the full spectra for fixed values  $\theta = 0$  (left panel) and  $\Phi = 0$  (right panel). Blue triangles in (b) represent the fixed values of flux and phase difference at which the 2D spectra are plotted in (c).

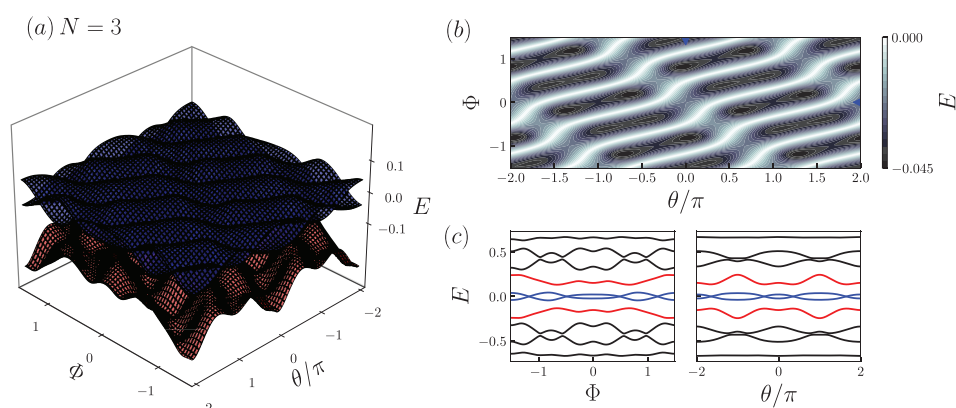


**Figure 4.** Quantum-ring spectra in C-junction configuration with  $N = 3$  and coupling amplitudes  $\lambda_1 = \lambda'_1 = 0.5$ ,  $\lambda_2 = 0$ ,  $\lambda'_2 = 0.3$ , and  $\xi_1 = \xi_2 = 0.2$ . a) MBS subgap bands in the parameter space. b) Color map of the negative energy subgap band projection, showing the undulated nodes topological pattern. c) 2D representation of the full spectra for fixed values  $\theta = 0$  (left panel) and  $\Phi = 0$  (right panel). Blue triangle marks in (b) represent the fixed values of flux and phase difference at which the 2D spectra is plotted in (c).

to obtain line nodes, undulated nodes, and flat bands. We do not graphically present all these behaviors mentioned since line nodes are shown already and an example of a flat band will be shown below in another case. However, undulated nodes can be observed in **Figure 4**, where the spectra are presented for C-junction configuration using the parameters  $\lambda_1 = \lambda'_1 = 0.5$ ,  $\lambda_2 = 0$ ,  $\lambda'_2 = 0.3$ , and  $\xi_1 = \xi_2 = 0.2$ . Panel (a) shows the MBS bands, and panel (b) shows a color map of the negative energy. Two hybridized Majorana bands are observed in these figures, which are better observed in panel (c) in red and blue curves. The red band, with a particle-hole symmetric upper band, forms a subgap in the spectra while the blue band, inside the subgap, forms a zero energy crossing, and in the parameter space, it forms undulated nodes patterns, which correspond to the deformation of the line nodes.

Finally, we address the D-junction configuration, which consists of the direct hybridization of the four MBSs in the quantum-ring. For this junction configuration, line nodes and undulated nodes are obtained, being similar to those presented in Figures 3 and 4. We do not graphically present such results. Henceforth, all

the possible couplings for the four types of junctions that display zero energy crossing and therefore regions where  $C$  symmetry is preserved are summarized in Table 1.

### 3.2.2. Quantum-Ring with Four Quantum Dots

As in the previous subsection, we are not graphically presenting all and each of the nodes observed, since many of them repeatedly appear in the different configurations considered.

For  $N = 4$ , the system possesses two different scenarios: centrosymmetric or noncentrosymmetric ( $j = 2$  and  $j = 1$ , respectively). In this sense, there is a richness in its topological characteristics, since different topological patterns appear according to this configuration. For A-junction, in a non-centrosymmetric case, the system displays three types of nodes: rectangular formation of nodes when  $\xi_1 = \xi_2 = 0$ ; line nodes coexisting with a flat band for  $\xi_1 = 0.2$  and  $\xi_2 = 0$  (not shown graphically); and a four-fold line node when four MBSs display the same line nodes simultaneously for  $\xi_1 = \xi_2 = 0.2$ . In **Figure 5** ( $\xi_1 = \xi_2 = 0$ ), there is

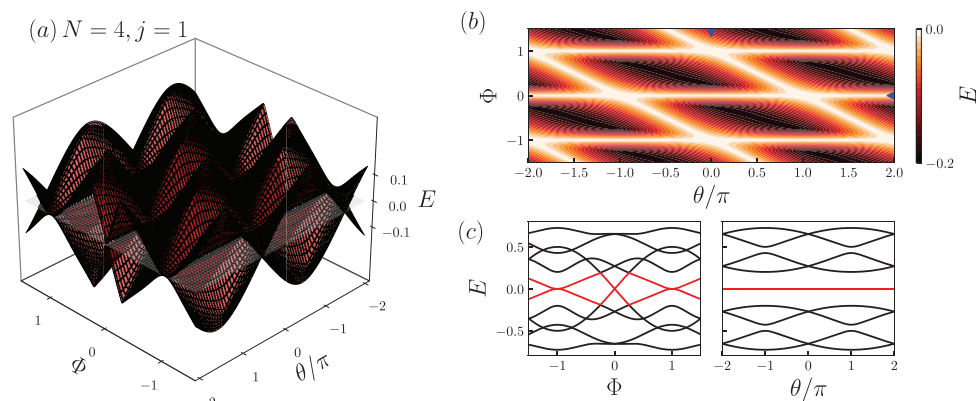


**Figure 5.** Quantum-ring spectra in the A-junction configuration with  $N = 4, j = 1$  with couplings  $\lambda_1 = \lambda'_1 = 0.5, \lambda_2 = \lambda'_2 = 0$ , and  $\xi_1 = \xi_2 = 0$ . a) MBSs subgap bands in the parameter space. b) Color map of the negative energy subgap band projection, showing rectangular nodes topological pattern. c) 2D representation of the full spectra for fixed values  $\theta = 0$  (left panel) and  $\Phi = 0$  (right panel). Blue triangle marks in (b) represent the fixed values of flux and phase difference at which the 2D spectra is plotted in (c).

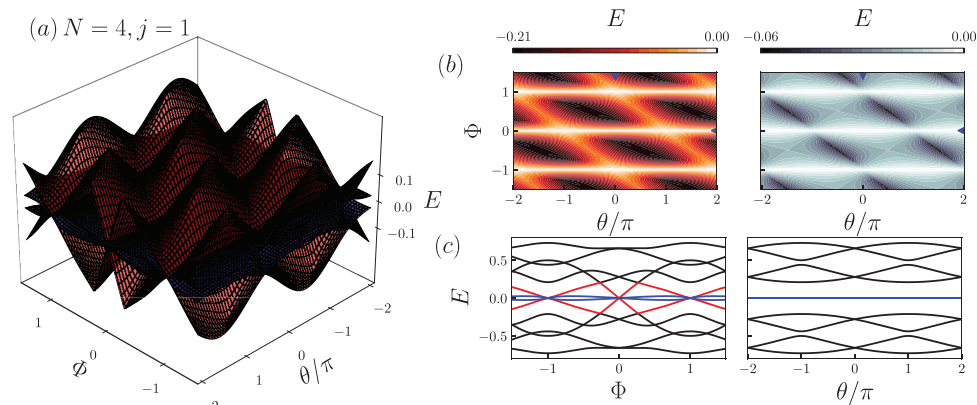


**Figure 6.** Quantum-ring spectra in A-junction configuration with  $N = 4, j = 1$ , the couplings are  $\lambda_1 = \lambda'_1 = 0.5, \lambda_2 = \lambda'_2 = 0$ , and  $\xi_1 = \xi_2 = 0.2$ . a) MBSs subgap bands in the parameter space. b) Color map of the negative energy subgap band projection, showing fourfold line nodes topological pattern. Left and right panels correspond to red and blue bands in panel (c), respectively. c) 2D representation of the full spectra for fixed values  $\theta = 0$  (left panel) and  $\Phi = 0$  (right panel). Blue triangle marks in (b) represent the fixed values of flux and phase difference at which the 2D spectra is plotted in (c).

a graphical representation of the formation of rectangular nodes. The rectangular node pattern is formed by two line nodes coming from different directions in the parameter space: one is formed in  $\mathcal{T}$  reversal points for a ring with  $N = 4$  sites ( $\Phi = \dots, -1, 0, 1, \dots$ ) and remain constant regardless  $\theta$ , and the second line nodes depend on  $\theta$  and  $\Phi$ . On the other hand, in **Figure 6** we present the spectra using  $\xi_1 = \xi_2 = 0.2$ , from which fourfold line nodes are observed. Note that in this case, two Majorana are coupled directly, and the other two are coupled indirectly. For this case there is no formation of a subgap, but rather the four MBSs oscillate around zero energy, sharing the same zero energy points, as can be observed in panel (b) and (c). In a B-junction, line nodes are displayed when  $\xi_1 = \xi_2 = 0.2$  and flat bands when  $\xi_1 = 0.2$  and  $\xi_2 = 0$  (not shown graphically). **Figure 7** shows the spectra for the C-junction configuration with a noncentrosymmetric arrangement, where three MBSs are coupled directly and the TSCs are infinitely long ( $\xi_1 = \xi_2 = 0$ ). The spectra show the coexistence of point nodes and flat bands. The point nodes are formed by the red bands shown in the panel (a) and are located at periodic points

in phase difference  $\theta$ , and along the  $\mathcal{T}$  reversal symmetry points in  $\Phi$ . Since we are considering a spinless or a fully polarized system, these topological point nodes in the parameter space can be seen as Majorana–Weyl cones, which are nondegenerate bands. There are some circuits that can simulate Weyl points without TSCs<sup>[55]</sup> and with TSCs.<sup>[32]</sup> By keeping the same coupling and moving one of the TSCs from site  $j = 1$  to site  $j = 2$ , the system results in a centrosymmetric system, and the point nodes are robust throughout this change, as can be seen in **Figure 8**. The difference is shown with the formation of line nodes coexisting with the point nodes: a pair of MBSs are forming the point nodes while the other two form a line node precisely at  $\mathcal{T}$  reversal symmetric points of a ring with  $N = 4$ .

Finally, in the D-junction configuration, where all MBSs are hybridized directly in the ring and with noncentrosymmetric arrangement, the spectra only display line nodes, while in the case of the centrosymmetric system we can have point and points coexisting with line nodes. Those results are not shown graphically, since they are already shown for other types of configurations. All

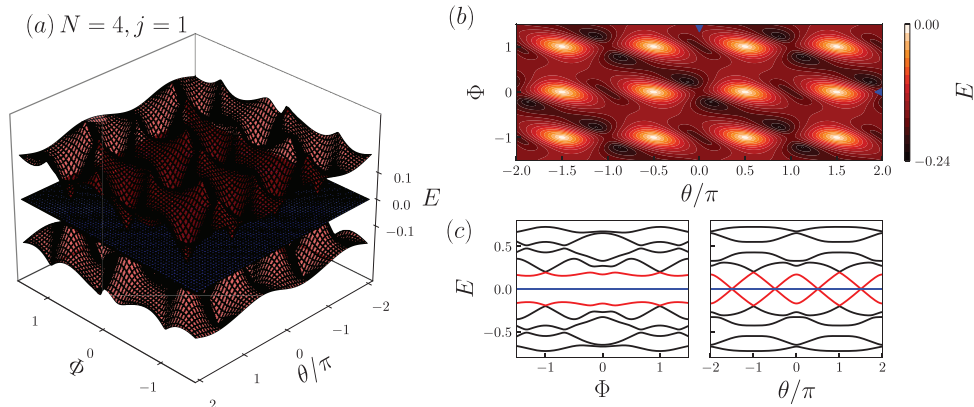


**Figure 7.** Quantum-ring spectra in C-junction configuration with  $N = 4, j = 1$  and coupling amplitudes  $\lambda_1 = \lambda'_1 = 0.5, \lambda_2 = 0, \lambda'_2 = 0.3$ , and  $\xi_1 = \xi_2 = 0$ . a) MBSs subgap bands in the parameter space. b) Color map of the negative energy subgap band projection, showing point nodes topological pattern. c) 2D representation of the full spectra for fixed values  $\theta = 0$  (left panel) and  $\Phi = 0$  (right panel). Blue triangle marks in (b) represent the fixed values of flux and phase difference at which the 2D spectra is plotted in (c).

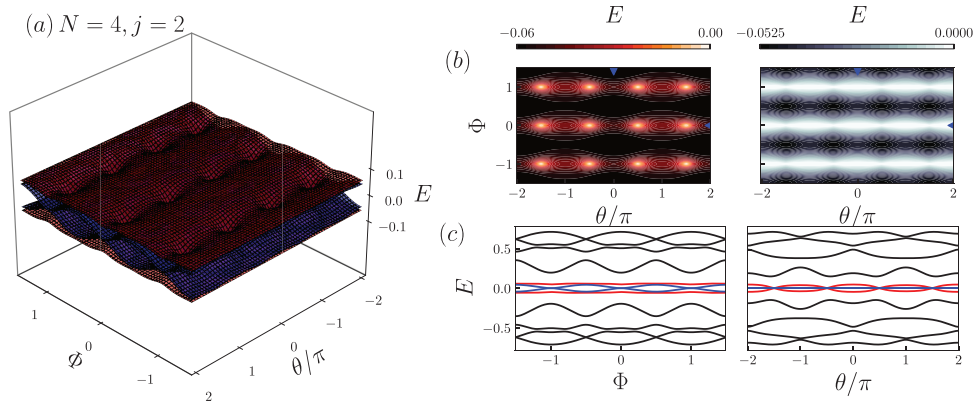


**Figure 8.** Quantum-ring spectra in C-junction configuration with  $N = 4, j = 2$  and coupling amplitudes  $\lambda_1 = \lambda'_1 = 0.5, \lambda_2 = 0, \lambda'_2 = 0.3$ , and  $\xi_1 = \xi_2 = 0.2$ . a) MBSs subgap bands in the parameter space. b) Contour plot representing the projection of the negative energy subgap band, showing point nodes topological pattern. c) 2D representation of the full spectra for fixed values  $\theta = 0$  (left panel) and  $\Phi = 0$  (right panel). Blue triangle marks in (b) represent the fixed values of flux and phase difference at which the 2D spectra is plotted in (c).

the results for a ring formed with four quantum-dots are summarized in Table 2. All possible couplings that are not included in the table break  $C$  symmetry, and as a consequence topological patterns are not formed.<sup>[56,57]</sup>

#### 4. Persistent and DC Josephson Currents

The topological patterns described in the previous section, for each junction, are expected to be observed or measured experimentally through the discontinuities of persistent and DC Josephson currents. Therefore, in this section, we evaluate these two current signals for each of the topological patterns displayed in the parameter space. Hence, the persistent current in the quantum-ring at zero temperature is obtained, given by

$$I_p/I_0 = - \sum_n \frac{\partial}{\partial \Phi} E_n(\Phi, \theta) \quad (13)$$

where  $E_n(\Phi, \theta)$  is a dimensionless quantity (measured in units of  $2t$ ), with particle-hole constraint in the system. Hence, we are

taking the positive energy states as the occupied states, counting from zero energy. Furthermore, the persistent current is taken in units of  $I_0 = 2te/\hbar$ .

Now if we take the differentiation of the energies with respect to the superconducting phase difference  $\theta$ , we obtain the DC Josephson current at zero temperature, given by

$$J/I_0 = 2\pi \sum_n \frac{\partial}{\partial \theta} E_n(\Phi, \theta) \quad (14)$$

Here, fermion parity (FP) switching plays an important role for both types of current signals. In the spectra, we have two even and odd FP sectors that belong to positive and negative energies, or vice versa. When a pair of levels crosses zero energy, the energy excitation of the Bogoliubov quasiparticle changes sign, that is, the ground state of the quantum-ring changes from even/odd to odd/even FP. Currents are continuous signals except for high symmetry points. Hence, when negative and positive energy modes cross at zero energy, a discontinuity in the persistent current is observed. **Figure 9** shows the contour plots for

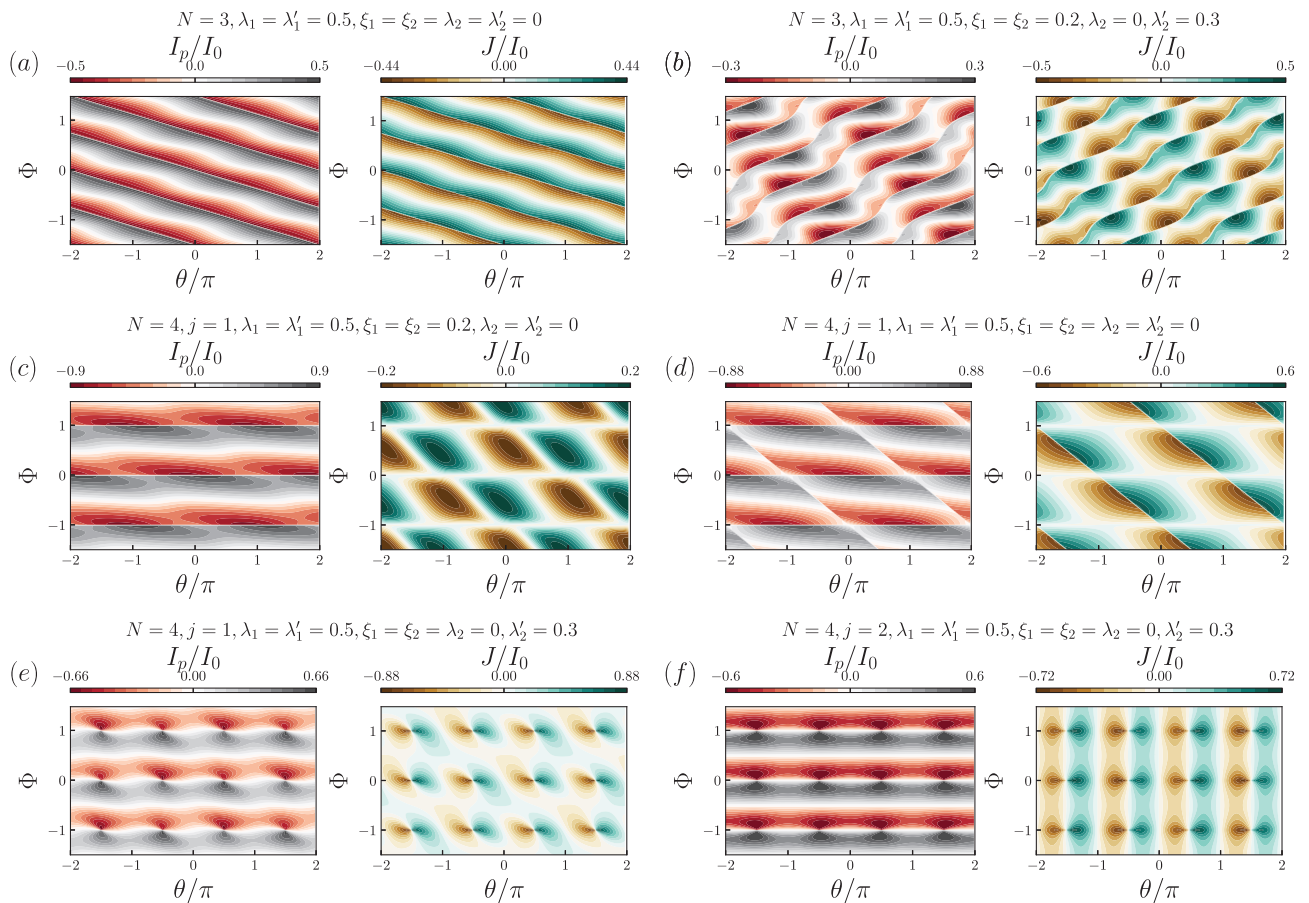


**Figure 9.** Left (red and black colors) and right (yellow and green colors) columns display persistent and DC Josephson currents, respectively. a) Current signals where linear patterns are observed in both signals. b) Current signals with undulating pattern is observed in both signals. c) Current signals. Here, DC Josephson current does not detect any zero energy crossing. d) Current signals, where persistent current detects the rectangular pattern while DC Josephson just detects the pattern partially. e) Current signals, where Point pattern can be observed in both current signals. f) Current signals, where point pattern is also observed in both signals.

persistent (red and gray colors) and Josephson currents (brown and blue-green colors) related to linear, undulated, fourfold linear, rectangular, point, and finally point and line node patterns in panels (a–f) respectively. Note that in (a) and (b) line nodes are shown in the persistent and DC Josephson currents by the sudden changes in the current signal. In (c) the persistent currents show clearly the line nodes that are located at integer values of magnetic flux. On the other hand, DC Josephson current cannot detect the line nodes in this configuration since the formation of these nodes is independent of the phase difference, contrary to what happens in the previous case. In (d), persistent current shows the square pattern, but DC Josephson currents only detect part of the rectangular pattern. In (e), the signatures for point nodes are dipole formations in the parameter space. For persistent current, the dipole orientation is in  $\Phi$ , and for DC Josephson current, the orientation is in  $\theta$ . In panel (f) point nodes can be distinguished in the same way, but since line nodes are independent of  $\theta$ , they cannot be distinguished by DC Josephson signals, only by persistent currents.

A characteristic that deserves some attention can be observed in panels (a) and (b) from Figure 9, where persistent and DC Josephson current do not cancel out at zero magnetic flux and

zero phase difference, respectively. From the spectra described above and expressions (13) and (14), we can see precisely these phenomena. In the former, the presence of a superconducting phase difference breaks  $\mathcal{T}$  symmetry generating a shift in the current signal observing persistent current at zero magnetic flux, and in the latter while the system is at equilibrium, meaning superconducting phase difference is zero, magnetic flux induces DC Josephson current. This phenomenon is not unique due to the presence of MBSs since persistent currents without gauge field can be obtained by reservoir engineering, as has been studied in ref. [58]. Also, in ref. [59] a triple-arm Aharonov–Bohm ring is studied with an impurity where the breaking of  $\mathcal{T}$  symmetry not only occurs by means of magnetic flux, but also due to charge stored in the three arms.

Figure 10 panel (a), shows persistent currents as red, purple, and brown lines that are the currents for different values of phase difference, and panel (b), shows DC Josephson currents where blue, orange, and green lines are currents for different values of magnetic flux. Similar color configurations are used for the other panels. The phenomena that we mentioned above can be appreciated in the last four panels (e–h), where persistent currents are presented as a function of superconducting phase difference and

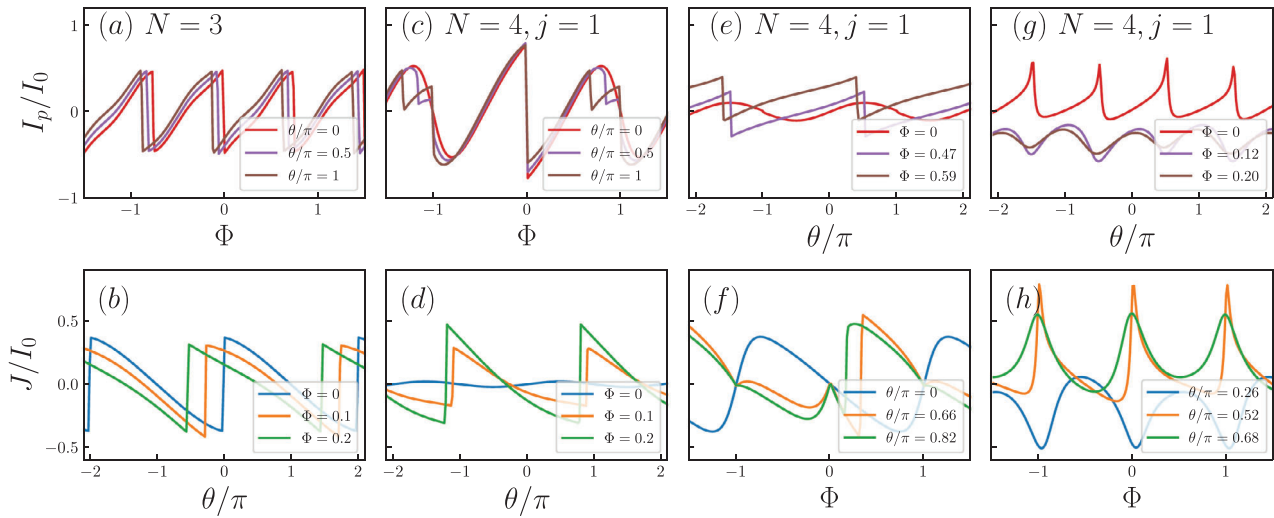


**Figure 10.** a,c) Persistent currents as functions of magnetic flux. b,d) DC Josephson currents, where all panels above are for  $\lambda_1 = \lambda'_1 = 0.5$ ,  $\lambda_2 = \lambda'_2 = 0$ ,  $\xi_1 = 0$ ,  $\xi_2 = 0$ . e,f) Persistent and DC Josephson currents as functions of the phase difference and magnetic flux, respectively. g,h) Persistent and DC Josephson currents as functions of the phase difference and magnetic flux. Colors in labels represent fixed magnetic fluxes and phase differences.

the DC Josephson currents are plotted as a function of the magnetic flux. Hence, it is worth to mention that it is possible to maneuver the persistent currents with the superconducting phase differences and the DC Josephson current with the magnetic flux. In other words, our results show that in our system the persistent currents can be obtained for zero magnetic flux and the DC Josephson currents can be obtained for zero phase difference between both TSCs.

At this point, it is important to highlight that we have checked our results by using an alternative form to calculate both currents, which are obtained by means of the variation of the total number of particles in the quantum ring, given by

$$\frac{dN}{dt} = -\frac{i}{\hbar} [c_r^\dagger c_l, H] \quad (15)$$

with the current being defined as  $I = e\langle \dot{N} \rangle$ . Therefore, we can express it as  $I = I_p + J$ . Hence, persistent current in the position representation reads

$$I_p = -i\frac{e}{\hbar} \sum_l \left( e^{i\frac{2\pi}{N}\Phi} \langle c_m^\dagger c_{m+1} \rangle - e^{-i\frac{2\pi}{N}\Phi} \langle c_{m+1}^\dagger c_m \rangle \right) \quad (16)$$

Through a Fourier transformation and the implementation of the fluctuation-dissipation theorem, we can write the total current as

$$I = \int d\omega f(\omega) [j_p(\omega) + j_j(\omega)] \quad (17)$$

with  $j_p(\omega)$  being the current density for the persistent current contribution given by<sup>[60]</sup>

$$j_p(\omega) = \frac{e}{\hbar\pi} \sum_k 2 \sin\left(\frac{2\pi}{N}\Phi + k\right) \text{Im} \langle \langle c_k^\dagger; c_k \rangle \rangle_\omega^r \quad (18)$$

which is completely equivalent to expression (13). Hence,  $j_j(\omega)$  is the Josephson density current, given by

$$j_j(\omega) = -\frac{4e}{\hbar} \sum_k \text{Im}[\lambda_{(-)}'^s e^{ikj} \text{Im} \langle \langle a^\dagger; c_k^\dagger \rangle \rangle_\omega^r + \lambda_{(+)}' e^{ikj} \text{Im} \langle \langle a; c_k^\dagger \rangle \rangle_\omega^r + \lambda_{(-)} \text{Im} \langle \langle f^\dagger; c_k^\dagger \rangle \rangle_\omega^r + \lambda_{(+)} \text{Im} \langle \langle f; c_k^\dagger \rangle \rangle_\omega^r] \quad (19)$$

where,

$$\begin{aligned} \lambda_{(-)}' &= \frac{1}{2} \left( \lambda_1' e^{-i\frac{\theta}{2}} - \lambda_2' e^{i\frac{\theta}{2}} \right) \\ \lambda_{(+)}' &= \frac{1}{2} \left( \lambda_1' e^{i\frac{\theta}{2}} + \lambda_2' e^{-i\frac{\theta}{2}} \right) \\ \lambda_{(\pm)} &= \frac{1}{2} (\lambda_1 \pm \lambda_2) \end{aligned} \quad (20)$$

## 5. Summary

In this work, we studied a system formed by a quantum-ring embedded between two TSCs, both hosting MBSs at their ends. A magnetic flux crosses the ring, and we considered two quantum-ring sizes, that is,  $N = 3$  and  $N = 4$ . Based on the tuning of the magnetic flux and the superconducting phase difference, we obtain the spectra of the system, observing zero energy-crossing points and flat bands. All the features obtained in the spectra could be observed through persistent and DC Josephson current measurements, by looking for the discontinuities in the signals for linear and undulated patterns. For the case of point nodes, the characteristic is the formation of the dipole-like structure in the currents. Interestingly, our results show that the persistent current and the DC Josephson current can be manipulated by variations in superconducting phase and magnetic flux, respectively, being clear that these phenomena are not due to the presence of MBSs. Thus, we believe our findings can be helpful to

understand the interplay between both current signals and their relation with the system spectra.

Furthermore, we highlight that the currents obtained may be accessible in experiments. The most common setups for the detection of MBSs in 1D TSCs with QD are made of InAs and GaAs.<sup>[42,61,62]</sup> In these setups, a segment of nanowire is covered with Al to build a TSC, leaving bare a shorter section of a few nm at the edges. These bare sections play the role of QDs where the charge is controlled by gate voltages. Based on the above description, a similar engineering can be used to make a quantum-ring with two TSCs. The QDs can be inserted as local impurities in the ring. Given the fact that nanowires usually have a width in the order of nm and lengths in the order of  $\mu\text{m}$ ,<sup>[63]</sup> the actual ring diameter could be also in the order of  $\mu\text{m}$ , which can hold persistent currents with amplitudes  $\approx 1$  nA at temperatures below 1 K. A wide range of magnetic fields can be experimentally obtained by the implementation of a single-crystal Si cantilever.<sup>[64]</sup> As a starting point, the experimental realization for the measurement of DC Josephson currents in multiterminal TSCs could be based on the promising experiments in multiterminal Josephson junctions with conventional superconductivity, where the superconductors are made of Al on top of an InAs 2DEG.<sup>[65–67]</sup>

Finally, the configuration gives the possibility of using our proposal in braiding operations if we consider a time-dependent magnetic flux. In ref. [68], six possible braiding operations are shown for four Majorana modes. In our proposal, a resonant manipulation can be performed by applying linear time-dependent magnetic flux pulses, in order to produce oscillating coupling with the frequency, matching the energy spacing between the Majorana modes.

## Appendix A: Hamiltonian Symmetry

The Hamiltonian of the system in Majorana representation, and in a BdG form, takes the form of a skew-symmetric matrix. Considering a single mode in the quantum ring, the spinor is written as  $\Psi = (\alpha_0^{(1)} \alpha_0^{(2)} \eta_1 \eta_2 \eta_3 \eta_4)^T$  and the Hamiltonian can be written as

$$H_R^{\text{BdG}} = \frac{1}{2} \epsilon(\Phi) \begin{pmatrix} 0 & i & 0 & 0 & 0 & 0 \\ -i & 0 & 0 & 0 & 0 & 0 \\ 0 & 0 & 0 & 0 & 0 & 0 \\ 0 & 0 & 0 & 0 & 0 & 0 \\ 0 & 0 & 0 & 0 & 0 & 0 \\ 0 & 0 & 0 & 0 & 0 & 0 \end{pmatrix} \quad (\text{A1})$$

$$H_{\text{TSC}}^{\text{BdG}} = \frac{1}{2} \xi_1 \begin{pmatrix} 0 & 0 & 0 & 0 & 0 & 0 \\ 0 & 0 & 0 & 0 & 0 & 0 \\ 0 & 0 & 0 & i & 0 & 0 \\ 0 & 0 & -i & 0 & 0 & 0 \\ 0 & 0 & 0 & 0 & 0 & 0 \\ 0 & 0 & 0 & 0 & 0 & 0 \end{pmatrix} + \frac{1}{2} \xi_2 \begin{pmatrix} 0 & 0 & 0 & 0 & 0 & 0 \\ 0 & 0 & 0 & 0 & 0 & 0 \\ 0 & 0 & 0 & 0 & 0 & 0 \\ 0 & 0 & 0 & 0 & 0 & 0 \\ 0 & 0 & 0 & 0 & 0 & i \\ 0 & 0 & 0 & 0 & -i & 0 \end{pmatrix} \quad (\text{A2})$$

$$H_C^{\text{BdG}} = \frac{1}{2} \lambda_1 \begin{pmatrix} 0 & 0 & 0 & 0 & 0 & 0 \\ 0 & 0 & -i & 0 & 0 & 0 \\ 0 & i & 0 & 0 & 0 & 0 \\ 0 & 0 & 0 & 0 & 0 & 0 \\ 0 & 0 & 0 & 0 & 0 & 0 \\ 0 & 0 & 0 & 0 & 0 & 0 \end{pmatrix} + \frac{1}{2} \lambda_2 \begin{pmatrix} 0 & 0 & 0 & i & 0 & 0 \\ 0 & 0 & 0 & 0 & 0 & 0 \\ 0 & 0 & 0 & 0 & 0 & 0 \\ -i & 0 & 0 & 0 & 0 & 0 \\ 0 & 0 & 0 & 0 & 0 & 0 \\ 0 & 0 & 0 & 0 & 0 & 0 \end{pmatrix} + \frac{1}{2} \lambda'_1 S(\theta) \begin{pmatrix} 0 & 0 & 0 & 0 & i & 0 \\ 0 & 0 & 0 & 0 & 0 & 0 \\ 0 & 0 & 0 & 0 & 0 & 0 \\ -i & 0 & 0 & 0 & 0 & 0 \\ 0 & 0 & 0 & 0 & 0 & 0 \end{pmatrix} + \frac{1}{2} \lambda'_1 C(\theta) \begin{pmatrix} 0 & 0 & 0 & 0 & 0 & 0 \\ 0 & 0 & 0 & 0 & -i & 0 \\ 0 & 0 & 0 & 0 & 0 & 0 \\ 0 & 0 & 0 & 0 & 0 & 0 \\ 0 & i & 0 & 0 & 0 & 0 \\ 0 & 0 & 0 & 0 & 0 & 0 \end{pmatrix} + \frac{1}{2} \lambda'_2 C(\theta) \begin{pmatrix} 0 & 0 & 0 & 0 & 0 & i \\ 0 & 0 & 0 & 0 & 0 & 0 \\ 0 & 0 & 0 & 0 & 0 & 0 \\ 0 & 0 & 0 & 0 & 0 & 0 \\ 0 & 0 & 0 & 0 & 0 & 0 \\ -i & 0 & 0 & 0 & 0 & 0 \end{pmatrix} + \frac{1}{2} \lambda'_2 S(\theta) \begin{pmatrix} 0 & 0 & 0 & 0 & 0 & 0 \\ 0 & 0 & 0 & 0 & 0 & -i \\ 0 & 0 & 0 & 0 & 0 & 0 \\ 0 & 0 & 0 & 0 & 0 & 0 \\ i & 0 & 0 & 0 & 0 & 0 \\ 0 & 0 & 0 & 0 & 0 & 0 \end{pmatrix} \quad (\text{A3})$$

It is straightforward to distinguish the basis on which the Hamiltonian is written. On this basis, and for a single mode in the ring, the Hamiltonian is expressed in terms of some elements of the SU(6) Lie algebra in  $\lambda$ -representation. Hence, we can write the Hamiltonian as

$$H_{\text{BdG}} = \frac{1}{2} (-\epsilon(\Phi) \tilde{\lambda}_2 - \xi_1 \tilde{\lambda}_{14} - \xi_2 \tilde{\lambda}_{34} + \lambda_1 \tilde{\lambda}_{17} + \lambda_1 \tilde{\lambda}_7 - \lambda_2 \tilde{\lambda}_{10} - \lambda'_1 S(\theta) \tilde{\lambda}_{17} + \lambda'_1 C(\theta) \tilde{\lambda}_{19} - \lambda'_2 C(\theta) \tilde{\lambda}_{26} + \lambda'_2 S(\theta) \tilde{\lambda}_{28}) \quad (\text{A4})$$

where  $\epsilon(\Phi) = \cos(2\pi\Phi/N)$ ,  $S(\theta) = \sin(\theta/2)$ ,  $C(\theta) = \cos(\theta/2)$ , and  $\tilde{\lambda}_i$  are the imaginary elements of the SU(6) group. Therefore, we can define a vector  $\mathbf{h}$  with a dimension 36 with non-zero components written in the above Hamiltonian. Similarly, we can represent as a vector the whole basis of the SU(6) algebra and the full Hamiltonian, written in a compact form as  $H_{\text{BdG}} = \mathbf{h} \cdot \Lambda/2$ . This

is generalized easily for any number of modes in the quantum-ring. Since the Hamiltonian can be written as a linear combination of the basic elements of the  $SU(2N + 4)$ , the system possesses that symmetry.

## Acknowledgements

F.G.M. is grateful for the funding of CONICYT-Chile scholarship No. 21170550. J.P.R.-A is grateful for the funding of FONDECYT Postdoc. Grant No. 3190301 (2019). L.R. and P.A.O. acknowledges support from FONDECYT Grant No. 1180914 and 1201876.

## Conflict of Interest

The authors declare no conflict of interest.

## Data Availability Statement

Research data are not shared.

## Keywords

Majorana bound states, persistent currents, quantum rings

Received: June 26, 2021

Revised: September 9, 2021

Published online: October 29, 2021

- [1] M. Z. Hasan, C. L. Kane, *Rev. Mod. Phys.* **2010**, *82*, 3045.
- [2] X.-L. Qi, S.-C. Zhang, *Rev. Mod. Phys.* **2011**, *83*, 1057.
- [3] M. Sato, Y. Ando, *Rep. Prog. Phys.* **2017**, *80*, 076501.
- [4] L. Lu, Z. Wang, D. Ye, L. Ran, L. Fu, J. D. Joannopoulos, M. Soljačić, *Science* **2015**, *349*, 622.
- [5] S.-Y. Xu, I. Belopolski, N. Alidoust, M. Neupane, G. Bian, C. Zhang, R. Sankar, G. Chang, Z. Yuan, C.-C. Lee, S.-M. Huang, R. Sankar, F. Chou, C.-H. Hsu, H.-T. Jeng, A. Bansil, T. Neupert, V. N. Strocov, H. Lin, S. Jia, M. Z. Hasan, *Science* **2015**, *349*, 613.
- [6] A. A. Soluyanov, D. Gresch, Z. Wang, Q. Wu, M. Troyer, X. Dai, B. A. Bernevig, *Nature* **2015**, *527*, 495.
- [7] C.-K. Chiu, J. C. Teo, A. P. Schnyder, S. Ryu, *Rev. Mod. Phys.* **2016**, *88*, 035005.
- [8] P. Kotetes, *New J. Phys.* **2013**, *15*, 105027.
- [9] A. P. Schnyder, S. Ryu, A. Furusaki, A. W. Ludwig, *Phys. Rev. B* **2008**, *78*, 195125.
- [10] A. Y. Kitaev, *Phys.-Usp.* **2001**, *44*, 131.
- [11] A. Aleccia, L. Dell'Anna, *Phys. Rev. B* **2017**, *95*, 195160.
- [12] J.-J. Miao, H.-K. Jin, F.-C. Zhang, Y. Zhou, *Phys. Rev. Lett.* **2017**, *118*, 267701.
- [13] A. Matos-Abiad, J. Shabani, A. D. Kent, G. L. Fatin, B. Scharf, I. Žutić, *Solid State Commun.* **2017**, *262*, 1.
- [14] J. Alicea, Y. Oreg, G. Refael, F. Von Oppen, M. P. Fisher, *Nat. Phys.* **2011**, *7*, 412.
- [15] S. D. Sarma, M. Freedman, C. Nayak, *npj Quantum Inf.* **2015**, *1*, 15001.
- [16] B. Van Heck, A. Akhmerov, F. Hassler, M. Burrello, C. Beenakker, *New J. Phys.* **2012**, *14*, 035019.
- [17] V. Mourik, K. Zuo, S. M. Frolov, S. Plissard, E. P. Bakkers, L. P. Kouwenhoven, *Science* **2012**, *336*, 1003.
- [18] M. Deng, C. Yu, G. Huang, M. Larsson, P. Caroff, H. Xu, *Nano Lett.* **2012**, *12*, 6414.
- [19] M. Nishiyama, Y. Inada, G.-q. Zheng, *Phys. Rev. Lett.* **2007**, *98*, 047002.
- [20] J.-K. Bao, J.-Y. Liu, C.-W. Ma, Z.-H. Meng, Z.-T. Tang, Y.-L. Sun, H.-F. Zhai, H. Jiang, H. Bai, C.-M. Feng, Z.-A. Xu, G.-H. Cao, *Phys. Rev. X* **2015**, *5*, 011013.
- [21] M. Eschrig, *Rep. Prog. Phys.* **2015**, *78*, 104501.
- [22] A. Das, Y. Ronen, Y. Most, Y. Oreg, M. Heiblum, H. Shtrikman, *Nat. Phys.* **2012**, *8*, 887.
- [23] F. Domínguez, J. Cayao, P. San-Jose, R. Aguado, A. L. Yeyati, E. Prada, *npj Quantum Mater.* **2017**, *2*, 13.
- [24] R. M. Lutchyn, E. P. Bakkers, L. P. Kouwenhoven, P. Krogstrup, C. M. Marcus, Y. Oreg, *Nat. Rev. Mater.* **2018**, *3*, 52.
- [25] J. S. Meyer, M. Houzet, *Phys. Rev. Lett.* **2017**, *119*, 136807.
- [26] H.-Y. Xie, M. G. Vavilov, A. Levchenko, *Phys. Rev. B* **2017**, *96*, 161406.
- [27] R.-P. Riwar, M. Houzet, J. S. Meyer, Y. V. Nazarov, *Nat. Commun.* **2016**, *7*, 11167.
- [28] H.-Y. Xie, M. G. Vavilov, A. Levchenko, *Phys. Rev. B* **2018**, *97*, 035443.
- [29] F. Zhang, C. Kane, *Phys. Rev. B* **2014**, *90*, 020501.
- [30] K. Sakurai, M. T. Mercaldo, S. Kobayashi, A. Yamakage, S. Ikegaya, T. Habe, P. Kotetes, M. Cuoco, Y. Asano, *Phys. Rev. B* **2020**, *101*, 174506.
- [31] M. Houzet, J. S. Meyer, *Phys. Rev. B* **2019**, *100*, 014521.
- [32] P. Kotetes, M. T. Mercaldo, M. Cuoco, *Phys. Rev. Lett.* **2019**, *123*, 126802.
- [33] C. Nayak, S. H. Simon, A. Stern, M. Freedman, S. D. Sarma, *Rev. Mod. Phys.* **2008**, *80*, 1083.
- [34] J. D. Sau, D. J. Clarke, S. Tewari, *Phys. Rev. B* **2011**, *84*, 094505.
- [35] W.-C. Huang, Q.-F. Liang, D.-X. Yao, Z. Wang, *Phys. Rev. A* **2015**, *92*, 012308.
- [36] Z. Wang, W.-C. Huang, Q.-F. Liang, X. Hu, *Sci. Rep.* **2018**, *8*, 7920.
- [37] M. Trif, O. Dmytruk, H. Bouchiat, R. Aguado, P. Simon, *Phys. Rev. B* **2018**, *97*, 041415.
- [38] C. Malciu, L. Mazza, C. Mora, *Phys. Rev. B* **2018**, *98*, 165426.
- [39] T. Hyart, B. Van Heck, I. Fulga, M. Burrello, A. Akhmerov, C. Beenakker, *Phys. Rev. B* **2013**, *88*, 035121.
- [40] E. Vernek, P. Penteado, A. Seridonio, J. Egues, *Phys. Rev. B* **2014**, *89*, 165314.
- [41] D. E. Liu, H. U. Baranger, *Phys. Rev. B* **2011**, *84*, 201308.
- [42] M.-T. Deng, S. Vaitiekėnas, E. Prada, P. San-Jose, J. Nygård, P. Krogstrup, R. Aguado, C. Marcus, *Phys. Rev. B* **2018**, *98*, 085125.
- [43] F. Medina, J. P. Ramos-Andrade, L. Rosales, P. Orellana, *Ann. Phys.* **2020**, *532*, 2000199.
- [44] A. Nava, R. Giuliano, G. Campagnano, D. Giuliano, *Phys. Rev. B* **2017**, *95*, 155449.
- [45] C.-K. Chiu, J. D. Sau, S. D. Sarma, *Phys. Rev. B* **2018**, *97*, 035310.
- [46] Z. Liu, J. Jiang, B. Zhou, Z. Wang, Y. Zhang, H. Weng, D. Prabhakaran, S. K. Mo, H. Peng, P. Dudin, T. Kim, M. Hoesch, Z. Fang, X. Dai, Z. X. Shen, D. L. Feng, Z. Hussain, Y. L. Chen, *Nat. Mater.* **2014**, *13*, 677.
- [47] M. Neupane, S.-Y. Xu, R. Sankar, N. Alidoust, G. Bian, C. Liu, I. Belopolski, T.-R. Chang, H.-T. Jeng, H. Lin, A. Bansil, F. Chou, M. Zahid, *Nat. Commun.* **2014**, *5*, 3786.
- [48] S. D. Sarma, J. D. Sau, T. D. Stanescu, *Phys. Rev. B* **2012**, *86*, 220506.
- [49] D. Rainis, L. Trifunovic, J. Klinovaja, D. Loss, *Phys. Rev. B* **2013**, *87*, 024515.
- [50] J. Danon, E. B. Hansen, K. Flensberg, *Phys. Rev. B* **2017**, *96*, 125420.
- [51] L. Ricco, V. Campo Jr, I. Shelykh, A. Seridonio, *Phys. Rev. B* **2018**, *98*, 075142.
- [52] M. Sato, Y. Tanaka, K. Yada, T. Yokoyama, *Phys. Rev. B* **2011**, *83*, 224511.

- [53] A. Whiticar, A. Fornieri, E. O'Farrell, A. Drachmann, T. Wang, C. Thomas, S. Gronin, R. Kallaher, G. Gardner, M. Manfra, C. M. Marcus, F. Nichele, *Nat. Commun.* **2020**, *11*, 3212.
- [54] H. Potts, I.-J. Chen, A. Tsintzis, M. Nilsson, S. Lehmann, K. A. Dick, M. Leijnse, C. Thelander, *Nat. Commun.* **2019**, *10*, 5740.
- [55] V. Fatemi, A. R. Akhmerov, L. Bretheau, *Phys. Rev. Res.* **2021**, *3*, 013288.
- [56] J. C. Teo, C. L. Kane, *Phys. Rev. B* **2010**, *82*, 115120.
- [57] C. Beenakker, D. Pikulin, T. Hyart, H. Schomerus, J. Dahlhaus, *Phys. Rev. Lett.* **2013**, *110*, 017003.
- [58] M. Keck, D. Rossini, R. Fazio, *Phys. Rev. A* **2018**, *98*, 053812.
- [59] H.-M. Li, J.-L. Xiao, *Phys. B* **2007**, *396*, 91.
- [60] S. K. Maiti, S. Saha, S. Karmakar, *Eur. Phys. J. B* **2011**, *79*, 209.
- [61] M. Deng, S. Vaitiekėnas, E. B. Hansen, J. Danon, M. Leijnse, K. Flensberg, J. Nygård, P. Krogstrup, C. M. Marcus, *Science* **2016**, *354*, 1557.
- [62] E. Prada, R. Aguado, P. San-Jose, *Phys. Rev. B* **2017**, *96*, 085418.
- [63] S. Vaitiekėnas, G. Winkler, B. van Heck, T. Karzig, M.-T. Deng, K. Flensberg, L. Glazman, C. Nayak, P. Krogstrup, R. Lutchyn, C. M. Marcus, *Science* **2020**, *367*, eaav3392.
- [64] A. Bleszynski-Jayich, W. Shanks, B. Peaudecerf, E. Ginossar, F. Von Oppen, L. Glazman, J. Harris, *Science* **2009**, *326*, 272.
- [65] N. Pankratova, H. Lee, R. Kuzmin, K. Wickramasinghe, W. Mayer, J. Yuan, M. G. Vavilov, J. Shabani, V. E. Manucharyan, *Phys. Rev. X* **2020**, *10*, 031051.
- [66] A. W. Draelos, M.-T. Wei, A. Seredinski, H. Li, Y. Mehta, K. Watanabe, T. Taniguchi, I. V. Borzenets, F. Amet, G. Finkelstein, *Nano Lett.* **2019**, *19*, 1039.
- [67] G. V. Graziano, J. S. Lee, M. Pendharkar, C. J. Palmström, V. S. Pribiag, *Phys. Rev. B* **2020**, *101*, 054510.
- [68] V. Kornich, X. Huang, E. Repin, Y. V. Nazarov, *Phys. Rev. Lett.* **2021**, *126*, 117701.

# Bibliography

- [1] Alexander Altland and Martin R Zirnbauer. Nonstandard symmetry classes in mesoscopic normal-superconducting hybrid structures. *Physical Review B*, 55(2):1142, 1997.
- [2] Philip W Anderson and Daniel L Stein. Broken symmetry, emergent properties, dissipative structures, life. In *Self-organizing systems*, pages 445–457. Springer, 1987.
- [3] John Bardeen, Leon N Cooper, and John Robert Schrieffer. Theory of superconductivity. *Physical review*, 108(5):1175, 1957.
- [4] B Andrei Bernevig. *Topological insulators and topological superconductors*. Princeton university press, 2013.
- [5] Guang Bian, Tay-Rong Chang, Raman Sankar, Su-Yang Xu, Hao Zheng, Titus Neupert, Ching-Kai Chiu, Shin-Ming Huang, Guoqing Chang, Ilya Belopolski, et al. Topological nodal-line fermions in the non-centrosymmetric superconductor compound pbtase2. *arXiv preprint arXiv:1505.03069*, 2015.
- [6] Guang Bian, Tay-Rong Chang, Raman Sankar, Su-Yang Xu, Hao Zheng, Titus Neupert, Ching-Kai Chiu, Shin-Ming Huang, Guoqing Chang, Ilya Belopolski, et al. Topological nodal-line fermions in spin-orbit metal pbtase 2. *Nature communications*, 7(1):1–8, 2016.
- [7] Guoqing Chang, Su-Yang Xu, Hao Zheng, Bahadur Singh, Chuang-Han Hsu, Guang Bian, Nasser Alidoust, Ilya Belopolski, Daniel S Sanchez, Songtian Zhang, et al. Room-temperature magnetic topological weyl fermion and nodal line semimetal states in half-metallic heusler  $\text{Co}_2\text{TiX}$  ( $X = \text{Si, Ge, or Sn}$ ). *Scientific reports*, 6(1):1–9, 2016.
- [8] Y-C Chiu, K-W Chen, Rico Schoenemann, VL Quito, S Sur, Q Zhou, D Graf, E Kampert, T Förster, K Yang, et al. Origin of the butterfly magnetoresistance in a dirac nodal-line system. *Physical Review B*, 100(12):125112, 2019.
- [9] Piers Coleman. *Introduction to many-body physics*. Cambridge University Press, 2015.
- [10] Sergey Frolov. Quantum computing’s reproducibility crisis: Majorana fermions, 2021.

- [11] B-B Fu, C-J Yi, T-T Zhang, M Caputo, J-Z Ma, X Gao, BQ Lv, L-Y Kong, Y-B Huang, P Richard, et al. Dirac nodal surfaces and nodal lines in zrsis. *Science advances*, 5(5):eaau6459, 2019.
- [12] Liang Fu and Charles L Kane. Superconducting proximity effect and majorana fermions at the surface of a topological insulator. *Physical review letters*, 100(9):096407, 2008.
- [13] Dmitri A Ivanov. Non-abelian statistics of half-quantum vortices in p-wave superconductors. *Physical review letters*, 86(2):268, 2001.
- [14] Radi A Jishi. *Feynman diagram techniques in condensed matter physics*. Cambridge University Press, 2013.
- [15] A Yu Kitaev. Unpaired majorana fermions in quantum wires. *Physics-uspekhi*, 44(10S):131, 2001.
- [16] Panagiotis Kotetes, Maria Teresa Mercaldo, and Mario Cuoco. Synthetic weyl points and chiral anomaly in majorana devices with nonstandard andreev-bound-state spectra. *Physical review letters*, 123(12):126802, 2019.
- [17] Chun-Xiao Liu, Jay D Sau, and S Das Sarma. Distinguishing topological majorana bound states from trivial andreev bound states: Proposed tests through differential tunneling conductance spectroscopy. *Physical Review B*, 97(21):214502, 2018.
- [18] Chun-Xiao Liu, Jay D Sau, Tudor D Stanescu, and S Das Sarma. Andreev bound states versus majorana bound states in quantum dot-nanowire-superconductor hybrid structures: Trivial versus topological zero-bias conductance peaks. *Physical Review B*, 96(7):075161, 2017.
- [19] Dong E Liu and Harold U Baranger. Detecting a majorana-fermion zero mode using a quantum dot. *Physical Review B*, 84(20):201308, 2011.
- [20] Ettore Majorana. Teoria simmetrica dell’elettrone e del positrone. *Il Nuovo Cimento (1924-1942)*, 14(4):171–184, 1937.
- [21] Christopher Moore, Chuanchang Zeng, Tudor D Stanescu, and Sumanta Tewari. Quantized zero-bias conductance plateau in semiconductor-superconductor heterostructures without topological majorana zero modes. *Physical Review B*, 98(15):155314, 2018.
- [22] Nicholas Read and Dmitry Green. Paired states of fermions in two dimensions with breaking of parity and time-reversal symmetries and the fractional quantum hall effect. *Physical Review B*, 61(15):10267, 2000.
- [23] Roman-Pascal Riwar, Manuel Houzet, Julia S Meyer, and Yuli V Nazarov. Multi-terminal josephson junctions as topological matter. *Nature communications*, 7(1):1–5, 2016.

- [24] Keimei Sakurai, Maria Teresa Mercaldo, Shingo Kobayashi, Ai Yamakage, Satoshi Ikegaya, Tetsuro Habe, Panagiotis Kotetes, Mario Cuoco, and Yasuhiro Asano. Nodal andreev spectra in multi-majorana three-terminal josephson junctions. *Physical Review B*, 101(17):174506, 2020.
- [25] Michael Stone and Suk-Bum Chung. Fusion rules and vortices in  $p_x + i p_y$  superconductors. *Physical Review B*, 73(1):014505, 2006.
- [26] Hao-Hua Sun and Jin-Feng Jia. Detection of majorana zero mode in the vortex. *npj Quantum Materials*, 2(1):1–9, 2017.
- [27] Yan Sun, Yang Zhang, Claudia Felser, and Binghai Yan. Strong intrinsic spin hall effect in the taas family of weyl semimetals. *Physical review letters*, 117(14):146403, 2016.
- [28] Adriaan Vuik, Bas Nijholt, Anton Akhmerov, and Michael Wimmer. Reproducing topological properties with quasi-majorana states. *SciPost Physics*, 7(5):061, 2019.
- [29] Hong-Yi Xie, Maxim G Vavilov, and Alex Levchenko. Topological andreev bands in three-terminal josephson junctions. *Physical Review B*, 96(16):161406, 2017.
- [30] Hong-Yi Xie, Maxim G Vavilov, and Alex Levchenko. Weyl nodes in andreev spectra of multiterminal josephson junctions: Chern numbers, conductances, and supercurrents. *Physical Review B*, 97(3):035443, 2018.
- [31] Konstantin Yavilberg, Eran Ginossar, and Eytan Grosfeld. Differentiating majorana from andreev bound states in a superconducting circuit. *Physical Review B*, 100(24):241408, 2019.